AN INTRINSIC MODEL FOR GRAPHITE OXIDATION AND THE EFFECTS OF MICROSTRUCTURAL FEATURES ON APPARENT RATE

by

Joshua J. Kane

A dissertation
submitted in partial fulfillment
of the requirements for the degree of
Doctor of Philosophy in Materials Science & Engineering
Boise State University

August 2013

BOISE STATE UNIVERSITY GRADUATE COLLEGE

DEFENSE COMMITTEE AND FINAL READING APPROVALS

of the dissertation submitted by

Joshua J. Kane

Dissertation Title: An Intrinsic Model for Graphite Oxidation and the Effects of Microstructure on Apparent Rate

Date of Final Oral Examination: 02 July 2013

The following individuals read and discussed the dissertation submitted by student Joshua J. Kane, and they evaluated his presentation and response to questions during the final oral examination. They found that the student passed the final oral examination.

Darryl P. Butt, Ph.D.	Chair, Supervisory Committee
Rick Ubic, Ph.D.	Member, Supervisory Committee
William E. Windes, Ph.D.	Member, Supervisory Committee
Karthik Chinnathambi, Ph.D.	Member, Supervisory Committee
Hui (Claire) Xiong, Ph.D.	Member, Supervisory Committee

The final reading approval of the dissertation was granted by Darryl P. Butt, Ph.D., Chair of the Supervisory Committee. The dissertation was approved for the Graduate College by John R. Pelton, Ph.D., Dean of the Graduate College.

DEDICATION

This dissertation is dedicated to my wife.

Love suffers long and is kind; love does not envy; love does not parade itself, is not puffed up; does not behave rudely, does no seek its own, is not provoked, thinks no evil; does not rejoice in iniquity, but rejoices in the truth; bears all things, believes all things, endures all things. Love never fails. 1 Corinthians 13:4-8a NKJV

Words will never be able to describe how grateful I am to our Lord and Savior, Jesus Christ, for bringing us together to walk hand-in-hand through this journey we call life.

ACKNOWLEDGEMENTS

Behind every PhD dissertation is a countlessly large group of individuals that have made the work possible in some way, shape, or form. I am very thankful to you all for your advice, guidance, and words of encouragement when I was ready to tear my hair out. There are a few groups and individuals, however, I would like to acknowledge specifically.

First, I would like to acknowledge that this dissertation is based on work supported by the Department of Energy [National Nuclear Security Administration] under Award Nos. 00041394/00026 and DE-NE0000140. Scanning and transmission electron microscopy studies were carried out at the Boise State Center for Materials Characterization and supported by the Department of Energy [National Nuclear Security Administration] under Award Number DE-NE0000338 and the National Science Foundation Major Research Instrumentation Program, Award No. 0521315, respectively. Furthermore, I would like to acknowledge the funding of the Nuclear Regulatory Commission under the Nuclear Materials Fellowship Program (NRC-38-08-955).

Next, I would like to thank Dr. Darryl Butt and the rest of my committee for their willingness to let me branch out from our original project and let me investigate the subjects of interest to me. I also very much appreciate all of your advice, encouragement, and, despite your busy schedules, your willingness to make time to invest in me as an individual and researcher.

I’d also like to thank Dr. Elisa Barney Smith of the Electrical and Computer Engineering department here at Boise State University for introducing me to the wealth of information obtainable through image processing and analysis as well as for advice on how to code the extraction of this information.

Finally, I’d like to thank my wife, parents, and the rest of our close friends that might as well be family (Dr. Brent and Janet Davis, Glenn and Lanie Compton, and Dusty Berggren, just to name a few). Thank you for your encouragement, prayer, and support.

ABSTRACT

The very high temperature reactor (VHTR) is the latest generation of high-temperature gas-cooled reactors (HTGR). The VHTR has higher outlet temperatures than a traditional HTGR with outlet temperatures up to 1000 °C. This high outlet temperature permits emissions-free process heat in the form of high-quality steam for high temperature industrial applications. Moreover, the high temperatures of the reactor could potentially be used for hydrogen production from water or high efficiency electrical power production (~50% efficiency of thermal to electrical power conversion).

The VHTR is designed to employ helium as its coolant and uses graphite for its neutron moderator and as a key structural component for the core. Graphite is used because of it excellent structural stability at high temperatures, high thermal inertia, and the relatively low cost of its production. Since graphite is a key component to the VHTR, the integrity of the graphite is critically linked to the operable lifetime of the reactor. Thorough characterization of the graphite material used, as well as a complete understanding of the mechanisms behind graphite's life-limiting phenomena is critical to understanding the limits of safe operation for the VHTR. Graphite is not a new high temperature nuclear material; in fact, it has been used in nuclear reactor designs since the very first reactor went critical in December of 1942. Due to its continued use in reactors, a major focus has been placed on understanding graphite's long-term degradation in a

radiation environment, and thus many of the phenomena responsible for degradation are well known.

Unfortunately, graphite is a complicated/complex material in that the properties are highly dependent upon the initial source of carbon, as well as variations in the coke type, size and relative quantities of filler and binder, and the manufacturing process used. Thus, each graphite used for nuclear applications is in some sense a new material with unique properties that must be thoroughly characterized before use in a reactor.

This dissertation research is focused on the pre-irradiation characterization of IG-110, PGX, NBG-18, and PCEA commercial graphites, the atomic level defects involved in irradiation induced shrinkage and swelling of these graphite materials, and finally the development of a unified reaction model for the oxidation of all high-purity nuclear graphites with oxygen. While similar characterizations and mechanistic studies have been made, many of the techniques used in this study such as electron energy loss spectroscopy (EELS), image processing and analysis, and filtering of high resolution lattice images were either impractical or unavailable in the past. This dissertation seeks to build on past studies of classical reactor grade graphites and use modern experimental techniques to further our understanding of the specific graphites examined and the underlying mechanism that contribute to graphite degradation.

In Chapter Two, microstructural characterization of the filler and binder materials is performed. All grades examined were well graphitized in both the binder and filler, although the spatial domains of crystallites were significantly smaller in the binder. Turbostratic graphite, indicated by an elliptical diffraction pattern, was present in all grades. The microcracks, which are known to contribute to the bulk materials shrinkage and later swelling, were found to vary significantly in size, shape, and quantity with graphite grade.

Chapter Three examines the atomic scale defects responsible for irradiation induced swelling and microcrack closure via transmission electron microscopy under electron beam irradiation. Utilization of noise-filtering in the frequency domain of lattice images and videos allowed analysis of the formation of vacancy loops, interstitial loops, and resulting dislocations with unprecedented clarity. The dislocations were observed to undergo positive climb resulting in the formation of extra basal planes. This in addition with the reduction in atomic density evidenced by electron energy loss spectroscopy is believed to be responsible for the graphite swelling in the c-direction and microcrack closure.

Using optical microscopy, the macro-scale features of the filler particles and macro-porosity were characterized in Chapter Four. The average size and shape of the two-dimensional cross-sections of the filler particles for each grade was determined. A qualitative trend was found between the aspect ratio of the particles and the degree of alignment of the particle crystallites. To characterize the porosity, image analysis was performed using code written in matlab. Probability densities were determined for the size and shape of the macroporosity. Furthermore, a preferred orientation was observed for all grades characterized. The code for two-dimensional analysis used for the corresponding publication is currently being modified to analyze three-dimensional input data from μX-ray CT scans and will be published in a future journal article.

In Chapter Five, the oxidation of NBG-18 nuclear graphite was studied. A reaction model was developed based upon the actual oxygen transfer mechanism for the graphite-oxygen reaction system. The parameters are therefore physically meaningful and directly related to individual elementary reaction rates within the mechanism. The Arrhenius parameters are in excellent agreement with experimental and theoretical measurements of the same elementary reactions. Given the wide variety of high-purity graphite sources used in this literature and excellent agreement between measured and predicted values, the developed intrinsic model should be applicable to all nuclear-grade graphites. Moreover, the model can be extrapolated outside the experimental temperature and pressure range with much larger degrees of certainty due to the relationship of the fitted parameters to the physical reaction mechanism.

TABLE OF CONTENTS

LIST OF TABLES

LIST OF FIGURES

LIST OF ABBREVIATIONS

HTGR	High Temperature gas-cooled Reactor
VHTR	Very High Temperature Reactor
TEM	Transmission Electron Microscopy
HREM	High Resolution Electron Microscopy
EELS	Electron Energy Loss Spectroscopy
SAED	Selected Area Electron Diffraction
FFT	Fast Fourier Transformation
DFT	Density Functional Theory
TSA	Total Surface Area
BET	Brunauer-Emmett-Teller
ASA	Active Surface Area
RSA	Reactive Surface Area
SCCM	Shrinking Cylindrical Platelet Model
OTM	Oxygen Transfer Model

CHAPTER ONE: INTRODUCTION

This dissertation is composed of four papers published in three journals, Microscopy and Microanalysis (Chapter Two), Journal of Nuclear Materials (Chapters Three and Four), and Carbon (Chapter Five). Chapters Two and Three utilize transmission electron microscopy to characterize the different microstructures in nuclear graphites and atomic level defects in an irradiation environment. Chapter Four utilizes optical microscopy to determine the size and shape of the filler material and macro-porosity within the different grades. The final Chapter focuses exclusively on the oxidation of nuclear graphite and the development of an intrinsic oxidation model applicable to all grades of nuclear graphite.

Each chapter (publication) was written specifically for publication with intentional autonomy rather than as one fluid body of work. This does not mean however, that the work represents four completely unrelated subjects. The overarching theme among the chapters is the use of detailed microstructure characterization to better understand the underlying mechanisms and phenomena that limit the life of graphite within a high-temperature gas-cooled nuclear reactor (HTGR). If the mechanisms and phenomena are better understood, the lifetime of the graphite can be better predicted and a more certain forecast of a reactors safe operating lifetime may be made.

A more detailed introduction is given at the beginning of each chapter on the specific applications and motivation for the experimental work; however, a broad overview is given in the following sections of this chapter.

1.1 Graphite In Nuclear Reactor Applications

Nuclear reactors are one potential low-carbon emitting technology. Graphite is used in HTGRs as a moderator and structural component due to its exceptional moderating properties (its high scattering and low neutron absorption cross section), compressive strength, high thermal stability, easy machinability, and cost effectiveness [1]. The future generation IV very high temperature reactor (VHTR) design is the most advanced very high-temperature reactor design. It will be helium cooled and operated with core outlet temperatures in the range of 850 to 1000 °C. The VHTR has the potential to be quite versatile in application because of its range of end energy products. These include high-efficiency electricity production (~50% efficiency), hydrogen production from water, and production of high-quality steam critical to many industrial high temperature applications. While graphites have been use in the past for high temperature gas reactor programs in the United States, these graphites are no longer available and newer generations of graphite must therefore be used.

1.2 Need for Characterization of Candidate Nuclear Graphites

Graphite is a complicated and complex material in that the initial source of carbon as well as variations in coke type, its quantity of filler (relative to binder and later densification impregnations), forming process, and heat treatments will produce a relatively wide spread distribution of initial properties [2-4]. Thus properties and their inherent variability must be tested and validated, prior to use in a nuclear reactor, for new nuclear graphites any time a previous carbon source material is no longer available. Some of the key properties of interest are the dimensional change, mechanical and thermal properties, and the oxidation resistance of graphite in an air or moist environment.

1.2.1 Irradiation-Induced Property Change

Irradiation-induced changes in graphite during reactor operation are strongly linked to the virgin microstructure of the graphite under investigation and are therefore affected by the carbon source material and processing.

Under irradiation, nuclear graphite undergoes complex dimensional changes. During irradiation of a graphite single crystal, carbon atoms are displaced, resulting in the accumulation of interstitial loops between the basal planes. This accumulation over time begins to increase the inter-planar distance between graphene sheets. The interstitial clusters eventually coalesce and rearrange to form new basal planes resulting in an overall expansion along the c-direction and contraction in the a-direction which is explained by the formation of vacancy loops.

In a bulk (polycrystalline) nuclear graphite the material will initially shrink with increasing irradiation dose before reaching a “turn-around” dosage after which the material begins to swell. Presently this is believed to be explained by the accommodation of swelling provided by microcracks parallel to the basal plane. The microcracks accommodate the expansion in the c-direction of the cyrstallites resulting in a net shrinkage at lower irradiation dosages provided by a-axis shrinkage [5-7]. Once the microcracks have closed and are no longer able to accommodate swelling (the “turn-around”), the bulk material begins to swell.

The major focus of Chapter Two and Three was the thorough pre-irradiation characterization of the nuclear graphite microstructures. This work when combined with thorough post-irradiation characterization will yield valuable information regarding the phenomena and mechanisms involved in irradiation shrinkage, swelling, and creep of nuclear graphite. Chapter Two focused on the microstructure and Chapter Three focused on the *in-situ* observation of the atomic level defects responsible for shrinkage and swelling using an electron beam. The work in both these chapters made extensive use of transmission electron microscopy.

1.2.2 Bulk Microstructure Changes

While Chapters Two and Three focus on characterization of nuclear graphite on the nano- and atomic-scale respectively, Chapter Four focuses on the initial characterization of microstructural features of the filler particles and macro-porosity. Thorough examination of the size, shape, and orientation of these features can yield valuable insight as the link between properties and microstructure. Data from the original publication has already been used by Contescu *et al.* [8] to partially rationalize and predict differences in the oxidation rate of different graphite grade. Characterization of these micro-scale features pre- and post-irradiation may also provide valuable insight into some of the bulk properties changes as well.

1.3 Oxidation of Nuclear Graphite

1.3.1 Significance of Carbon Combustion

The combustion of carbon is arguably the most important and extensively investigated high-temperature reaction. Modern society and the world as we know it would not be possible without its utilization. In 2009, it was estimated that approximately 41% of worldwide electricity production, came from coal-fired power plants [9]. As energy demand continues to climb globally, governments and industries alike have begun to investigate alternative low-carbon emitting technologies to lessen the effects of emitted carbon dioxide on climate change. Nuclear power is one such viable alternative to fossil energy. Ironically, in nuclear reactors the oxidation of graphite (carbon) is still an important consideration.

1.3.2 Graphite Oxidation In Nuclear Reactors

Since helium is used as the coolant within the VHTR design, oxidation is not a concern for normal or ideal operation; however, if a significant quantity of air or water were to reach the graphite within the reactor, its long-term structural integrity could be compromised. Thus, the oxidation of reactor graphite is an important consideration in reactor design and safety analysis.

There are two main scenarios of concern for oxidation of reactor graphite: acute and chronic exposure. Acute exposure is considered to be an accident scenario where there has been a depressurized loss of forced convection of the helium in the primary system followed by continual air flow to the reactor core. In such an extreme accident scenario the primary concerns are: 1) oxidation of the graphite structure to a degree that its integrity is compromised, 2) release of fission products that have been absorbed in the graphite structures, 3) exposure of fuel containment to oxygen and subsequent release of fission products after graphite fuel elements have been oxidized [10]. Also of interest is the long-term (chronic) exposure of the graphite to minor oxidizing impurities in the helium coolant such as O_2 and H_2O and their effects on the integrity of the graphite components.

1.3.3 Complications in Determining a Graphite-Oxygen Gas-Solid Reaction Rate

The oxidation literature for nuclear graphite shows a great deal of discrepancy from grade to grade and even within a grade between experimenters. Typical activation energies determined lie in the range of 170-210 kJ/mol [11-18], although activation energies as high as 505 kJ/mol and as low as 123 kJ/mol have been reported [19-22]. Much of this variation seen in the nuclear graphite literature can be attributed to three phenomena which are dependent upon the microstructures of the different grades as well as the size and geometry of the specimen.

1.3.3.1 Oxygen Transport Limitations

The first phenomenon is transport of oxygen to the interior of the graphite specimen through the pore structures. As seen in Figure 1.1, during oxidation the density profile of graphite changes substantially as a function of temperature. This is directly related to the ability of oxygen to diffuse into the sample interior. At low oxidation temperatures, oxygen will fully penetrate the sample and oxidize the entire volume uniformly. At high oxidation temperatures, the rate of reaction increases substantially relative to the rate of diffusion into the sample interior and thus the reaction occurs primarily at the surface, which leaves the sample interior relatively unoxidized. Two samples that have lost the same amount of mass, but have been oxidized at different temperatures, will likely have markedly different density profiles and thus substantially different mechanical properties.

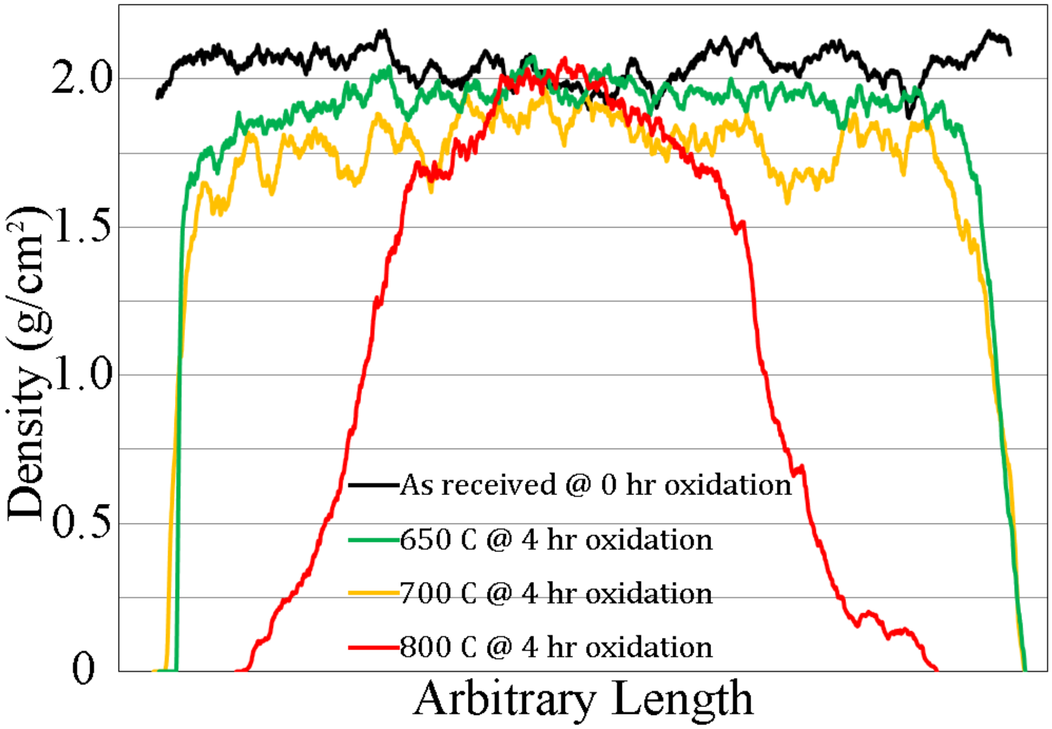

Figure 1.1 Oxidized NBG-18 Graphite Density Profiles. All samples initially started out at approximately 4.75 mm in thickness.

When oxygen is not able to penetrate deep into the sample interior, the rate of reaction is not uniform throughout the sample. This can cause significant variations in the determined rate for samples of different sizes.

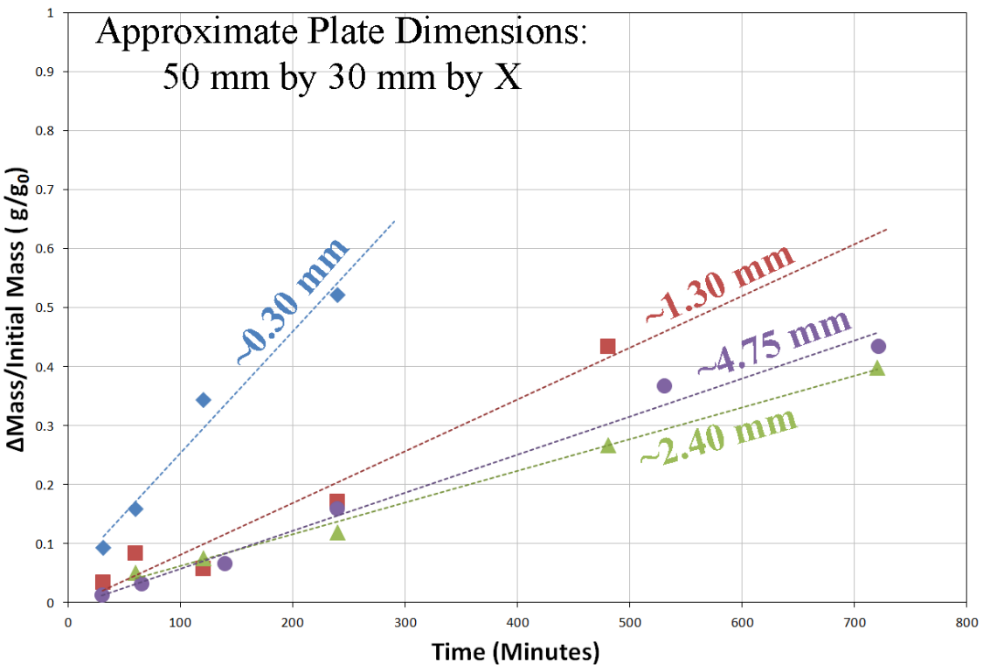

Figure 1.2 Effect of Size on Apparent Oxidation Rate. X represents the thickness of each set of graphite plates indicated next to the corresponding data set trend line.

As shown in Figure 1.2, the rate of oxidation changes with sample dimensions. As the sample volume increases the rate of reaction decreases. The 4.75 mm thick plates likely oxidized slightly faster than the 2.4 mm thick plates because of the available surface area for the chemical reaction.

1.3.3.2 Changing Surface Area

As oxygen diffuses into a graphite sample and reacts, carbon is removed from the surface of pores. Initially, the surface area increases due to the opening of pores originally isolated from the ambient environment. As oxidation continues and pores continue to grow, the porosity begins to interconnect and smooth which substantially decrease the surface area as shown in Figure 1.3. Since the rate of reaction is directly proportional to the amount of exposed surface area (assuming reactive surface area is directly proportional to total surface area, see Chapter Five), the apparent rate of reaction per unit volume will decrease with decreasing surface area. Thus a uniform apparent rate cannot be determined for the oxidation of graphite.

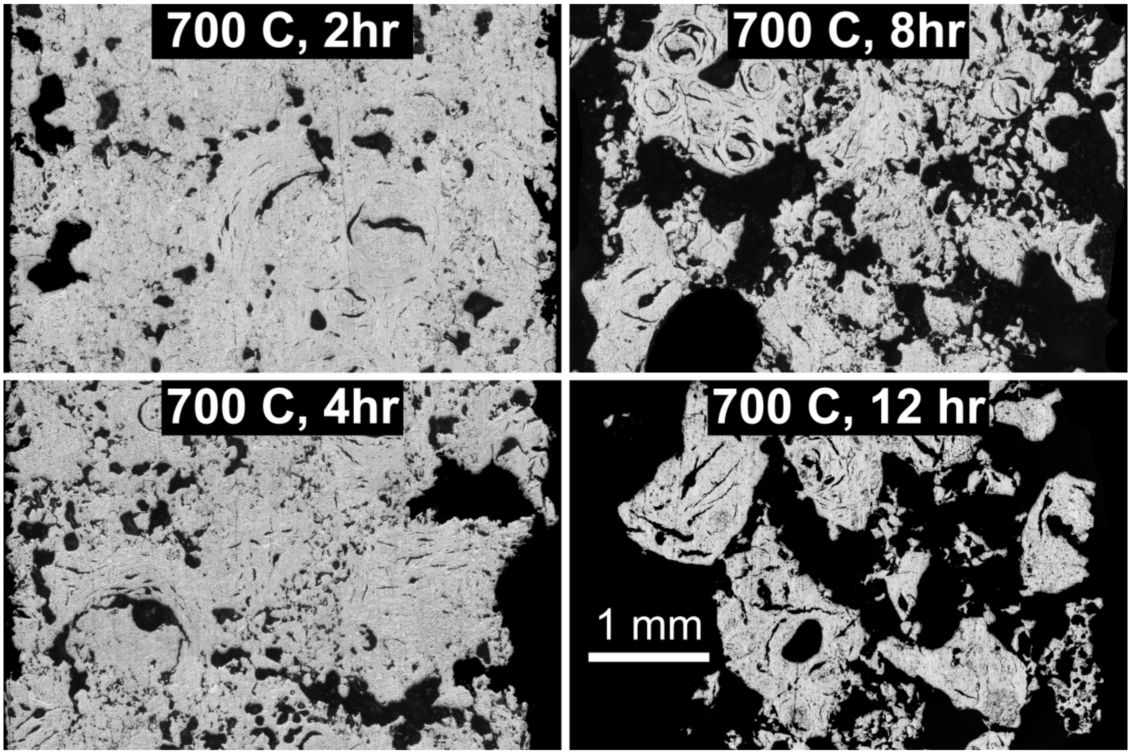

Figure 1.3 Oxidized 4.75 mm Thick Graphite Plates

1.3.3.3 Filler Versus Binder Oxidation Rate

Figure 1.3 shows large particles that remain relatively intact even after 8 and 12 hours of oxidation while a majority of the material around the particles is consumed. These particles are filler particles from the manufacturing process where as the material that has been consumed is a matrix material that holds the filler particles together [3]. From Figure 1.3 it is quite evident that the binder oxidizes faster than the filler, however this is an apparent effect due to crystallite size and arrangement of crystallites within the microstructure rather than an intrinsic difference in the oxidation rate (refer to Chapter Two).

1.3.4 Approach to Nuclear Graphite Oxidation

The effects discussed previously in section 1.3.3 make the determination of a rate of reaction very difficult to predict for a particular graphite. Assuming a rate can be determined, given the factors discussed above, the extrapolation of rates for lab sized samples to the monolithic material used in reactors would have a great deal of uncertainty. Moreover, if an accurate rate were to be determined for one graphite material, in all likelihood it would not be accurate for other grades (Section 1.2).

At an atomistic level each nuclear graphite grade has the same graphitic structure (refer to Chapter Two). It is therefore probable that at the atomic scale each graphite reacts at a nearly identical rate (refer to Chapter Five). If this is indeed the case, the size, shape, and arrangement of graphitic structures or lack thereof (porosity) at the nano- and micro scale (refer to Chapters Two and Four) are solely responsible for the differences in observed apparent rates of oxidation for nuclear graphites. If an intrinsic model for the oxidation of high-purity graphites was available, an apparent rate could hypothetically be determined for well characterized graphite.

1.4 References

[1] T. R. Allen, K. Sridharan, L. Tan, W. E. Windes, J. I. Cole, D. C. Crawford, and G. S. Was, “Materials challenges for Generation IV nuclear energy systems,” Nucl. Technol., 162 [3] (2008).

[2] R. Bratton and W. Windes, “NGNP graphite selection and acquisition strategy”;

ORNL/TM-2007/153-10-07 (INL/MIS-10-19427), Oak Ridge National Laboratory, July 28, 2010.

[3] W. P. Eatherly and E. L. Piper, “Manufacturing”; pp. 21-51 in *Nuclear Graphite*. Edited by R.E. Nightingale, Academic Press, 1962.

[4] R. E. Nightingale, “Structure”; pp. 87-115 in Nuclear Graphite. Edited by R.E. Nightingale. Academic Press, New York, 1962.

[5] W. Bollmann, “Electron Microscope Study of Radiation Damage in Graphite,” *J. Appl. Phys.*, **32** [5] 869-876 (1961).

[6] C. Baker, A. Kelly, “An electron microscope study of radiation damage in single crystal graphite,” *Phil. Mag.*, **11**[112] 729-746 (1965).

[7] A. Kelly and R. M. Mayer, “The influence of boron on the clustering of radiation damage in graphite. I. Electron microscope observations,” *Phil. Mag.*, **19**[160] 701-719 (1969).

[8] C. I. Contescu, T. Guldan, P. Wang, T. D. Burchell, “The effect of microstructure on air oxidation resistance of nuclear graphite,” *Carbon*, **50**[9] 5278-5285 (2012).

[9] World Coal Institute. The coal resource: a comprehensive overview of coal, 48. Available from: http://www.worldcoal.org/resources/wca-publications/; 2005 [cited 07.11.12].

[10] T. D. Burchell, R. Bratton, and B. Marsden, “Next Generation Nuclear Plant Phenomena Identification and Ranking Tables (PIRTS)”; Vol. 5 Graphite PIRT, USNRC, NUREG/CR-6944, ORNL/TM-2007/147, 2008.

[11] E. S. Kim and H. C. No, “Experimental study on the oxidation of nuclear graphite and development of an oxidation model,” *J. Nucl. Mater.*, **349**, 182-194 (2006).

[12] H. Yang, H. Eun, D. Lee, C. Jung, and K. Lee, “Analysis of combustion kinetics of powdered nuclear graphite by using a non-isothermal thermogravimetric method,” *J. Nucl. Sci. Technol.*, **43**, 1436-1439 (2006).

[13] H. Kawakami, “Air oxidation behavior of carbon and graphite materials or HTGR,” *Tanso*, **124**, 26-33 (1994).

[14] S. Chi and G. Kim, “Comparison of oxidation rate and degree of graphitization of selected IG and NBG nuclear grades,” *J. Nucl. Mater.*, **381**, 9-14 (2008).

[15] E. S. Kim, H. C. No, B. J. Kim, and C. H. Oh, “Estimation of graphite density and mechanical strength variation of VHTR during air-ingress accident,” *Nucl. Eng. Des.*, **238**[4], 837-847 (2008).

[16] L. Xiaowei, R. Jean-Charles, and Y. Suyuan, “Effect of temperature on graphite oxidation behavior,” *Nucl. Eng. Des.,* **227**[3], 273-280 (2004).

[17] H. K. Hinssen, K. Kühn, R. Moorman, B. Schlögl, M. Fechter, and M. Mitchell, “Oxidation experiments and theoretical examinations of graphite materials relevant for PBMR,” *Nucl. Eng. Des.*, **238**[11], 2018-2025 (2008).

[18] E. L. Fuller and J. M. Okoh, “Kinetics and mechanisms of the reaction of air with nuclear grade graphites: IG-110,” *J. Nucl. Mater.*, **240**, 241-250 (1997).

[19] M. S. El-Genk and J. P. Tournier, “Development and validation of a model for the chemical kinetics of graphite oxidation,” *J. Nucl. Mater.*, **411**, 193-207 (2011).

[20] M. S. El-Genk and J. P. Tournier, "Comparison of oxidation model predictions with gasification data of IG-110, IG-430 and NBG-25 nuclear graphite," *J. Nucl. Mater.*, **420**, 141-158 (2012).

[21] M. S. El-Genk and J. P. Tournier, "Validation of gasification model for NBG-18 nuclear graphite," *Nuc. Eng. Des.*, **250**, 142-155 (2012).

[22] R. Moormann, H.K. Hinssen, and K. Kühn, "Oxidation behavior of an HTR fuel element matrix graphite in oxygen compared to a standard nuclear graphite," *Nucl. Eng. Des.*, **227**, 281-284 (2004).

CHAPTER TWO: MICROSTRUCTURAL CHARACTERIZATION OF NEXT GENERATION NUCLEAR GRAPHITE*

This chapter is published by Cambridge University Press in *Microscopy and Microanalysis* and should be referenced appropriately.

Reference:

C. Karthik, J. Kane, D. P. Butt, W. E. Windes, R. Ubic, “Microstructural Characterization of Next Generation Nuclear Graphites.” *Micros. Microanal.*, **18**, 272-278 (2012).

Reproduced/modified by permission of the Cambridge University Press.

*This chapter includes modifications from the originally published version.

MICROSTRUCTURAL CHARACTERIZATION OF NEXT GENERATION NUCLEAR GRAPHITES

Chinnathambi Karthik[a,b]

Joshua Kane[a,b]

Darryl P. Butt[a,b]

William E. Windes[b,c]

Rick Ubic[a,b]

Accepted for publication in:

Microscopy and Microanalysis

April, 2012

[a]Department of Materials Science and Engineering, Boise State University,
1910 University Drive, Boise, ID 83725.

[b]Center for Advanced Energy Studies,
995 University Boulevard, Idaho Falls, ID 83415.

[c]Idaho National Laboratory,
2351 N. Boulevard, Idaho Falls, ID 83415.

Abstract

This article reports the microstructural characteristics of various petroleum and pitch based nuclear graphites (IG-110, NBG-18, and PCEA) that are of interest to the next generation nuclear plant program. Bright-field transmission electron microscopy imaging was used to identify and understand the different features constituting the microstructure of nuclear graphite such as the filler particles, microcracks, binder phase, rosette-shaped quinoline insoluble (QI) particles, chaotic structures, and turbostratic graphite phase. The dimensions of microcracks were found to vary from a few nanometers to tens of microns. Furthermore, the microcracks were found to be filled with amorphous carbon of unknown origin. The pitch coke based graphite (NBG-18) was found to contain higher concentration of binder phase constituting QI particles as well as chaotic structures. The turbostratic graphite, present in all of the grades, was identified through their elliptical diffraction patterns. The difference in the microstructure has been analyzed in view of their processing conditions.

2.1 Introduction

Nuclear graphite will be used in the next-generation very- high-temperature gas-cooled reactors owing to its excellent moderating properties (a high scattering and low absorption cross-section), high thermal stability, compressive strength, easy machinability, and cost-effectiveness [1]. Graphite will be used as a structural as well as moderator material. Even though the earlier gas-cooled reactors (e.g., Magnox, advanced gas reactor, etc.) demonstrated the feasibility of using graphite for commercial power-producing reactor components, the historic nuclear grades of graphite no longer exist; therefore, it is imperative to characterize the new grades of graphite and demonstrate that they exhibit acceptable properties in both the non-irradiated and irradiated state. Furthermore, the microstructure-property relation in irradiated nuclear graphites is poorly understood, probably due to the complexity of the microstructure.

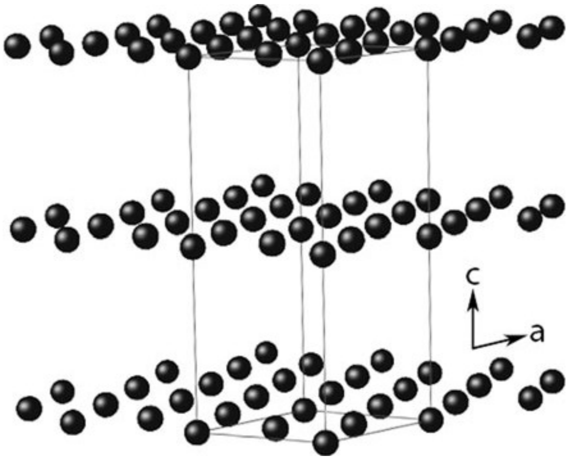

Figure 2.1 Schematic showing the layered crystal structure of graphite along with the unit cell outline.

Single crystalline graphite has a layered structure formed by stacking of sheets of hexagonal rings of carbon atoms (graphene). The commonly found hexagonal structure of bulk graphite results from the ABAB, stacking of these graphene sheets perpendicular to the c-axis (Figure 2.1). The distance between these sheets, also called as basal planes, is 0.335 nm. The bonding between the in-plane carbon atoms is strong, while the interplanar bonding is relatively weak resulting in more open space between the layers and highly anisotrophic physical properties. Nuclear graphite is an artificially-produced high-purity, polycrystalline material with a complex microstructure [2]. It is manufactured from coke particles (petroleum or pitch coke). Petroleum coke is obtained as a by-product of refining petroleum crude, whereas pitch coke is derived from coal tar, which is obtained as a by-product during the carbonization of coal. Coke is basically a carbonaceous material containing lamellar domains of large polycyclic aromatic molecules along with small quantities of ash and other impurities. Filler particles are manufactured by calcining the raw coke at temperatures around 1300 °C to remove the volatile hydrocarbons. This calcined coke is then crushed and sized as needed. These filler particles are mixed with a pitch binder at 165 °C. Binder is a thermoplastic material, composed of thousands of different hydrocarbons (mostly aromatic compounds), derived from the distillation of coal tar. The resulting filler-binder mixture is cooled and formed into a rigid green body (via extrusion, molding, or isostatic pressing). The green body is baked at 1000 °C, which results in the pyrolysis of the pitch and hence the evolution of a large volume of volatile gas. The baked material is impregnated further with pitch binder to increase the density and graphitized in an inert atmosphere at temperatures ranging from 2500 to 3000 °C for several weeks. This process results in a polycrystalline material with a complex microstructure constituting several different graphite phases such as filler particles, binder phase, and quinoline insoluble (QI) particles (from the binder) [2-5]. It also contains a large volume of macro- and micropores, resulting from gas evolution, as well as macro- and microcracks (also called Mrozowski cracks) [4]. Graphite has a very high c-axis thermal expansion coefficient, and a large contraction on cooling from graphitization temperatures results in the formation of microcracks perpendicular to the c-axis. These microcracks form as a result of delamination of the graphite basal planes and hence are aligned parallel to them. The width of these microcracks varies from nano- to micrometer scale while their length is on the micrometer scale.

The fast neutron damage of graphite moderators leads to the displacement of carbon atoms that significantly modifies the microstructure and hence the bulk properties. Under irradiation, graphite crystallites undergo dimensional changes that involve expansion along the c-axis and shrinkage parallel to the basal planes [2, 6]. The common explanation for these changes is that the ballistic displacement of carbon atoms, caused by irradiation, results in the accumulation of interstitials between the basal planes, forcing them apart [7-8]. These interstitial carbon clusters eventually rearrange to become new basal planes, resulting in the expansion along the c-axis with a concurrent shrinkage along the a-axis postulated to be due to the collapse of basal plane vacancies. In polycrystalline graphite, the microcracks can accommodate the c-axis expansion resulting in net shrinkage at lower doses of irradiation [9].

Ballistic displacement of atoms also results in significant creep even at room temperature [10], whereas significant thermal creep requires very high temperatures in excess of 2000 °C. The irradiation induced point defects result in an increased Young's modulus (attributed to the pinning of dislocations) and a decrease in thermal conductivity (due to increased phonon scattering by vacancy clusters) [11]. Since all of these processes alter the microstructure, it is important to fully understand the virgin microstructure-property relationship of each new grade. In this article, the authors have investigated and compared the microstructural features of three different commercial grades of nuclear graphite, NBG-18 and PCEA, which are new grades with potential applications in the next generation reactors, as well as IG-110, which is a historic reference grade.

2.2 Materials and Methods

Transmission electron microscope (TEM) samples of these graphites were prepared by conventional sample preparation techniques. Bulk samples of NBG-18 (SGL Group, Wiesbaden, Germany), PCEA (GrafTech International, Parma, OH, USA), and IG-110 (Toyo Tanso Co., Kagawa, Japan) were obtained from the manufacturers. Disks of 3 mm diameters were cut from the as-received bulk graphite using a diamond saw. These disks were further thinned mechanically to approximately 20-30 μm thick. A precision ion polishing system (Gatan PlPS 691; Gatan, Inc., Pleasanton, CA, USA) was used to achieve the final electron transparency. Ion-milling conditions were optimized to minimize the ion-beam damage. Typically, the samples were milled for about 60-70 min at 5° followed by a low angle milling step at 2° for 10 min. Electron microscopy studies were performed at room temperature on a 200 kV JEOL-2100 high-resolution TEM (JEOL Ltd., Tokyo, Japan).

2.3 Results and Discussion

Figure 2.2 shows the various microstructural features of the IG-110, which is fine-grained isotropic graphite fabricated via cold isostatic pressing. Petroleum coke is used as the filler material. Figure 2.2a shows what appears to be a filler particle (marked F) surrounded by binder (marked B) on both sides. The filler particles are lenticular in shape with sizes varying from a few tens of nanometer to tens of micrometers in length. The width varies from a few tens of nanometers to hundreds of nanometers. The lenticular shape arises from the shape of the starting coke particles. When the highly crystalline coke particles are crushed, they cleave parallel to basal planes resulting in a powder containing elongated particles with their crystallographic c-axis perpendicular to the length of the particles [2]. This means that the shape of the resultant filler particles depends on the crystallinity of the coke used. Petroleum coke is usually highly crystalline whereas pitch coke is usually less crystalline, resulting in more spherical filler particles. It should also be noted that the quality of the coke can vary depending on the crude oil/coal-tar pitch source used, affecting the shape distribution of the resultant filler particles significantly. Figures 2.2b and 2.2c are at a higher magnification and show the filler particles in different regions. The filler particles (as well as the binder) contain cracks running parallel to the basal planes. Microcracks are believed to form through delamination of the basal planes as a result of thermal contraction and play a major role in the irradiation induced dimensional change as well as the thermal expansion characteristics of the graphite. It was originally thought that these cracks would be void of any material; but interestingly, most are filled with amorphous carbon, the origin of which is not clear. This observation is in accordance with the recent study by Wen *et al*. [4], who despite preparing samples using several methods, noticed the presence of amorphous carbon in the microcracks in PGA grade nuclear graphite. The present authors show that this is a characteristic of all nuclear graphites irrespective of the manufacturing process and is found to be present in all the graphite grades under study.

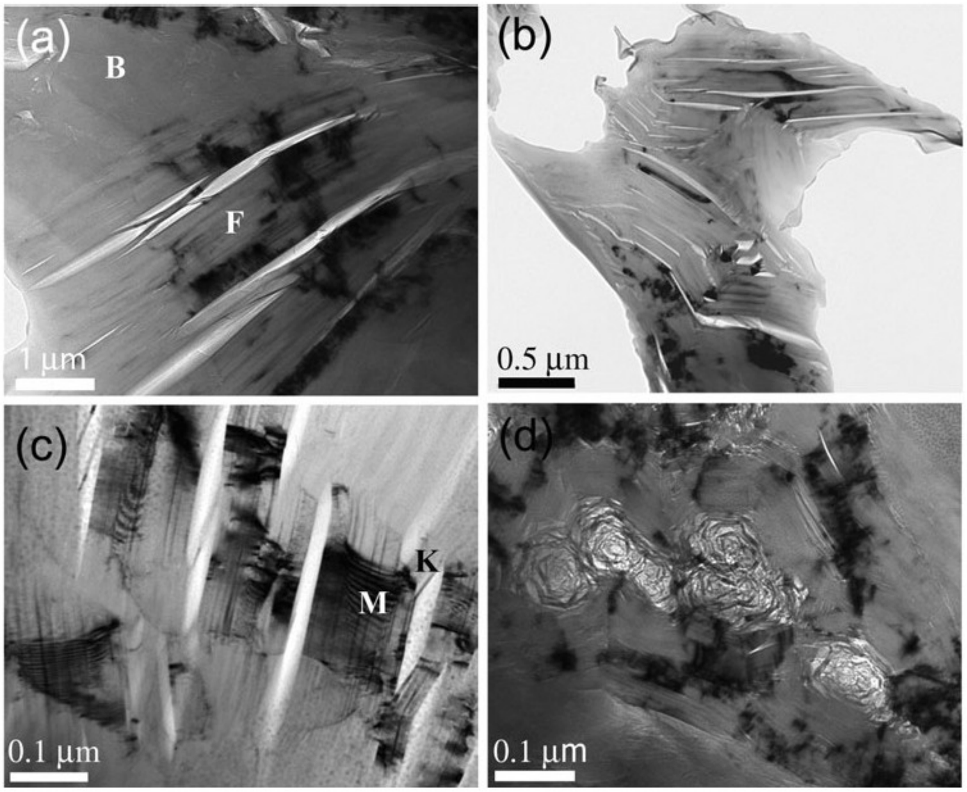

Figure 2.2 Bright-field TEM micrographs of IG-110 grade graphite: (a) interface region between a filler particle (marked F) and binder (marked B), (b) filler particle at high magnification, (c) filler particle with kink boundaries (marked K) and moire fringes (marked M), and (d) binder region.

Figure 2.2c shows the presence of delamination cracks with strands of inclined basal planes (marked K) bridging the bulk of the crystal across the cracks. These inclined strands, commonly known as kink bands, arise as a localized deformation mechanism in a variety of materials. Materials with layered structure such as graphite, boron nitrides, etc., subjected to compressive stresses, are especially prone to this kind of localized deformation [12]. Another interesting feature of Figure 2.2c is the presence of Moire fringes (marked M), which indicates the presence of twist boundaries that is confirmed by the selected area electron diffraction (SAED) pattern shown in Figure 2.3a. The [010] pattern clearly shows the arcing of the spots, indicating the presence of low-angle twist boundaries that may be a result of the delamination process.

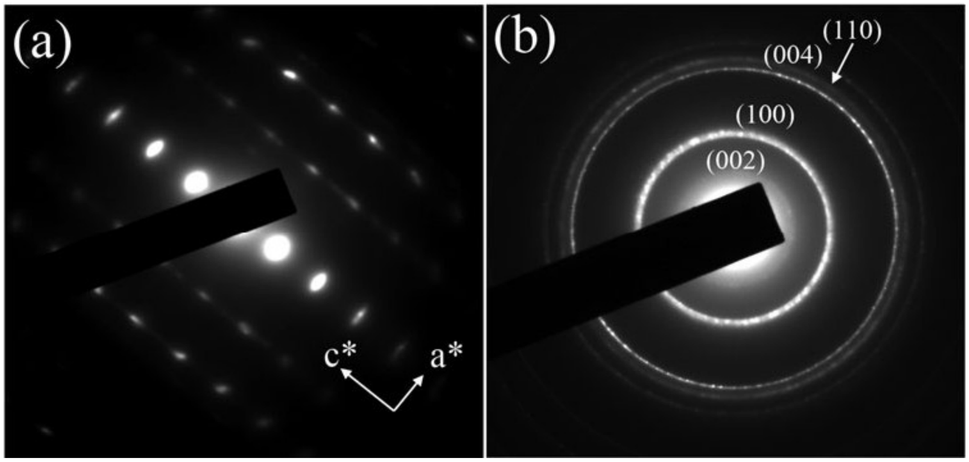

Figure 2.3 SAED diffraction pattern recorded from (a) filler particle and (b) rosette in the binder region of IG-110 graphite.

Figure 2.2d shows a micrograph recorded from the binder region. The binder region was found to contain well- graphitized crystallites of carbon with occasional rosette- structured particles embedded in them. Binder regions were also found to contain cracks similar to that of the filler particles. The rosette-shaped particles are well crystallized and are thought to originate from the QI fraction present in the pitch [2]. Even though it is very difficult to quantify the concentration of these particles using TEM due to the limited field of view and heterogeneity of microstructure, the authors estimated about 10-20 particles per square micron in the binder region. The size of these rosettes varied from 10 nm to a few hundreds of nano-meters in diameter. The SAED pattern recorded from a rosette is shown in Figure 2.3b with the prominent rings indexed as (002), (100), (004), and (110) planes. The ring pattern is a result of the continuous spiraling of the graphitic strands, which is equivalent to texturing in a direction perpendicular to the c-axis.

QI particles are basically solid particles similar to carbon black, composed of high-molecular-weight hydrocarbons [13-14]. These are formed either during the decomposition of coal or through the condensation of small aromatic molecules on the walls of the cracking chamber. It is believed that the aromatic molecules result in rosette-shaped particles constituting a spiral of graphite strands during graphitization. These strands are more disordered at the center of the rosettes. It can also be seen that these rosettes act as templates inducing the graphitization of binder around them in the form of wide concentric strands of graphite (marked with a dotted arrow in Figure 2.2d) retaining the crystallographic orientation of the outermost strand of the rosette. The concentration of QI particles in coal tars can vary from 2 to 12 wt% depending on the type of coal used and the production conditions. Unfortunately, the exact concentrations are proprietary and so not revealed by the manufacturers.

The presence of QI particles has been known to affect the mechanical properties of graphite [15]. Studies have shown the compressive strength of graphite to vary significantly with QI particle concentration, and there appears to be an optimum concentration where compressive strength is maximized. During baking, QI particles provide paths facilitating the escape of volatile species that reduces cracking and hence increases the strength of the final product [15].

Figure 2.4 shows the microstructural features of NBG-18 grade graphite. NBG-18 is vibrationally molded, near-isotropic graphite with pitch coke as the filler source. Figure 2.4a shows an interface region between a filler particle (marked F), binder phase (marked B), and turbostratic graphite (marked T). Figure 2.4b shows the close-up view of a filler particle delaminated into several fine stands (~10 nm in width) of graphite resulting in numerous microcracks.

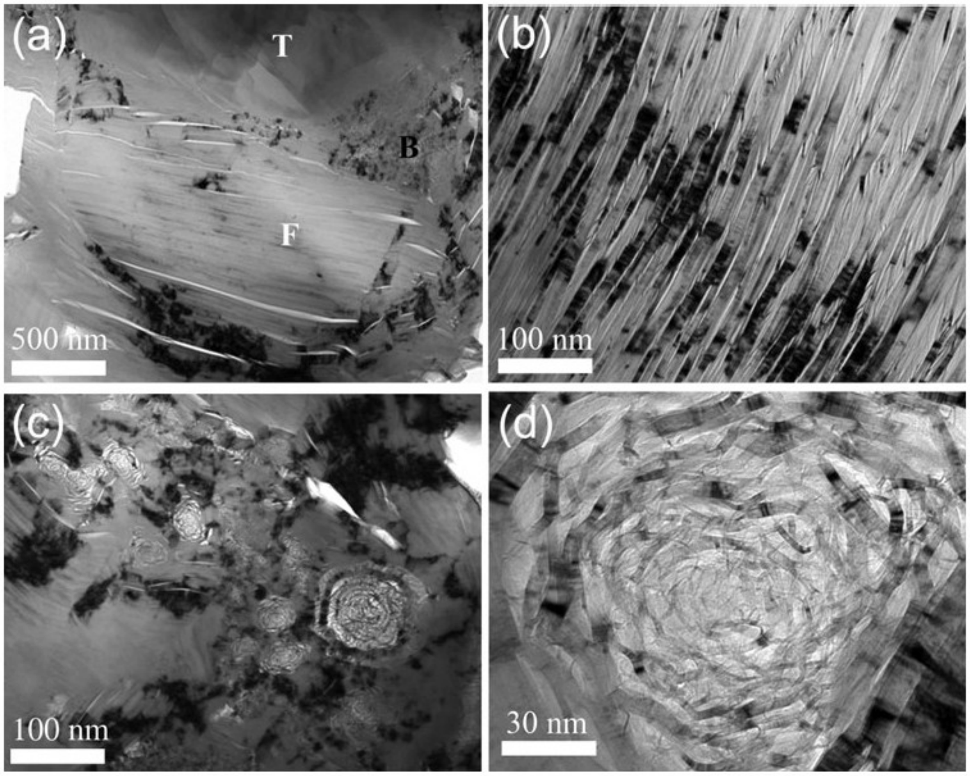

Figure 2.4 Bright-field TEM micrographs of NBG-18 grade graphite: (a) interface region constituting filler (marked F), binder (marked B), and turbostratic graphite (marked T), (b) filler particle at higher magnification, (c) binder region, and (d) rosette (QI particle) at high magnification.

Several filler particles with such fine strands were observed while other particles exhibited only a few cracks, similar to IG-110. One of the striking features of the NBG-18 microstructure is the high concentration of both binder and QI particles (Figure 2.4c) compared to other grades under study. The authors observed the presence of QI particles of varying sizes in a given square micron of binder. One of the reasons for the high concentration of the QI particles could be the usage of coal-tar pitch (as the binder source) which naturally tends to have a high concentration of QI particles [2]. Figure 2.4d is a high-magnification image depicting the internal structure of a QI particle, and the diffraction pattern obtained was similar to that in Figure 2.3b. The interior of QI particles appears to be more chaotic in case of NBG-18 compared to other grades.

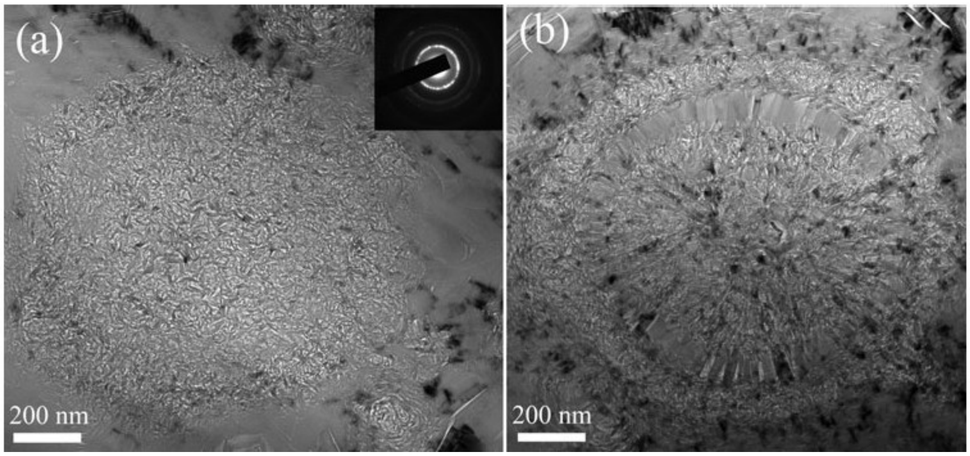

Figure 2.5 Bright-field TEM micrographs of spherical chaotic structures in NBG-18 grade graphite. Inset in (a) shows a typical SAED pattern recorded from these structures.

Apart from the QI particles, the binder phase in NBG-18 showed the presence of several other types of spherical chaotic structures as shown in Figure 2.5. These structures are of ~1 µm in diameter and packed with randomly oriented well-crystallized graphitic strands. Similar structures have been observed in PGA grade graphite [5], which has a coal-tar pitch binder; therefore, it can be safely concluded that these structures are characteristic of coal-tar pitch based binders. The diffraction patterns recorded from these chaotic structures were similar to those of QI particles.

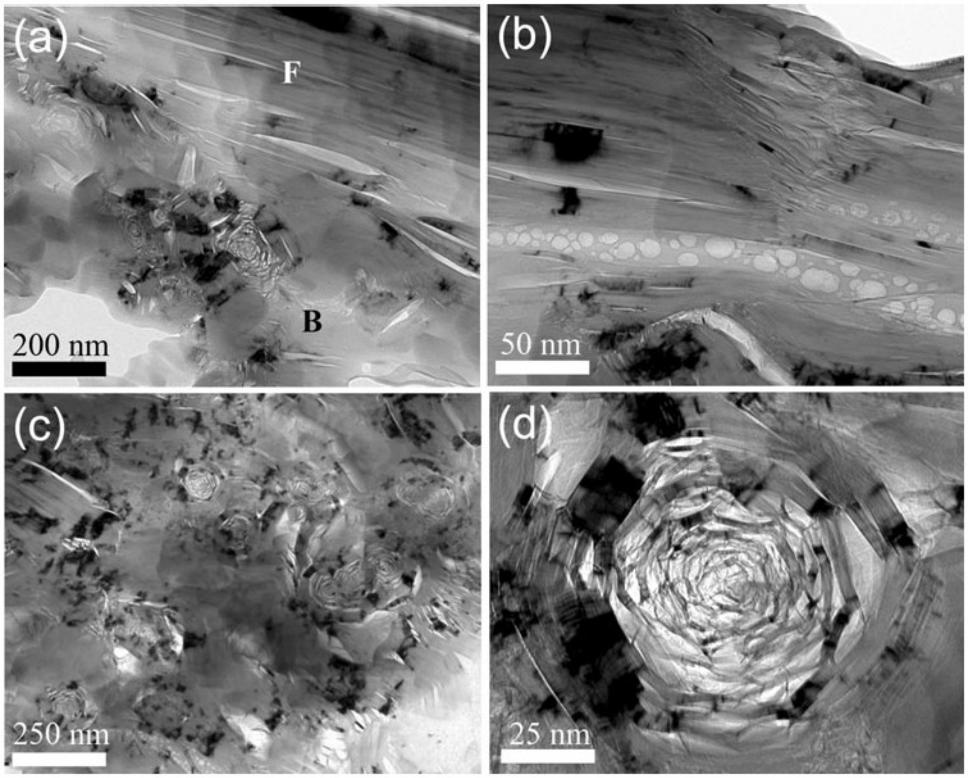

Figure 2.6 Bright-field TEM micrographs of PCBA grade graphite: (a) interface region constituting filler (marked F) and binder phase (marked B), (b) filler particle with cracks filled with porous amorphous carbon, (c) binder region, and (d) a rosette at high magnification.

The microstructural features of PCEA graphite, which is a nearly-isotropic. Extruded, petroleum coke based graphite, are depicted in Figure 2.6. Figure 2.6a shows an interface region between a filler particle (marked F) and binder phase (marked B) with embedded QI particles. Figure 2.6b shows the structure of a filler particle with microcracks. The microcracks in the case of PCEA appear to be wider than in other grades. Another distinct feature of PCEA is that the amorphous carbon filling the microcracks contains numerous voids. The sizes of these voids were found to vary in the range of approximately 1-25 μm in diameter. Figures 2.6c and 2.6d show the microstructure of the binder phase and a QI particle, respectively. The concentration of QI particles is comparable to that of IG-110. It should be noted that, unlike NBG-18, petroleum based pitch is used in the production of both IG-110 and PCEA, so they are expected to have negligible amounts of QI particles.

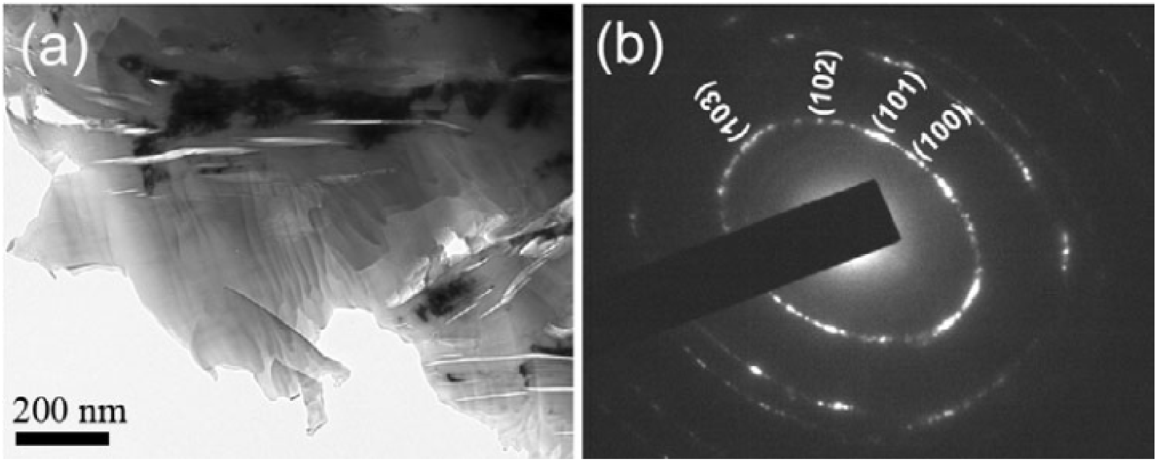

Figure 2.7 (a) Bright-field TEM micrograph of turbostratic graphite recorded from IG-110 grade graphite and (b) the corresponding SAED pattern.

Apart from the above-mentioned structures that constitute well-crystallized graphite, the authors also noticed the presence of turbostratic graphite in all the graphite grades. Figure 2.7 shows a typical microstructure of turbostratic graphite and the corresponding SAED pattern recorded from IG-110. Turbostratic graphites can be identified in a TEM by their elliptical diffraction patterns. Turbostratic graphite has packed carbon planes that are curled and rotated with respect to each other. In turbostratic graphite, the atoms are arranged in layers similar to graphite, but stacked randomly. The presence of simultaneous translational and rotational disorder results in the distribution of the scattering power in the reciprocal lattice in the form of concentric cylinders. The sectioning of these cylinders by the Ewalds sphere gives rise to a series of elongated spots that lie on one [16]. As pointed out by Vainshtein *et al*. [17], one could index the spots on one ellipse with the same *hk* indices but with different *l* indices as shown in Figure 2.7b. Turbostratic graphite can form during the process of graphitization or normal graphite can be converted to the turbostratic form by weakening the bonding between the layers by; for example, mechano-chemical activation [18]. There is also a possibility of the accidental insertion of Ar^+ ions between the layers during ion-milling resulting in turbostratic graphite. To verify this, TEM studies were carried out on powdered samples of graphite by dispersing the flakes of graphite particles on a TEM grid. TEM studies (Figure 2.8) showed the turbostratic graphite to be present even in the case of the powder samples. It confirms that the turbostratic graphite is an inherent characteristic of the nuclear graphite microstructure and not an artifact created by ion-milling.

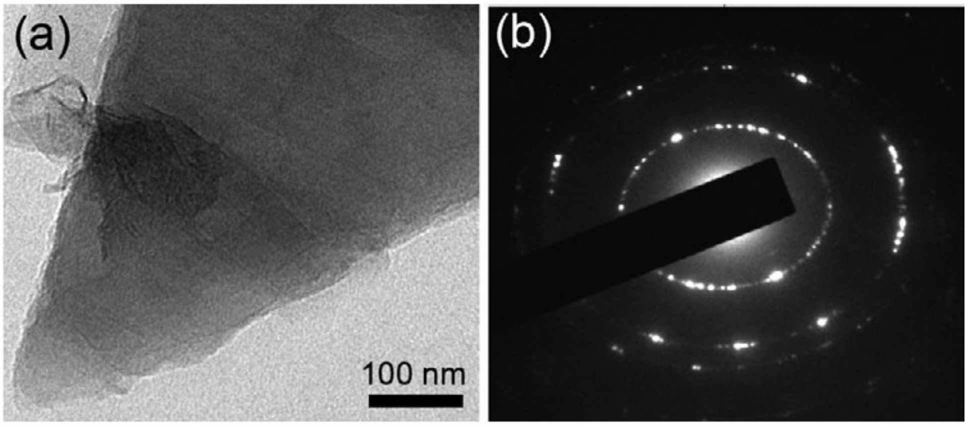

Figure 2.8 (a) Bright-field TEM micrograph and (b) SAED pattern recorded from powdered sample of IG-110 showing the presence of turbostratic carbon.

There have been several attempts in recent times to model the irradiation-induced property changes in graphite, especially Young's modulus and dimensional changes, and to identify the probable microstructural mechanisms [19-20]. These studies show that the changes in the physical properties under irradiation are highly dependent on the filler particle size as well as the porosity; however, the experimental results obtained from various test reactors have shown these changes to be highly complex providing very little insight into the microstructural mechanisms [10]. One of the reasons for the difficulty is the poor understanding of the part microstructure plays identifying the properties, and the authors hope that this article adds valuable information on that front.

2.4 Conclusions

The microstructure of various grades of next generation nuclear graphite has been studied by using transmission electron microscopy. Bright-field imaging was carried out to characterize the different constituents such as filler, binder, and microcracks that constitute the complex microstructure of the nuclear graphite. The size and shape of the microcracks were found to be different for different grades. The pitch based graphite contains higher concentration of binder phase as well as QI particles compared to other grades, which is attributed to the source of the binder (coal-tar pitch). The presence of turbostratic graphite in all of the grades under study was also observed.

2.5 Author Justification

The research presented in this publication was carried out and authored by Dr. Karthik Chinnathambi and Joshua Kane. Dr. Chinnathambi took on the responsibilities of lead author because of his expertise in the field of Transmission Electron Microscopy and experience in the publication process. Karthik and Joshua both contributed to the sample preparation, microscopy, and writing of the article. Joshua contributed heavily to the early drafts of the manuscript and remained critically engaged throughout the publication process in terms of editing and discussion. Joshua Kane's research was carried out as a partial fulfillment of the requirements for a Doctoral degree in Materials Science and Engineering at Boise State University, under the advisement and supervision of Dr. Darryl P. Butt. Dr. Rick Ubic, Dr. William E. Windes, and Dr. Darryl P. Butt contributed greatly in terms of financial support, detailed discussion features observed with respect to processing routes, and provided in-depth critical reviews of the article throughout the writing process.

2.7 References

[1] T. R. Allen, K. Sridharan, L. Tan, W. E. Windes, J. I. Cole, D. C. Crawford, and G. S. Was, "Materials challenges for Generation IV nuclear energy systems," *Nucl. Technol.*, **162**[3] (2008).

[2] R. E. Nightingale, "Structure"; pp. 87-115 in Nuclear Graphite. Edited by R. E. Nightingale. Academic Press, New York, 1962.

[3] A. N. Jones, G. N. Hall, M. Joyce, A. Hodgkins, K. Wen, T. J. Marrow, and B. J. Marsden, "Microstructure characterisation of nuclear grade graphite," *J. Nucl. Mater.*, **381**[1-2] 152-157 (2008).

[4] K. Y. Wen, J. Marrow, and B. Marsden, "Microcracks in nuclear graphite and highly oriented pyrolytic graphite (HOPG)," *J. Nucl. Mater.*, **381**[1-2] 199-203 (2008).

[5] K. Y. Wen, T. J. Marrow, and B. J. Marsden, "The microstructure of nuclear graphite binders," *Carbon,* **46**[1] 62-71 (2008).

[6] J. E. Brocklehurst and B. T. Kelly, "The microstructural modeling of nuclear grade

graphite," *J. Nucl. Mater.*, **353**, 12-18 (1993).

[7] P. A. Thrower and W. N. Reynolds, "Microstructural changes in neutron irradiated graphite," *J. Nucl. Mater.*, **6**, 221-226 (1963).

[8] M. Heerschap and E. Schüller, "Vacancy and interstial loops in graphite single crystals reactor-irradiated at 900 °C and 1200 °C," *Carbon* **7**, 624-625 (1969).

[9] W. Bollmann, "Electron Microscope Study of Radiation Damage in Graphite," *J. Appl. Phys.*, **32**[5] 869-876 (1961).

[10] J.H.W. Simmons, "Radiation Damage in Graphite"; Pergamon Press, Oxford, 1965.

[11] C. H. Wu, J. P. Bonal, and B. Thiele, "Thermal conductivity changes in graphites and carbon/carbon fiber material induced by low neutron damages," *J. Nucl. Mater.,* **212-215**, 1168-1173 (1994).

[12] M. W. Baroum, A. Murugaiah, S. R. Kalidindi, T. Zhen, and Y. Gogotsi, "Kink bands, nonlinear elasticity, and nanoindentations in graphite," *Carbon*, **42**, 1435-1445 (2004).

[13] I. Mochida, K. Maeda, and K. Takeshita, "Comparative study of the chemical structure of the disk-like components in the quinoline insoluble," *Carbon*, **16**, 469-467 (1978).

[14] P. A.Peaden, M. L. Lee, Y. Hirata, and M. Novotny, "High performance liquid chromatographic separation of high-molecular-weight polycyclic aromatic compounds in carbon black," *Anal. Chem.*, **52**, 2268-2271 (1980).

[15] M. S. Morgan, W. H. Schlag, and M. H. Wilt, "Surface properties of the quinoline-insoluble fraction of coal-tar pitch," *J. Chem. Eng. Data.*, **5**, 81-84 (1960).

[16] G. Schiffmacher, H. Dexpert, P. Caro, and J. M. Cowley, “Elliptic electron diffraction patterns from the films of turbostratic graphite,” *J. Microsc. Spectrosc. Electron.*, **5**, 729-734 (1960).

[17] B. K. Vainshtein, B. B. Zuyagin, and A. V. Avilov, “Electron diffraction structure analysis” in Electron Diffraction Techniques I. Edited by J. M. Cowley. Oxford University Press, New York, 1992.

[18] F. Salver-Disma, J. M. Tarascon, C. Clinard, and J. N. Rouzaud, “Transmission electron microscopy studies on carbon material prepared by mechanical milling,” *Carbon*, **37**, 1941-1959 (1999).

[19] G. Hall, B. J. Marsden, and S. L. Fok, “The microstructural modeling of nuclear graphite,” *J. Nucl. Mater.*, **353**[1-2] 12-18 (2006).

[20] M. R. Bradford and A. G. Streer, “A structurally-based model of irradiated graphite properties,” *J. Nucl. Mater.*, **381**, 137-144 (2008).

CHAPTER THREE: IN-SITU TRANSMISSION ELECTRON MICROSCOPY OF ELECTRON-BEAM INDUCED DAMAGE IN NUCLEAR GRADE GRAPHITE*

This chapter is published by Elsevier in *Journal of Nuclear Materials* and should be referenced appropriately.

Reference:

C. Karthik, J. Kane, D. P. Butt, W. E. Windes, R. Ubic, "In situ transmission electron microscopy of electron-beam induced damage process in nuclear grade graphite," *J. Nucl. Mater.*, **412**[3] 321-326 (2011).

Reproduced/modified by permission of the Elsevier.

*This chapter includes modifications from the originally published version.

IN-SITU TRANSMISSION ELECTRON MICROSCOPY OF ELECTRON-BEAM INDUCED DAMAGE IN NUCLEAR GRADE GRAPHITE

Joshua. Kane[a,b]

Chinnathambi. Karthik[a,b]

Darryl. P. Butt[a,b]

William. E. Windes[b,c]

Rick. Ubic[a,b]

Accepted for publication in:

Journal of Nuclear Materials

August, 2011

[a]*Department of Materials Science and Engineering, Boise State University,*
1910 University Drive, Boise, ID 83725.

[b]*Center for Advanced Energy Studies,*
995 University Boulevard, Idaho Falls, ID 83415.

[c]*Idaho National Laboratory,*
2351 N. Boulevard, Idaho Falls, ID 83415.

Abstract

Atomic level processes involved in the swelling and crack-closing in nuclear grade graphite under electron irradiation have been observed in real-time using transmission electron microscopy. Noise-filtered lattice images show the formation of vacancy loops, interstitial loops and resulting dislocations with unprecedented clarity. The dislocation dipoles formed via vacancy loops were found to undergo climb resulting in extra basal planes. Concurrent EELS studies showed a reduction in the atomic density because of the breakage of hexagonal carbon rings. The formation of new basal planes via dislocation climb in addition to the bending/breaking of basal planes leads to swelling and closing of microcracks.

3.1 Introduction

Artificial polycrystalline nuclear graphite will be used as a major structural and moderator material in high-temperature gas-cooled next-generation nuclear reactors [1]. Nuclear graphite has a complex microstructure consisting of filler particles, binder and microcracks parallel to the basal planes [2–4]. Since the historic nuclear graphite grades are no longer available, it is necessary to develop an understanding of irradiation induced dimensional and property changes in the current and future grades. For this reason, there has recently been renewed interest in the characterization of the properties of nuclear graphite [5–10].

Under irradiation, polycrystalline graphite undergoes complex dimensional changes, whereas single-crystalline graphite such as highly oriented pyrolytic graphite (HOPG) undergoes elongation in a direction perpendicular to the basal planes and shrinkage along the basal planes [2]. The present understanding is that the displacement of carbon atoms caused by irradiation results in the accumulation of interstitial loops in-between the basal planes forcing them apart. These interstitial clusters eventually rearrange to form new basal planes resulting in the expansion along the c-axis. The a-axis contraction is explained at present by the formation of vacancy loops. At present it is argued that the bulk changes in polycrystalline graphite can be explained by the orientation of the crystallites coupled with accommodation provided by micro- cracks oriented parallel to the basal planes [8]. The microcracks accommodate the c-axis expansion resulting in net shrinkage at lower doses of irradiation [11–13] provided by the a-axis shrinkage. However, this explanation was disputed by Tanabe *et al*. [14, 15], whose room temperature electron microscopic studies on carbon fibers did not show any evidence for the formation of interstitial basal planes and their existence at room temperature is controversial to date.

Niwase [16, 17] proposed a convincing model to explain the dimensional change as well as irradiation induced amorphization at lower temperatures based on the accumulation of partial dislocations, yet the nature of such dislocations remains unknown. The reasons for the lack of clear understanding of radiation induced microstructural changes is the complex microstructure of nuclear graphite as well as the difficulty in capturing the microstructural changes in real-time given the dynamic nature of the process. One of the ways to overcome these difficulties is to use electron-beam (as a substitute for neutrons) in a TEM to simulate the reactor environment which enables real-time observations. However, the dose rates of electron irradiation (~10^{-4} to 10^{-3} dpa/s) is much higher than neutron irradiation (~10^{-7} dpa/s). Furthermore, unlike electrons, neutrons and ions produce cascade damage owing to their heavier mass.

Nevertheless, the microscopic studies have shown the neutron-induced damage in graphite to be similar to that of electrons which is believed to be because of the large open space between the basal planes [18, 19]. The openness of graphite results in less dense neutron-induced cascade structures compared to other close-packed materials which combined with the lower neutron dose rates in usual reactor environments result in annealing of cascade structures leaving a small number of point defects between cascades. Koike and Pedraza [20, 21] have carried out detailed microscopic studies on HOPG as well as nuclear graphite and established the similarities between electron and neutron-induced damage processes. However, as pointed out by Pedraza [21] one should not directly compare the calculated dpa values because of the difference in the dose rates and the consequent difference in the rate of defect pairs generated.

In the present study, the room temperature electron irradiation induced swelling, crack-closing, and associated microstructural processes performed on next-generation nuclear-grade graphite (grade NBG-18) were observed in situ using a transmission electron microscope (TEM). The changes in the local lattice structure of nuclear grade graphite under electron irradiation, especially the evidence for the formation of interstitial loops have been shown with unprecedented clarity with the aid of noise-filtered high resolution electron microscopic (HREM) images obtained from videos recorded *in situ* electron energy loss spectroscopy (EELS) was also been used to monitor the changes in the bonding environment as well as the atomic density of the graphite.

3.2 Experimental

TEM samples of commercial nuclear-grade graphite, NBG-18 (supplied by SGL group, Germany), were prepared by conventional sample preparation techniques. Disks with 3 mm diameters were cut from the as-received bulk graphite. These disks were further thinned mechanically to approximately 100 µm thick. An ion-slicer (EM09100-IS, JEOL) was used to achieve the final electron transparency. Compared to conventional ion milling techniques, the ion-slicer is known to produce minimal beam damage to the samples. *In situ* electron irradiation and EELS studies were performed at room temperature on a 200 kV JEOL-2100 high resolution transmission electron microscope fitted with an EELS spectrometer (Enfina, Gatan). Since the irradiation induced processes were rapid, the whole process was captured in the form of a video. The noise reduction of the videos was carried out via notch-pass filtering of fast Fourier transforms. The entire filtering process was carried out using a MATLAB® code developed at Boise State University.

3.3 Results and Discussion

Figure 3.1a and b show the microstructure of NBG-18 taken from filler and binder regions respectively. The complex microstructure of nuclear graphite arises from the manufacturing process which involves mixing coke filler particles (petroleum or coal tar) with a binder (pitch). The microcracks seen in Figure 3.1a are formed due to the anisotropic crystal thermal expansion coefficient leading to delamination when the graphite billets cool from high graphitization temperatures. These microcracks play a vital role in determining the magnitude of irradiation induced swelling as they can accommodate crystalline swelling that occurs at lower irradiation doses. Fig 3.1b shows a region of binder which is embedded with rosette like particles which are resultant of graphitization of solid quinoline insoluble particles made up of high molecular weight aromatic molecules present in the pitch binder [4].

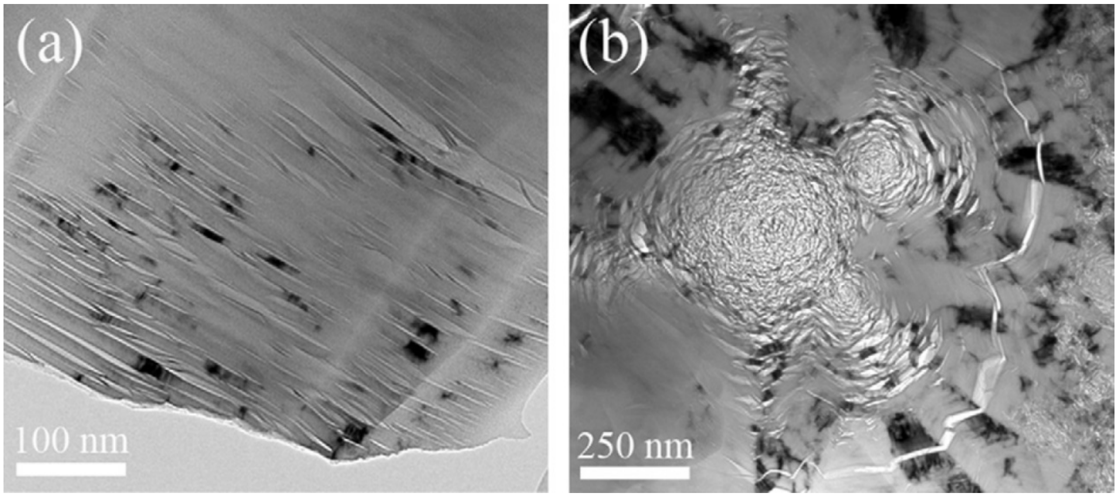

Figure 3.1 Bright field TEM micrographs showing the microstructure of NBG-18 nuclear-grade graphite recorded from (a) filler and (b) binder region.

The electron irradiation induced microstructural changes, in particular the closing of microcracks were studied in the filler particles where they are long and lenticular in nature and are believed to have the most influence on irradiation induced property changes. Fig 3.2 shows the effect of intense electron irradiation on the microcracks. The electron-beam was focused (~5 x 1021 electrons/cm-s) and positioned to cover the center of the microcrack with an initial width at the center of about ~20 nm. With increased irradiation, the graphite showed significant swelling and the crack closed completely after only 20 s irradiation time. The dosage, in terms of displacement per atom (dpa) was estimated to be approximately 1 dpa. A significant decrease in the diffraction contrast in the irradiated area as seen from Figure 3.2b indicates a decrease in the crystallinity in the graphite. Such behavior has been reported elsewhere [7].

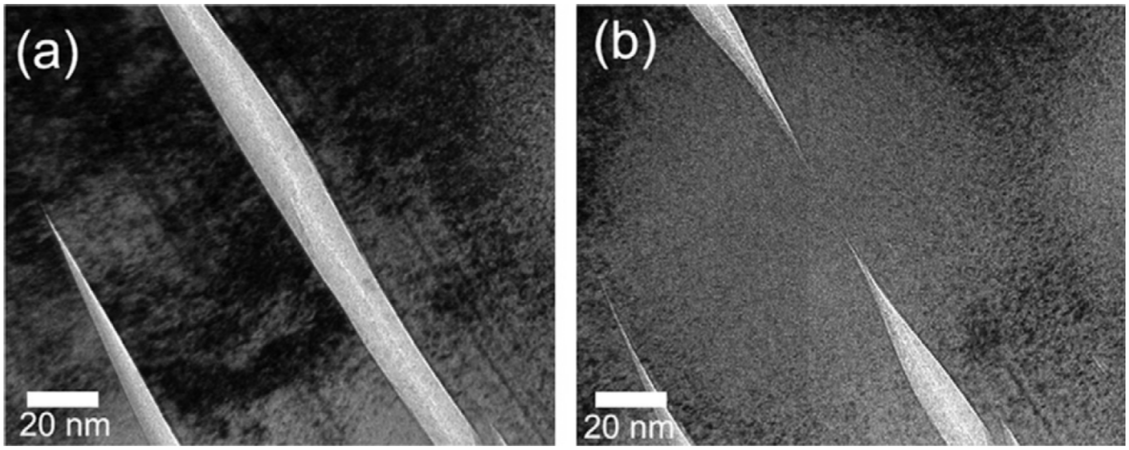

Figure 3.2 Bright field TEM micrographs showing the effect of electron irradiation on nuclear graphite; (a) shows a microcrack present in the as-prepared sample and (b) the same crack after ~ 1 dpa irradiation.

Fig 3.3a–c shows lattice images recorded along [1 0 0 0] depicting the sequential changes in the (0 0 0 2) basal planes associated with swelling and crack-closing induced by electron irradiation. The crack with a width which was ~20 nm seen in Figure 3.3a completely disappeared as seen in Figure 3.3c due to swelling of the crystallite from either sides. It is clearly shown that, with the increased electron dose, the graphite basal planes lose their long-range order with the formation of breaks and bends, eventually leading to randomization. The shape of the (0 0 0 2) reflections in the corresponding fast fourier transformation (FFT) patterns transformed from spots to arcs (Figure 3.4), which is an indication of fragmentation and rotation of the basal planes while still retaining a layered structure locally within a smaller scale of few nanometers as seen from the micrographs. The average (0 0 0 2) inter-planar spacing was estimated to increase approximately 13% from 3.6 nm to 4.2 nm.

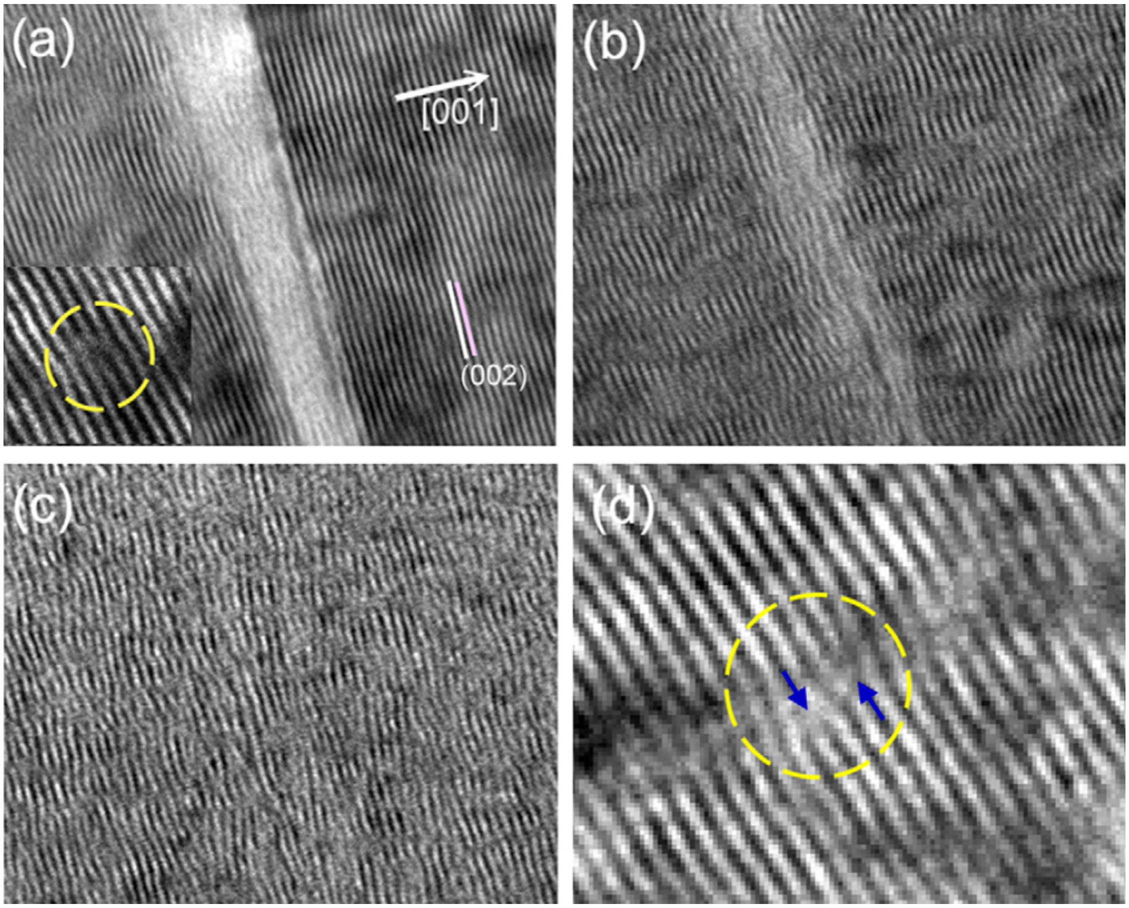

Figure 3.3 High resolution TEM images showing the effect of electron irradiation on the graphite lattice. (a)-(c) Recorded sequentially from as–prepared, ~0.5 dpa, and ~1 dpa irradiated samples. Inset in (a) shows the nucleation of vacancy loops. (d) Close up view of the lattice recorded after ~0.25 dpa showing the creation of dislocation dipoles; one such marked with a dashed circle.

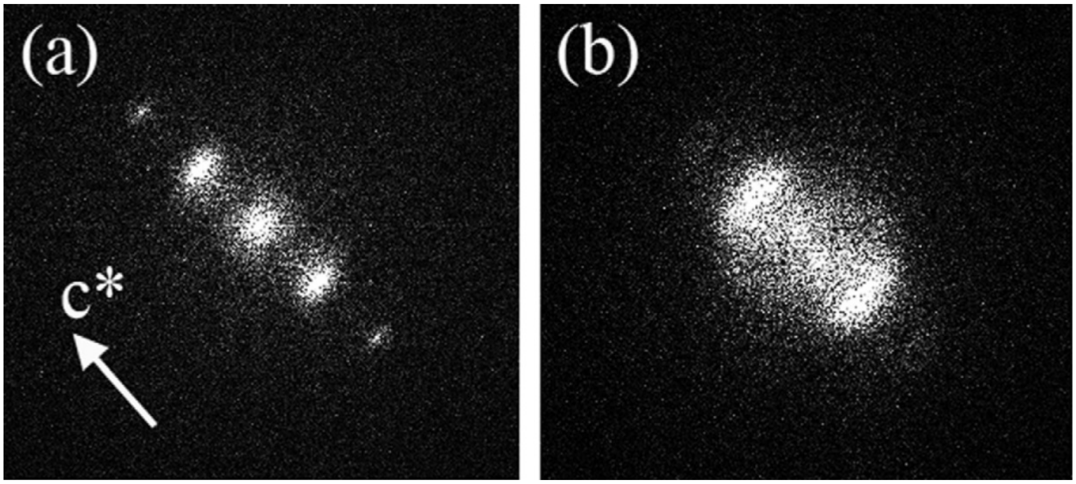

Figure 3.4 FFT of HREM images recorded from (a) as-prepared and (b) ~1 dpa irradiated sample.

During the initial stages of electron irradiation, the nucleation of numerous dislocation dipoles was observed, the concentration of which increased with increasing dpa. A high-magnification lattice image shown in Figure 3.3d depicts few of these dislocation dipoles (marked with arrows). These dislocations were created by the formation of vacancy loops (Figure 3.3a inset). These images are highly noisy due to the fast scan rate used to capture the rapid changes in the lattice structure. In order to observe these changes more clearly Figure 3.5a shows a noise-filtered HREM image, this clearly shows the nucleation of a vacancy loop (marked with arrows) which leads to the formation of a set of edge dislocations with opposite Burgers vectors as shown in Figure 3.5b. These two snapshots were captured at 1 s interval. Fig 5b also shows the nucleation of more vacancy loops. It should be noted that the ballistic displacement of carbon atoms under intense electron irradiation results in high concentration of vacancies and interstitials. According to Amelinckx and Delavigiette [22], these dislocation loops, formed due to the precipitation of vacancies are known to contain a low-energy single stacking fault (one layer of rhombohedral stacking) with a Burgers vector of $\frac{1}{2}\langle 0\ 0\ 0\ 1\rangle + \frac{1}{3}\langle -1\ 2\ 1\ 0\rangle$. Subsequent snapshots show that these dislocations move via positive climb as illustrated in Figure 3.5c. Fig 3.5c clearly shows the growth of the incomplete planes marked with arrows which effectively results in the formation of an extra basal plane. In the case of neutron irradiation, it has been assumed from TEM observations of irradiated graphite [23] that the formation of interstitial loops is the reason for the swelling along c-axis, but the images presented here for electron irradiation show that extra basal planes can form without the initial formation of interstitial loops.

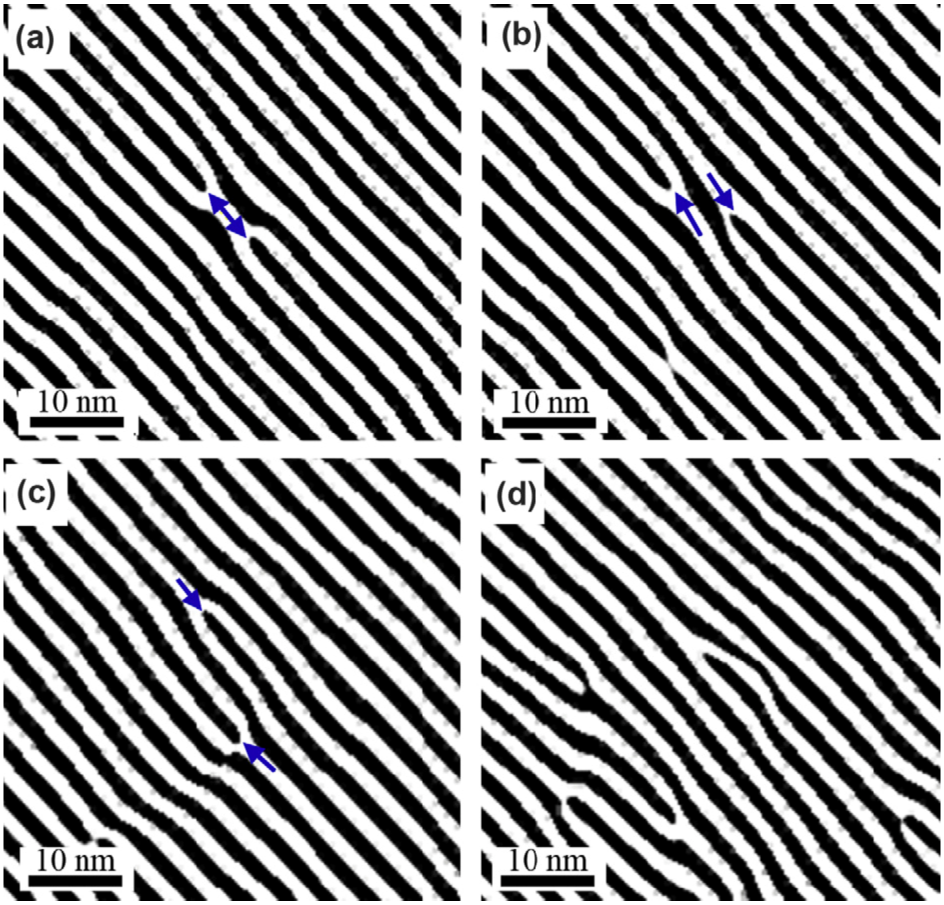

Figure 3.5 Noise filtered HREM images showing the formation of dislocation dipoles via vacancy loops (a) shows the nucleation of a vacancy loop (~0.25 dpa) dissociating itself into a set of dislocations as shown in (b) with the incomplete planes marked with arrows, (c) shows the growth of the incomplete planes via positive climb and (d) shows the accumulation of several dislocations at higher irradiation doses resulting in disordering of the graphite lattice. Distance between two black fringes corresponds to (0 0 0 2) inter-planar spacing (~0.36 nm).

It should be noted that the whole process is dynamic with numerous dislocations being constantly created and annihilated with only a few dislocations undergoing climb. Apart from vacancy loops, the formation of interstitial loops (precipitation of interstitials) was also observed as shown in Figure 3.6a and b. Figure 3.6a shows the bending of planes outward indicative of compressive stress exerted by interstitial cluster even though the loop is not resolvable by the Fourier analysis. According to Muto and Tanabe [15], the interstitial loops would require to be larger than half the sample thickness to be visible in HREM images. Fig 3.6b, a subsequent snap shot recorded after 1 s irradiation shows a more fully grown interstitial loop with a lateral length of about ~5 nm. Most of the loops observed in this work were of similar size. The interstitial loops of sufficient size are considered to introduce a new c layer in the ab stacking of hexagonal graphite. These types of interstitial loops, also referred to as prismatic dislocation loops are essentially partial dislocations with a Burgers vector of $\frac{1}{2}[0\ 0\ 0\ 1]$ [24]. These interstitial loops were found to be highly unstable and destroyed by further electron irradiation. With the increased irradiation, the concentration of dislocations also increased, leading to an increase in the concentration of broken graphite layers, eventually leading to more randomization as shown in Figure 3.5d. The complete real-time noise-filtered video of the above mentioned processes is provided in video 1.

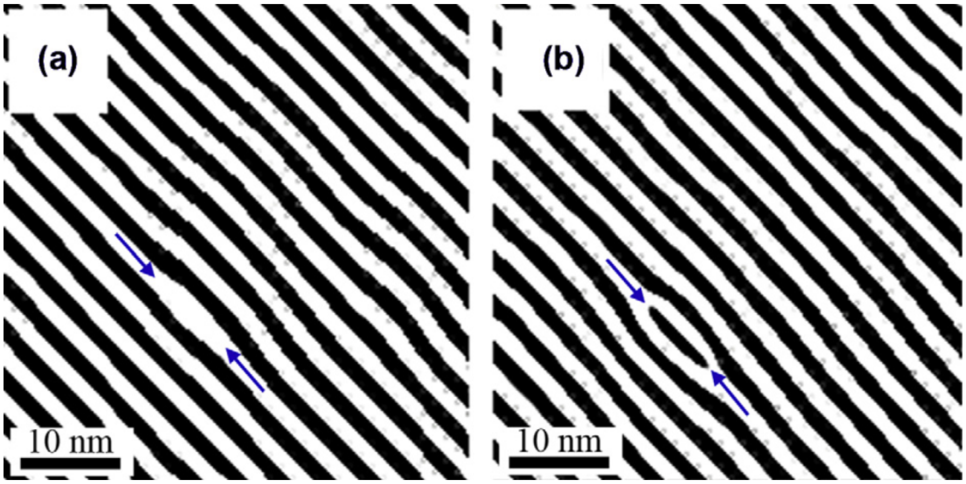

Figure 3.6 (a) Nucleation and (b) growth of an interstitial loop.

In order to obtain a better understanding of the implications of the electron irradiation damage on the atomic bonding, EELS was used to study the changes in the bonding environment associated with breakage and randomization of the graphite layers. Figure 3.7 shows the low-loss and core-loss EELS spectra recorded for as-prepared and after 1 dpa irradiation corresponding to the microstructures shown in Figure 3.3a and c. The low-loss spectrum shown in Figure 3.7a has two prominent features, a π-plasmon peak around 6 eV and π + σ plasmon peak around 25 eV. The π + σ plasmon peak showed a shift towards lower energies with an increase in the irradiation damage. The energy shift was 1.9 eV for 1 dpa irradiation. A shift towards lower energies indicates a reduction in valance electron density which could be indicative of a volume expansion or of structural transitions such as the formation of non-six sided carbon rings [25]. It should be noted that there is a weak π-plasmon peak still present even after 1 dpa irradiation indicating that the layered structure associated with p-bonds is retained, although largely aperiodic, even at this stage of irradiation, confirming the microstructural observations of the present study.

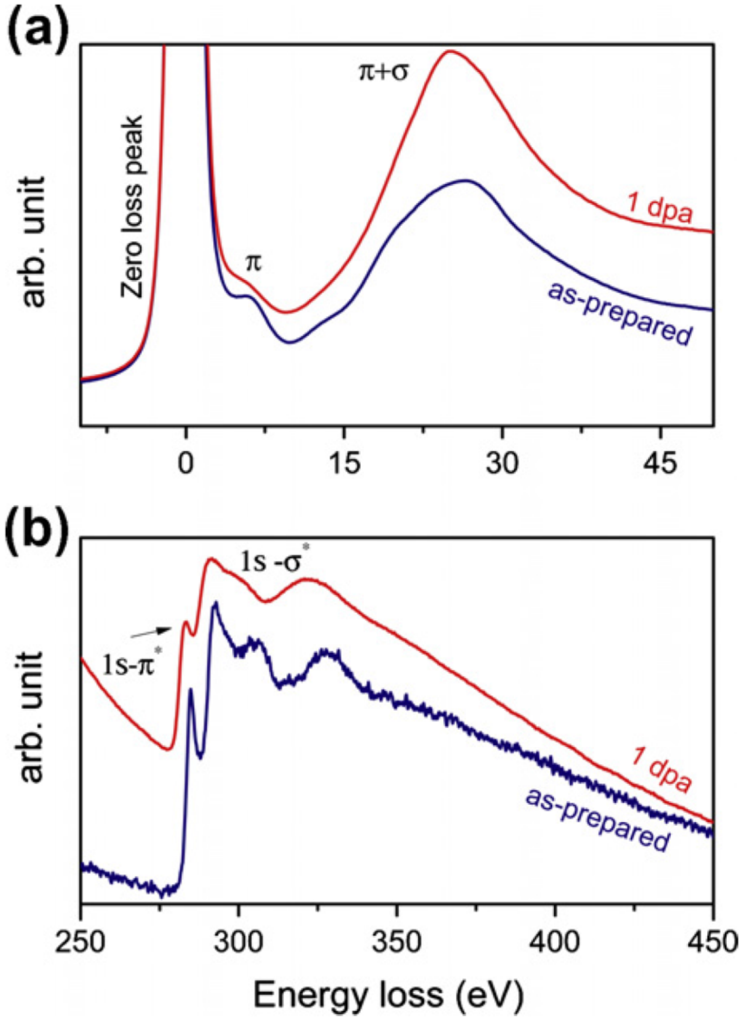

Figure 3.7 (a) Low-loss and (b) core-loss EELS spectra of the graphite recorded from the as-prepared and ~1 dpa irradiated graphite.

From the peak position (E_p) of the $\pi + \sigma$ plasmon peak, the change in the valence electron density (ne) of the graphite was calculated using a relationship based on the quasi-free electron model [26],

$$E_p = \frac{\hbar n_e e^2}{\varepsilon_0 m^*} \tag{3.1}$$

where m* is the effective mass of electrons (for graphite, m* = $0.87m_e$, where m_e is the free electron mass [27]) and ε_0 is the permittivity of free space. The mass density can then be estimated from ne using the atomic mass of carbon and the number of valance electrons per carbon. This method of calculating mass density has been used and verified by several authors [27, 28]. From Figure 3.7a, the densities of the as-prepared and ~1 dpa irradiated graphite have been estimated to be 2.28 g/cm^3 and 1.96 g/cm^3, respectively, which is an average fall in density drop of about 16%. It should be noted that the density of the as-prepared graphite is essentially the theoretical density of single-crystalline graphite (2.26 g/cm^3), which gives validation to this method.

The K-edge core-loss spectra for the corresponding doses are shown in Figure 3.7b. The spectra have two main features: a peak at ~285 eV and a maximum with extended fine structures at ~ 290 eV which are attributed to 1s-π* and 1s-σ* electronic transitions, respectively. It can be seen that the fine structure in the σ* peak disappeared with the formation of a broad peak, which is indicative of the formation of fullerene like structures [29]. This change indicates the deterioration of the long-range periodicity within the basal plane due to the formation of non-hexagonal atomic rings, which corroborates the previously calculated reduction in density. Apart from destroying the long range ordering, the dislocation dipoles are also believed to aid the formation of the so-called bucky onions [17] because the dipoles induce curvature of the basal planes which is consistent with the formation of bends and curves in the present case and may explain the changes observed in the EELS spectra. Recently, Chuvilin *et al*. [30] have shown in real-time the fullerene formation from a graphene sheet under electron irradiation. Also, the accumulation of interstitial carbon atoms themselves can induce, local buckling of basal planes by forming crosslinks between the basal planes.

Initially, the formation and growth of new interstitial planes as a result of accumulation of displaced carbon atoms were considered to be the sole reason for the macroscopic swelling of graphite along the c-axis, but there was no clear microstructural evidence creating doubt as to the above mentioned hypothesis for c-axis expansion [24]. In this work, clear evidence for the formation of interstitial loops at room temperature has been shown. However, the interstitial loops were found to be highly unstable and few in number, and therefore are unlikely to significantly contribute to the observed swelling. Hence, the authors believe that the observed swelling along c-axis and the closing of microcracks is mainly because of the new basal planes being introduced by the positive climb of dislocation dipoles created via vacancy loops. The dislocation climb involves the migration and effective accumulation of carbon atoms along c-axis leaving behind a high concentration of vacancies, the condensation of which on free surfaces might be a reason for the a-axis shrinkage. In addition, the significant reduction in density observed even at 1 dpa of electron irradiation shows the increase in the open nature of the lattice. As proposed by Niwase [16], as the dislocation dipoles increase in concentration, they introduce breaks, bends and curls in the basal planes, leading to the destruction of the lattice ordering and resulting in a more open structure which is confirmed from the increase in the measured lattice parameter and decrease in density as shown by EELS study.

3.4 Conclusions

The in situ HRTEM study and analysis of electron irradiation damage in graphite presented in this paper provides experimental evidence for the formation of vacancy loops and interstitial loops in graphite irradiated at room temperature. Dislocations were found to undergo positive climb resulting in the formation of extra basal planes which in addition to the reduction in atomic density as evidenced by EELS are believed to be responsible for the observed swelling and crack-closure.

3.5 Supplementary Materials

Supplementary data associated with this article can be found, in the online version, at doi:10.1016/j.jnucmat.2011.03.024.

3.6 Author Justification

The research presented in this publication was carried out and authored by Dr. Karthik Chinnathambi and Joshua Kane. Dr. Chinnathambi took on the responsibilities of lead author because of his expertise in the field of Transmission Electron Microscopy, Electron Energy Loss Spectroscopy, and experience in the publication process. Karthik and Joshua both contributed to the sample preparation, microscopy. Joshua contributed heavily to the early drafts of the manuscript and was responsible for the identification of analyzed defects though image processing and filtration. Joshua Kane’s research was carried out as a partial fulfillment of the requirements for a Doctoral degree in Materials Science and Engineering at Boise State University, under the advisement and supervision of Dr. Darryl P. Butt. Dr. Rick Ubic, Dr. William E. Windes, and Dr. Darryl P. Butt contributed greatly in terms of financial support, detailed discussion features observed with respect to processing routes, and provided in-depth critical reviews of the article throughout the writing process.

3.7 References

[1] T. R. Allen, K. Sridharan, L. Tan, W. E. Windes, J. I. Cole, D. C. Crawford, and G.

S. Was, “Materials challenges for Generation IV nuclear energy systems,” *Nucl. Technol.*, **162**[3] (2008).

[2] R.E. Nightingale, “Structure”; pp. 87-115 in Nuclear Graphite. Edited by R.E. Nightingale. Academic Press, New York, 1962.

[3] A.N. Jones, G.N. Hall, M. Joyce, A. Hodgkins, K. Wen, T.J. Marrow, B.J. Marsden, “Microstructure characterisation of nuclear grade graphite,” *J. Nucl. Mater.*, **381**[1-2] 152-157 (2008).

[4] K. Y. Wen, T. J. Marrow, and B. J. Marsden, “The microstructure of nuclear graphite binders,” *Carbon*, **46**[1] 62-71 (2008).

[5] B. J. Marsden, G. N. Hall, O. Wouters, J. A. Vreeling, and J. van der Laan, “Dimensional and material property changes to irradiated Gilsocarbon graphite irradiated between 650 and 750 °C,” *J. Nucl. Mater.*, **381**[1-2] 62-67 (2008).

[6] L .L. Snead, T. D. Burchell, and Y. Katoh, “Swelling of nuclear graphite and high quality carbon fiber composite under very high irradiation temperature,” *J. Nucl. Mater.*, **381**[1-2] 55-61 (2008).

[7] K. Y. Wen, J. Marrow, and B. Marsden, “Microcracks in nuclear graphite and highly oriented pyrolytic graphite (HOPG),” *J. Nucl. Mater.*, **381**[1-2] 199-203 (2008).

[8] G. Hall, B. J. Marsden, and S. L. Fok, “The microstructural modeling of nuclear graphite,” *J. Nucl. Mater.*, **353**[1-2] 12-18 (2006).

[9] T. D. Burchell and L. L. Snead, “The effect of neutron irradiation damage on the properties of grade NBG-10 graphite,” *J. Nucl. Mater.*, **371**[1-3] 18-27 (2007).

[10] T. D. Burchell, “Irraiation induced creep behavior of H-451 graphite,” *J. Nucl.*

Mater., **381**[1-2] 46-54 (2008).

[11] W. Bollmann, “Electron Microscope Study of Radiation Damage in Graphite,” *J. Appl. Phys.*, **32**[5] 869-876 (1961).

[12] C. Baker and A. Kelly, “An electron microscope study of radiation damage in single crystal graphite,” *Phil. Mag.*, **11**[112] 729-746 (1965).

[13] A. Kelly and R. M. Mayer, “The influence of boron on the clustering of radiation damage in graphite. I. Electron microscope observations,” *Phil. Mag.*, **19**[160] 701-719 (1969).

[14] T. Tanabe, S. Muto, and K. Niwase, “On the mechanism of dimensional change of neutron irradiated graphite,” *Appl. Phys. Lett.*, **61**[14] 1638-1640 (1992).

[15] S. Muto and T. Tanabe, “Damage process in electron-irradiated graphite studied by transmission electron microscopy. I. High-resolution observation of highly graphitized carbon fibre,” *Phil. Mag. A*, **76**[3] 679–690 (1997).

[16] K. Niwase, “Irradiation-induced amorphization of graphite: A dislocation accumulation model,” *Phil. Mag. Lett.*, **82**[7] 401-408 (2002).

[17] K. Niwase, “Formation of dislocation dipoles in irradiated graphite,” *Mater. Sci. Eng. A*, **400**, 101-104 (2005).

[18] J. H. W. Simmons, “Radiation Damage in Graphite”; Pergamon Press, Oxford, 1965.

[19] D. F. Pedraza, pp.437 in *Phase formation and modification by beam-solid interactions*, Mater. Res. Soc. Symp. Proc. **235** Pittsburgh, Pennsylvania, (1992).

[20] J. Koike and D. F. Pedraza,”Dimensional changes in highly oriented pyrolytic

graphite due to electron-irradiation," *J. Mater. Res.*, **9**[7] 1899-1907 (1994).

[21] D. F. Pedraza and J. Koike, "Dimensional changes in grade H-451 nuclear graphite due to electron irradiation," *Carbon*, **32**[4] 727-734 (1994).

[22] S. Amelinckx and P. Delavignette, "Dislocations loops due to quenched-in point defects in graphite," *Phys. Rev. Lett.*, **5** 50-51 (1960).

[23] P. A. Thrower and W. N. Reynolds, "Microstructural changes in neutron-irradiated graphite," *J. Nucl. Mater.*, **8** [2] 221-226 (1963).

[24] R. H. Telling and M. I. Heggie, "Radiation defects in graphite," *Phil. Mag.*, **87** [31] 4797-4846 (2007).

[25] M. Takeuchi, S. Muto, T. Tanabe, S. Arai, and T. Kuroyanagi, "Damage process in electron-irradiated graphite studied by transmission electron microscopy. II. Analysis of extended energy-loss fine structure of highly oriented pyrolytic graphite," *Phil. Mag. A*, **76**[3] 691-700 (1997).

[26] R. F. Egerton, "Electron Energy-Loss Spectroscopy in the Electron Microscope"; Plenum, New York, 1986.

[27] A. C. Ferrari, A. Libassi, B. K. Tanner, V. Stolojan, J. Yuan, L. M. Brown, S. E. Rodil, B. Kleinsorge, and J. Robertson, "Density, sp^3 fraction, and cross-sectional struction of amorphous carbon films determined by x-ray reflectivity ad electron energy-loss spectroscopy," *Phys. Rev. B*, **62**[16] 11089-11103 (2000).

[28] R. Haerle, E. Riedo, A. Pasquarello, and A. Baldereschi, "sp^2/sp^3 hybridization ratio in amorphous carbon from C 1s core-level shifts: X-ray photoelectron spectroscopy and first-principles calculation," *Phys. Rev. B*, **65**[4] 45101 (2001).

[29] M. Takeuchi, S. Muto, T. Tanabe, H. Kurata, and K. Hojou, “Structural change in graphite under electron irradiation at low temperatures,” *J. Nucl. Mater.*, **271**, 280-284 (1999).

[30] A. Chuvilin, U. Kaiser, E. Bichoutskaia, N. A. Besley, and A. N. Khlobystov, “Direct transformation of graphene to fullerene,” *Nature Chem.*, **2**[6] 450-453 (2010).

CHAPTER FOUR: MICROSTRUCTURAL CHARACTERIZATION AND PORE STRUCTRURE ANALYSIS OF NUCLEAR GRAPHITE*

This chapter is published by Elsevier in *Journal of Nuclear Materials* and should be referenced appropriately.

Reference:

J. Kane, C. Karthik, D. P. Butt, W. E. Windes, R. Ubic, “Microstructural characterization and pore structure analysis of nuclear graphite,” *J. Nucl. Mater.*, **415**[2] 189-197 (2011).

Reproduced/modified by permission of the Elsevier.

*This chapter includes modifications from the originally published version.

MICROSTRUCTURAL CHARACTERIZATION AND PORE STRUCTRURE ANALYSIS OF NUCLEAR GRAPHITE

Joshua. Kane[a,b]

Chinnathambi. Karthik[a,b]

Darryl. P. Butt[a,b]

William. E. Windes[b,c]

Rick. Ubic[a,b]

Accepted for publication in:

Journal of Nuclear Materials

August, 2011

[a]*Department of Materials Science and Engineering, Boise State University,*
1910 University Drive, Boise, ID 83725.

[b]*Center for Advanced Energy Studies,*
995 University Boulevard, Idaho Falls, ID 83415.

[c]*Idaho National Laboratory,*
2351 N. Boulevard, Idaho Falls, ID 83415.

Abstract

Graphite will be used as a structural and moderator material in next-generation nuclear reactors. While the overall nature of the production of nuclear graphite is well understood, the historic nuclear grades of graphite are no longer available. This paper reports the virgin microstructural characteristics of filler particles and macro-scale porosity in virgin nuclear graphite grades of interest to the Next Generation Nuclear Plant program. Optical microscopy was used to characterize filler particle size and shape as well as the arrangement of shrinkage cracks. Computer aided image analysis was applied to optical images to quantitatively determine the variation of pore structure, area, eccentricity, and orientation within and between grades. The overall porosity ranged between ~14% and 21%. A few large pores constitute the majority of the overall porosity. The distribution of pore area in all grades was roughly logarithmic in nature. The average pore was best fit by an ellipse with aspect ratio of ~2. An estimated 0.6–0.9% of observed porosity was attributed to shrinkage cracks in the filler particles. Finally, a preferred orientation of the porosity was observed in all grades.

4.1 Introduction

Graphite is an important component to the design of high-temperature gas-cooled reactors. Many of these reactors use graphite as a neutron moderator and/or structural component such as fuel- and gas-coolant channels [1–3]. Graphite is a desirable material because of its low neutron absorption cross-section and its high- temperature strength [4]. During operation, material properties and dimensions can change as a function of neutron irradiation dose and temperature. Gradients in both temperature and dose can lead to significant stress and distortion of the graphite components. Over time these stresses and distortions, if unaccounted for, can lead to failure of components, blockage of coolant channels, and even restriction of control rod sleeves [5].

The nuclear graphite is typically a nearly isotropic polycrystalline material with its microstructure primarily composed of coke filler and binder [6]. Most of the nuclear grades contain a petroleum or pitch-based coke. Materials such as graphite are quite unique in that variations in the coke type, quantity (relative to binder and later densification impregnations), forming process, and heat treatment processes can produce a relatively widespread distribution of initial properties and variation of graphite behavior under irradiation [2, 7, 8].

Irradiation-induced changes in graphite are strongly linked to the virgin microstructure of the graphite component [3, 9]. The filler and binder phases, pore and crack microstructure, as well as their relative quantities will significantly impact the dimensional change, mechanical and thermal properties, and oxidation of the graphite upon irradiation. Given the variability in graphite initial properties, and consequently irradiation behavior, it is important to establish a thorough understanding of the fundamental mechanisms involved in irradiation-induced changes to properties and dimensions [9–13]. This task is best accomplished through thorough characterization of virgin and irradiated nuclear graphites. This work focuses on virgin nuclear graphite characterization via optical imagery and digital image analysis.

While digital image processing and digital image analysis have been around since the 1960s [14], they have just recently become more common in the nuclear industry due to increases in commonly available computing power. Image analysis has been used to determine microstructural inputs for fracture models of polygranular graphite [15] and more recently to characterize porosity development under varying oxidation conditions [16]. Additionally, digital image analysis has been applied to 3D X-ray tomography techniques to map density evolution in oxidized samples [17–19]. In this work image analysis is used to estimate 2D parameters of the macro-porosity including area, perimeter, shape, and orientation in virgin nuclear graphite grades. 2D image analysis while somewhat restricted in terms of directly accessible parameters, compared to a 3D analysis, is much quicker and capable of examining much larger samples. This allows for a detailed statistical description of the features of interest, which will greatly benefit later irradiated and oxidized graphite characterizations.

4.2 Experimental

Nuclear graphite grades IG-110, PGX, NBG-18, and PCEA were selected for characterization. NBG-18 and PCEA were chosen because of the Next Generation Nuclear Plant (NGNP) program's interest for high irradiation dosage regions of the Very High Temperature Reactor (VHTR) [2, 3]. IG-110 is a fine grained historical reference grade which is currently being used in the HTTR and HTR-10 and is in many ways similar to IG-430, also a high dose candidate for the VHTR. PGX is a candidate grade for low dosage regions of the VHTR reactor. Pertinent data regarding these grades are presented in Table 4.1.

Table 4.1 Grain Size Comparison. Grain size refers to filler particle size.

Grade	Coke Source	Forming Process	Grain Size	Vendor
PGX	Petroleum	Molded	Medium	Graftech, USA
PCEA	Petroleum	Extruded	Medium	Graftech, USA
NBG-18	Pitch	Vibration Molded	Medium,1.6 mm[a]	SGL, Germany
IG-110	Petroleum	Isostatic Pressed	Superfine, 20 μm[b]	Toyo Tanso, Japan

[a] Maximum diameter of filler particles.

[b] Average particle length.

4.2.1 Sample Preparation

Samples prepared for optical microscopy and pore analysis were approximately 0.2 cm thick and had an observable surface of approximately 2.25 cm^2. To strengthen the graphite samples internally and prevent degradation of graphite pore walls and surface flow during polishing, samples were impregnated with epoxy resin and allowed to cure for 24 h. The graphite samples were hand-polished with successively finer SiC abrasive paper to a final grit of 1200. Next, samples were placed without additional weight into a vibratory polisher and allowed to polish for 3 h in a 0.3 μm SiC water-based suspension. Upon completion, samples were cleaned with deionized water to remove remaining SiC abrasive.

4.2.2 Optical Microscopy and Image Analysis

Optical microscopy was carried out using a standard bench-top Olympus BX51 Optical Microscope. Programming and code execution for pore identification and analysis were carried out using MATLAB® (MathWorks, USA) and its image processing toolbox. The bright field micrographs used for pore analysis were taken at a magnification of 5x. The pixel resolution of micrographs used for pore analysis was ~0.7 μm. The smallest pores identified were in the range of 5 μm^2; however, sample artifacts of similar sizes were also observed. To distinguish between porosity and sample artifacts of small sizes, higher magnifications were needed; therefore, the minimum pore size measured in this work was arbitrarily set to 12.5 μm^2. It was not necessary to use higher magnification in the case of such pores. Original micrographs were formatted as 24-bit color files as shown in Figure 4.1a for PGX graphite.

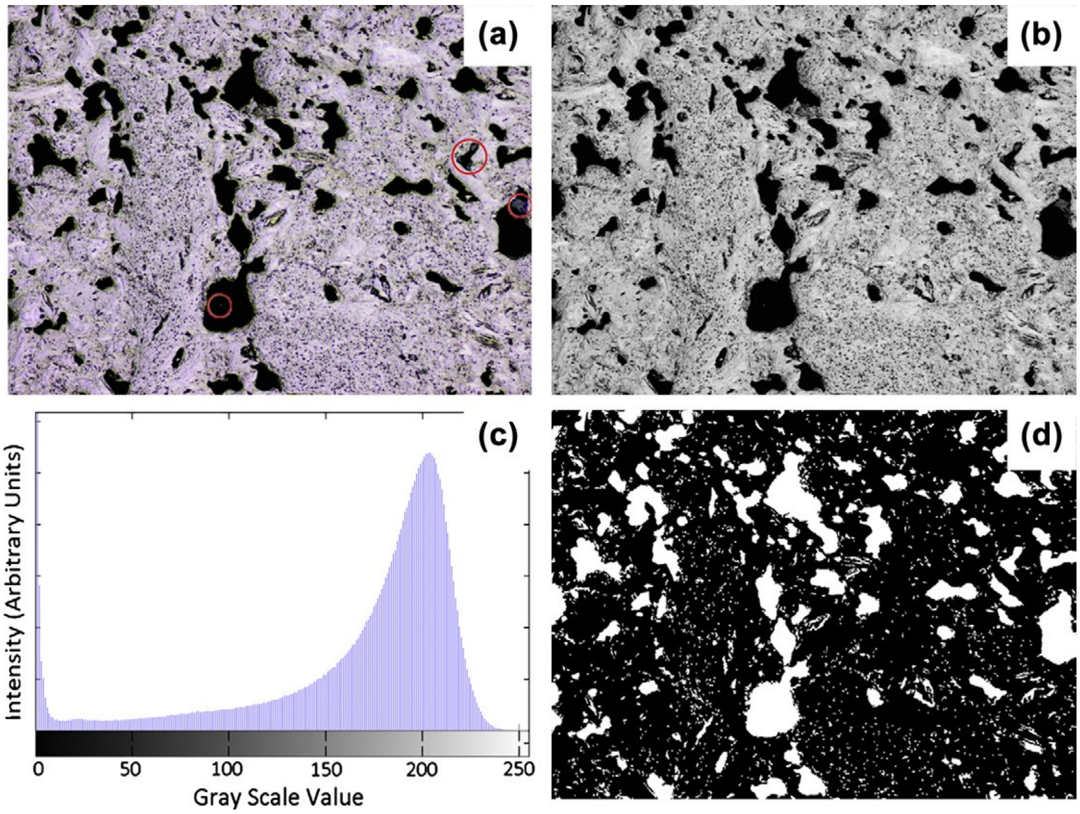

Figure 4.1 Basic image processing flow: (a) original colored micrograph, (b) gray-scale micrograph of (a) hue and saturation removed, but luminance retained, (c) histogram of (b) prior to contrast stretching and thresholding, (d) final binary image, this image is ran through connective components algorithm to extract quantitative pore data.

Upon uploading files to MATLAB they were converted to 8-bit gray-scale images. The color to gray-scale transformation was accomplished by eliminating the hue and saturation information while retaining the luminance of the color image (Fig 4.1b). Figure 4.1c shows a histogram of the gray-scale image in Figure 4.1b, in which two distinct peaks can be seen near 0 and 220 corresponding to the porosity and graphitic material respectively. Each graphite grade produced a nearly identical histogram. Contrast stretching was applied to all gray-scale images. The reference points for contrast stretching were approximately 50 and 220 respectively. The lower reference of

~50 was chosen because it corresponded well with local minima, yet it was still well within the range of what could sensibly be determined as porosity. The upper reference was chosen to correspond with the peak intensity of the polished graphitic material. Contrast stretching was performed to increase the sensitivity of the threshold parameter used for converting the images to the binary image matrices (Figure 4.1d). Typical values for the threshold parameter (allowable values are normalized between 0 and 1 over the 8 bit range of 0–255) were 0.45 for PGX, NBG-18, and PCEA and 0.37 for IG-110.

Two additional processing steps were used between converting to a binary image and data collection. The first was removal of small pores of area less than 25 μm^2 using morphological opening. Next was the removal of small ‘‘islands’’ such as those circled in Figure 4.1a. This step involved the use of a morphological flooding algorithm. These ‘‘islands’’ were removed under the assumption that they were (1) loose graphite fragments that become lodged in pores, or (2) artifacts of the 3D nature of the pores which were not directly in the polished plane of the sample.

To identify each pore and its respective pixels from the binary matrix, a connective components algorithm was applied with neighboring pixels defined as N4(p), the left, right, top, and bottom neighbor pixels [15]. Additional algorithms were used to extract the number of pixels (pixel area), the centroid coordinates within the matrix, perimeter, and orientation of each pore. Ellipses were used to provide a quantitative estimate of pore shape. The ellipse with the same normalized second central moment as the pore was used. The eccentricity (e), major axis length (M), minor axis length (m), and orientation of the major axis with respect to the horizontal image plane was extracted for each pore. The eccentricity of an ellipse is related to the major (M) and minor (m) axis length as,

$$e = \frac{\sqrt{M^2 - m^2}}{M} \ . \tag{4.1}$$

As such, eccentricity is defined between the degenerate cases of 0 and 1, where 0 is a circle and 1 is a line.

4.3 Results and Discussion

4.3.1 Filler Particle Size Analyses

The nature of the coke is integral to the development of the filler microstructure in nuclear graphite. As seen in Figs. 4.2–4.5, the shape of the filler particles varies from acicular to spherical. The shape of filler particles, in general, is a function of the coke's innate ability to align its rudimentary graphitic crystallites during calcination. Graphite with a petroleum-based coke tends to have anisotropic, acicular particles resulting from a high degree of alignment of rudimentary crystallites. On the other hand, pitch cokes are, in general, more isotropic and spherical in nature as a result of their lesser degree of rudimentary crystallite alignment. A summary of the size and shape of the filler material for each grade is given in Table 4.2.

Table 4.2 Measurements of Observed Filler Material. Major axis length (MAL), standard deviation (σ), aspect ratio (AR).

Grade	Sample Size	Mal Mean*	Mal σ	AR Mean*	AR σ
PGX	624	92±7 µm	85 µm	3.1±0.1	1.6
PCEA	320	126±10 µm	94 µm	2.6±0.2	1.6
NBG-18	300	360±25 µm	217 µm	~1	-
IG-110	625	27±2 µm	22 µm	3.9±0.2	2.4

* means are two sided confidence intervals, $\alpha = 0.05$.

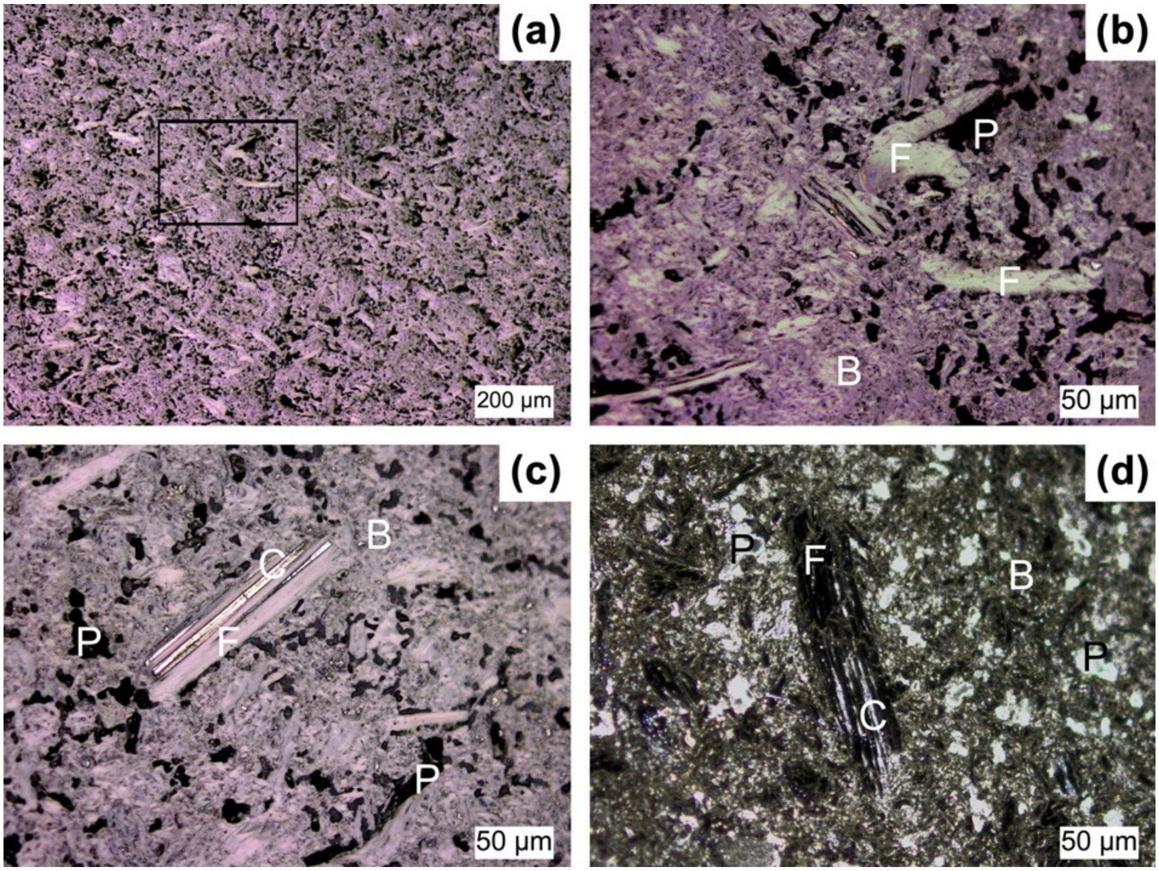

Figure 4.2 Optical micrographs of IG-110 graphtie: (a0 typical bright field micrograph of IG-110 showing filler, binder, and porosity, (b) bright field micrograph showing magnified view of the highlighted region in (a), (c) bright field micrograph of filler where the bright regions running along the length of filler particles are shallow shrinkage cracks and (d) dark field micrograph. P-Porosity, F-Filler, B-Binder, C-Shrinkage crack.

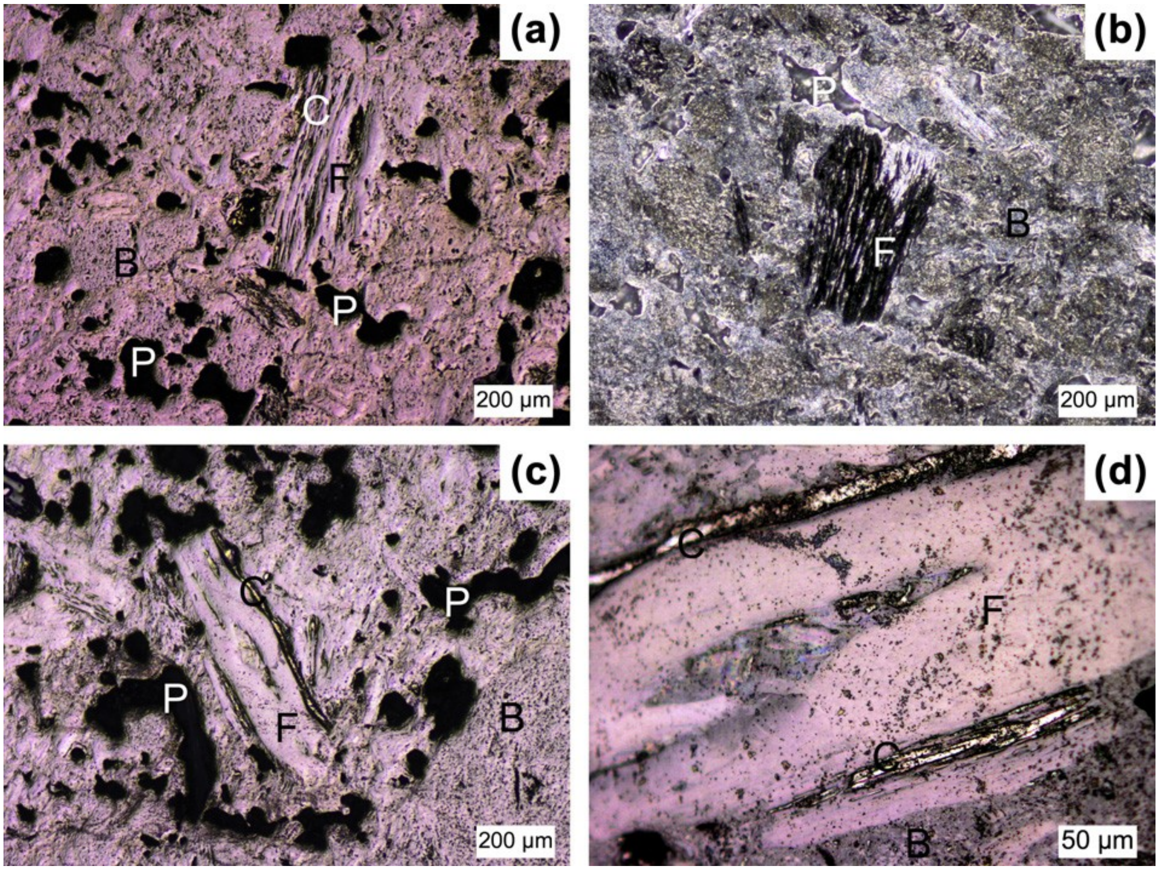

Figure 4.3 Optical micrographs of PGX graphite: (a) typical bright field micrograph of PGX showing filler, binder, and porosity, (b) dark field micrograph of filler in binder matrix, (c) bright field micrograph of filler with long shrinkage cracks running parallel to particle's long axis, and (d) bright field micrograph magnifying (c) P-Porosity, F-Filler, B-Binder, C-Shrinkage crack.

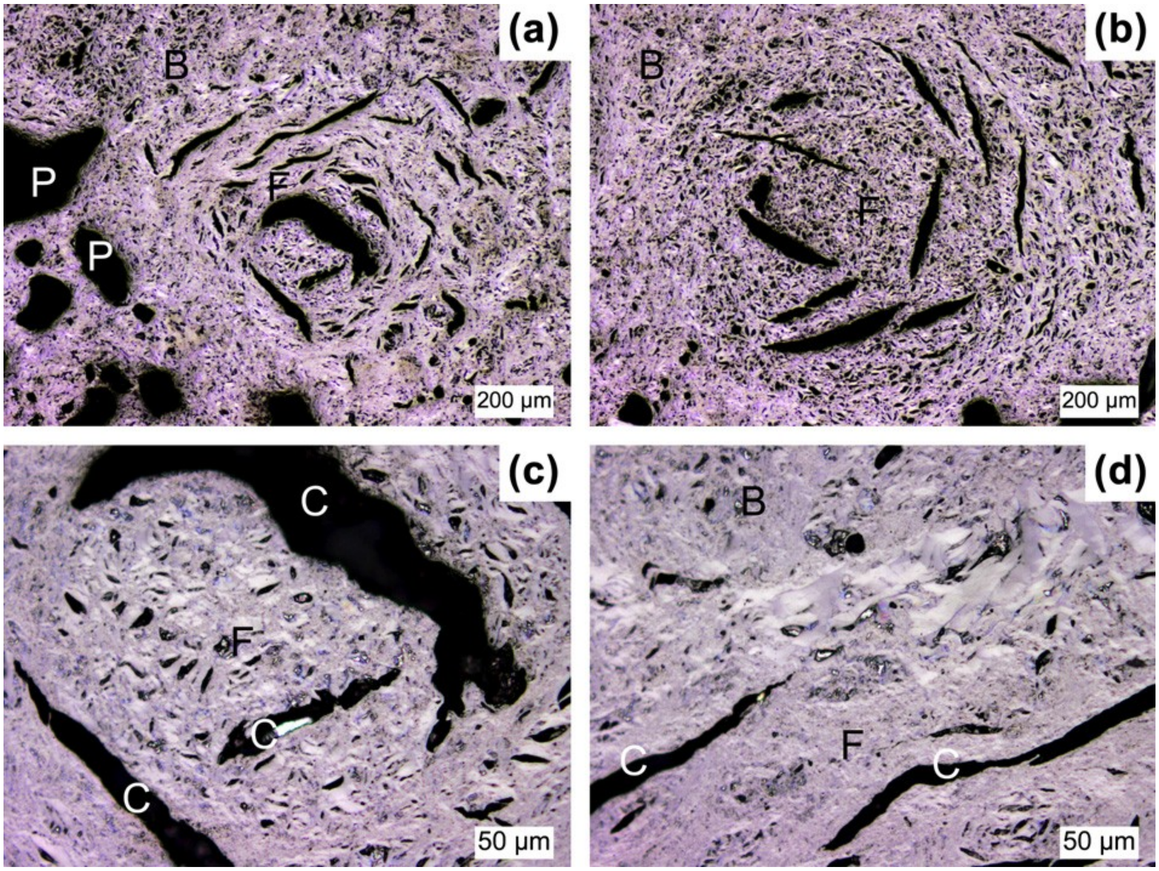

Figure 4.4 Optical micrographs of NBG-18 graphite: (a) bright field micrograph showing filler particles, binder, and porosity, (b) bright field micrograph of filler surrounded by binder matrix, (c) bright filed micrograph magnifying the inner region of filler particles in (a) , and (d) bright filed micrograph magnifying the outer perimeter of filler particle in (a). P-Porosity, F-Filler, B-Binder, C-Shrinkage crack.

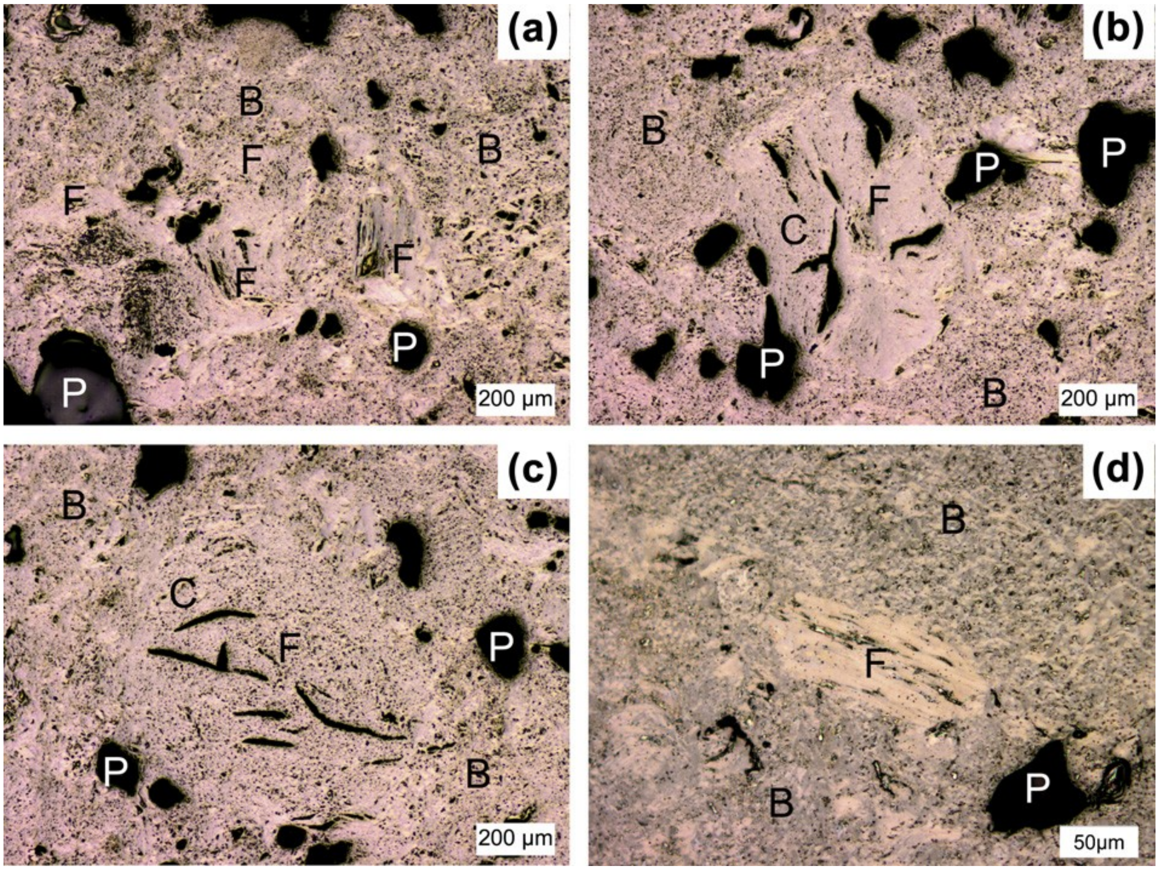

Figure 4.5 **Optical micrographs of PCEA graphite: (a) bright field image showing filler particles with various shapes, (b) bright filed micrograph of filler with relatively high degree of crystalline alignment surrounded by binder matrix, 9c) bright field micrograph of roughly spherical filler particles, and (d) bright field image of relatively small acicular filler particle. P-Porosity, F-Filler, B-Binder, C-Shrinkage crack.**

The filler observed in IG-110, a fine grained, petroleum based, nuclear graphite appears acicular (Figure 4.2). The mean length of filler observed was 27 ± 2 µm with a standard deviation (σ) of 22 µm.

This is reasonably similar to the average length given by the manufacturer of 20 µm. The mean aspect ratio observed for IG-110 filler is 3.9 ± 0.2, σ = 2.4. Observed in

Figure 4.2c are shrinkage cracks that run parallel to the major axis length of the particle. These cracks form during calcination as a result of the establishment of rudimentary basal planes of carbonaceous material. This strongly suggests that the c-direction of the graphitic crystallites is aligned with the minor axis of the particles.

The filler in PGX is also petroleum-based graphite. It is acicular much like IG-110 but, significantly larger in size (Figure 4.3). PGX filler particles are approximately three times larger than in IG-110 with a length of 92 ± 7 µm and $\sigma = 85$ µm. The aspect ratio of PGX filler was 3.1 ± 0.1 with $\sigma = 1.6$. Shrinkage cracks in PGX are more numerous and of greater thickness than those observed in IG-110.

The filler material in NBG-18, pitch-based graphite, appears to be spherical in nature (Figure 4.4). The mean particle size observed in NBG-18 is 360 ± 25 µm with $\sigma =$ 217 µm. The maximum particle size observed was 1796 µm which corresponds roughly with the manufacturer's stated maximum particle size of 1600 µm. The roughly 200 µm difference may in part be due to the difficultly in defining an exact particle boundary. The nearly spherical nature of the NBG-18 filler material suggests a relatively low degree of crystalline alignment within the particles. The crystallites in the center of the particles, in general, appear to be small and randomly oriented (Figure 4.4b). Those toward the particle exterior appear larger with their long axis aligned with the particle circumference.

The shrinkage cracks in NBG-18 vary greatly in size. Many of the larger shrinkage cracks, as observed in Fig 4.4a and b, are oriented with their long axis approximately tangential to the particle's radial direction. Further magnification of the filler particles in Figure 4.4a, c and d show the orientation of the small shrinkage cracks in the interior of the filler particle and near the perimeter respectively. The small shrinkage cracks toward the center of the filler particles appear to be randomly oriented, while those near the perimeter of the particle appear to be oriented similar to the larger shrinkage cracks.

PCEA, a petroleum-based graphite, had a wide variation in observed filler particles (Figure 4.5). Approximately 70% of filler is acicular in shape. The acicular particles had a mean length of 137 ± 12 µm with $\sigma = 88$ µm. The mean aspect ratio of the acicular particles is 3.2 ± 0.2 with $\sigma = 1.4$. The acicular particles in PCEA are slightly larger than those in PGX, but have a nearly identical aspect ratio. The spherical filler particles in PCEA had a mean diameter of 99 ± 21 µm with $\sigma = 102$ µm. PCEA filler material appears to have varying degrees of crystalline alignment. The spherical filler particle shown in Figure 4.5c appears to have crystalline alignment similar to that observed in the center of NBG-18 filler particles (Figure 4.4). These crystallites are relatively small and have a random orientation. The crystallites observed in Figure 4.5b appear to have a high degree of crystalline alignment similar to that observed in PGX particles (Figure 4.3). The shrinkage cracks observed in PCEA were relatively narrow compared to cracks observed in NBG-18. The orientation appeared random for small shrinkage cracks. Large shrinkage cracks appeared to have a preferred orientation along the particles long axis for acicular particles (Figure 4.5a and d). For spherical particles, the shrinkage cracks were aligned with one another, but not along any particular axis of the filler particle.

4.3.2 Pore Structure Analysis

The three different types of porosity within nuclear graphite are gas-evolved pores, shrinkage cracks, and microcracks [8, 20]. Pore characterization via image analysis used in the present study was able to resolve only gas evolved pores and shrinkage cracks. As observed in Figs. 4.2–4.5, the porosity varies greatly in size, shape, and orientation between and within grades. A statistical summary of the data collected is given in Table 4.3.

Table 4.3 Statistical Summary of Pore Analysis. Mean is arithmetic mean. W. mean is weighted mean based on each pore's fraction contribution to total porosity.

	Area (μm^2)					Eccentricity		Additional	
Grade	**Mean**	**W. Mean**	***σ***	**Min**	**Max**	**Mean**	***σ***	**Porosity**	**Count**
PGX	197.9	21,400	2047	12.1	353,336	0.820	0.14	21.49%	475,981
PCEA	146.8	30,100	2097	12.1	447,960	0.814	0.14	15.98%	1,242,597
NBG-18	168.3	23,600	1986	12.1	505,123	0.816	0.14	13.97%	916,076
IG-110	98	485	195	12.1	27,868	0.798	0.14	14.73%	1,532,451

Table 4.3 is the culmination of multiple samples of each grade covering areas of approximately 10 cm^2 for IG-110, NBG-18, and PCEA and an area of roughly 5 cm^2 for PGX. Such areas provided both large pore counts (on the order of 106) and were sufficient to observe variation within a grade. The arithmetic mean indicates that the distribution in pore size is skewed greatly toward the minimum pore size compared to a normal distribution. Examination of the weighted mean suggests that the majority of the total porosity is a result of a small number of large pores in PGX, PCEA, and NBG-18. In IG-110 the opposite appears to be true. The majority of the total porosity results from smaller pores as suggested by the weighted average. The mean eccentricity of the pores ranged from 0.798 for IG-110 to 0.82 for PGX, corresponding to aspect ratios of 1.66 and

1.75 respectively. A somewhat unexpected result was seen in the calculated porosities of the grades. NBG-18 was calculated to have an overall porosity of 14%, followed by IG-110 with 15%, PCEA with 16%, and PGX with 21% porosity. This result was unexpected given that visual inspection of IG-110 does not reveal significant porosity, while porosity is very apparent in NBG-18. The porosity was calculated by dividing the total pore area by the total area observed. For this calculation to be valid, the porosity must be nearly uniform throughout the graphite block. Using the theoretical densities of each graphite grade, apparent densities were back-calculated and compared to their respective values from the manufacturer (Table 4.4).

Table 4.4 Density Comparison. Summary of experimental and manufacturer apparent density values versus theoretical density calculated from lattice parameters.

Grade	Experimental	Manufacturer	Theoretical
PGX	1.77 g/cm^3	-	-
PCEA	1.90 g/cm^3	1.84 g/cm^3	2.257 g/cm^3
NBG-18	1.94 g/cm^3	1.85 g/cm^3	2.253 g/cm^3
IG-110	1.93 g/cm^3	1.77 g/cm^3	2.257 g/cm^3

The experimental apparent densities were all in excess of those listed by the manufacturer. For IG-110, NBG-18, and PCEA the errors, relative to the manufacturers' values, were 8.8%, 4.8%, and 3.1%, respectively. This positive error may occur as a result of an overestimation of pore area due to the choice of thresholding parameters. In a nuclear grade such as IG-110, size and proximity of the porosity can lead to connection of pores after thresholding. Such errors can be minimized, or at least remove experimenter bias to some degree, by investigation of automated global thresholding methods [15,21]. It is however, at least from visual inspection of optical micrographs, difficult to accept that manufacturer reported porosity of IG-110 is very similar to that predicted for PGX. Another possibility is the manufacturer's values were derived from fluid intrusion methods that were incapable of accessing all of the porous volume. This would result in an underestimation of the apparent densities. Regardless, this comparison is made to show the relative accuracy of measurements via digital image analysis.

Inspection of the resulting data for pore orientation showed an approximately normal distribution of orientation with respect to the horizontal image plane. To confirm the existence of a preferred orientation within the porosity, three mutually orthogonal samples were taken from each grade (IG-110, NBG-18, and PCEA). Resulting orientations were fitted to normal distributions and the standard deviation, σ, for each sample was tabulated. As seen in Table 4.5, NBG-18 and PCEA have only two statistically different standard deviations, implying a preferential orientation of porosity within the grades. IG-110 has three statistically significant means; however, two are relatively close to one another. This is assumed to be a result of imperfect slicing along the three orthogonal planes resulting in slight displacements of the standard deviations from their true values. While this (Table 4.5) indicates the existence of preferential pore orientation, it does not provide significant evidence as to the magnitude or variation of the orientation upon processing of the original block. To obtain such, detailed information about sampling location relative to the original block and the blocks orientation relative to processing would need to be known. It should be noted that there was no significant change in the distribution of pore area or shape with sample position or orientation. The orientation distribution observed in each cross-section does not appear to change as a function of pore area.

Table 4.5 Tabulated standard deviations for pore orientation distributions. Normal distribution assumed, confidence interval given for α = 0.05. Slight preferential orientation of major axis of pore observed. Sample population per face ranged from a minimum of ~87,000 to 327,000 pores.

Grade	Face 1	Face 2	Face 3
PCEA	52.4°±0.1°	49.2°±0.2°	48.9°±0.2°
NBG-18	49.8°±0.2°	49.7°±0.2°	47.8°±0.2°
IG-110	51.8°±0.1°	50.7°±0.1°	43.0°±0.1°

Since proprietary details of processing are only approximately known for each grade, it is difficult to conclude the exact reasoning for the observed pore orientation; however, it is suspected that the orientation is the result of densification impregnations. Gas evolved from the impregnation material will take the path of least resistance corresponding to the path through the impregnated pores to the nearest surface. If all three orthogonal faces are equally far from the point of gas evolution, there will be no preferred alignment of the porosity. When the point of gas evolution has different path lengths to the graphite block surface, preferred alignment will result. Using this hypothesis, the degree of preferred orientation will be dependent upon the position of the examined sample with respect to the original graphite block.

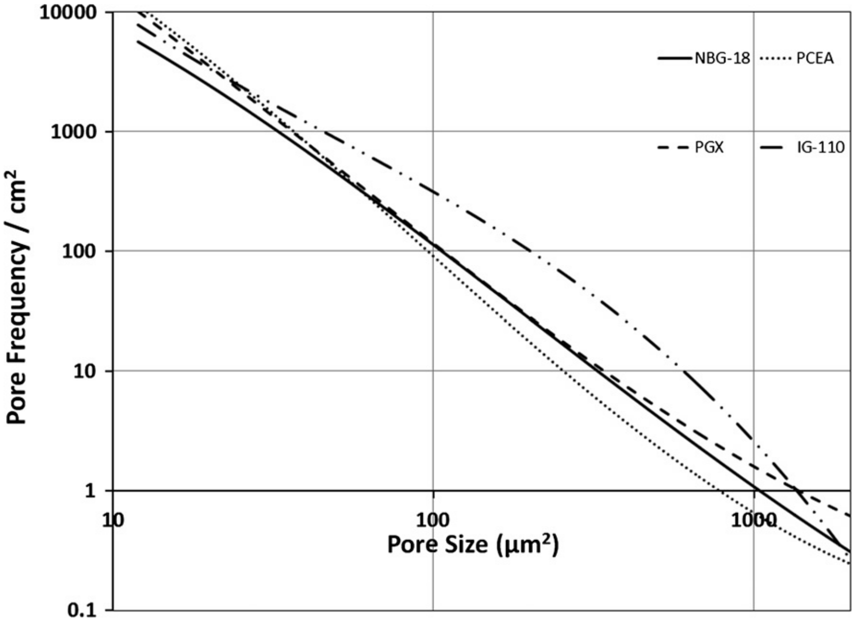

Figure 4.6 Log-log plot of frequency of pore size per cm^2 as a function of pore size.

While useful, the statistical data above does not fully describe the nature of the pores within each grade. The quantity of pores within any given size range was found to be a strong function of pore size. The shape of porosity, while not strongly dependent on pore size, had a wide distribution. In general, the aspect ratio of a pore ranged from 1 to 25. To better describe pore quantities and shape, continuous distributions were fitted to the experimental data collected. A plot of pore frequency/cm^2 vs. pore area ranging from 12 μm^2 to 2000 μm^2 is shown in Figure 4.6. Although significantly larger pores were observed in each grade, more than 98% of the pore data fell within this range. The ~2% remaining was discarded to allow a 'better' fit of the remaining data. Initial inspection of plotted data displays the approximate ''power-like'' nature of pore frequency vs. size. Transformation of the dependent and independent variables by a natural logarithm yield approximately linear functions (Figure 4.6). The pore area, while expressed in units of μm^2, was really measured as a discrete function of pixel quantities.

The final distributions were deemed best fit by a third-order polynomial with the natural log of the pore area as the independent variable (Table 4.6).

$$\ln\big(y(x)\big) = a + bln(x) + cln(x)^2 + dln(x)^3 \tag{4.2}$$

Table 4.6 **Porosity Size Distribution per Unit Area. The coefficients for distribution of each grade given by equation 4.2. X is pore area in μm^2. Y is frequency per cm^2.**

Grade	a	b	c	d
PGX	1.341E+01	-1.221E+00	-2.404E-01	2.111E-02
PCEA	1.205E+01	2.498E-02	-5.523E-01	4.160E-02
NBG-18	1.107E+01	-2.691E-01	-3.390E-01	2.138E-02
IG-110	1.543E+01	-3.795E+00	6.107E-01	-5.282E-02

Higher order polynomials provided higher R^2 values and lower root mean square errors; however, the rate of increase in 'fit improvement' dropped significantly with increasingly higher orders. The general logarithmic nature of the pore area distribution in PCEA appears to coincide well with similar image analysis techniques used by Contescu for PCEA [16].

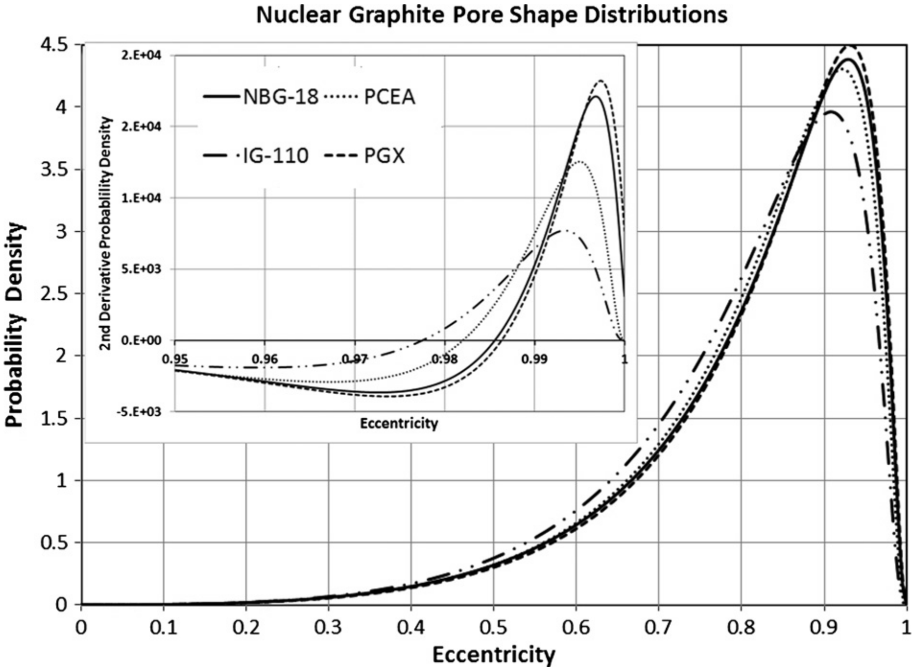

Figure 4.7 Continuous Probability Distribution of Porosity Shape Described by Eccentricity of an Ellipse. Inset plot is the 2nd derivative of the density function over the range of $e = 0.95$-1.

The shape of the porosity as described by the eccentricity of an ellipse is shown in Figure 4.7. By inspection, it is apparent that each grade has a relatively similar distribution, with the largest deviation occurring in the curve for IG-110. This deviation of IG-110 from the other grades is hypothesized to be the result of the green body formation via isostatic press. Figure 4.7 suggests that only a minority of the total pores may be described as approximately spherical (~6%) while nearly 75% of the pores examined have aspect ratios between 1.5 and 5. The average aspect ratio of porosity in nuclear graphite is approximately 1.7 and ranges from a low of 1.66 for IG-110 to a high of 1.75 for PGX. The shape of the experimental data curve for eccentricity was best fit by the Johnson SB continuous distribution function. The Johnson SB follows the general form,

$$f(x) = \frac{\delta}{b(1-b)}\phi(x) \tag{4.3}$$

where $z = \gamma + \delta \ln(b/1 - b)$, with $b = (x - \theta)/\sigma$, and ϕ is the standard normal distribution (Parameters in Table 4.7). For this function, γ and δ are shape parameters while θ and σ define the location and shape of the curve, respectively. The peaks of each function are located at eccentricities of 0.908, 0.931, 0.929, and 0.922 (aspect ratios of 2.389, 2.747, 2.704, and 2.579) corresponding to IG-110, PGX, NBG-18, and PCEA respectively. The probability of a pore existing with an eccentricity less than that of peak density is approximately 0.78 and ranges from 0.773 to 0.797.

Table 4.7 Parameters for Johnson S_B Fit of Pore Eccentricity for Each Grade.

Grade	γ	δ	θ	σ
PGX	-1.930	1.043	-5.931E-02	1.061
PCEA	-1.949	1.076	-8.090E-02	1.081
NBG-18	-1.884	1.039	-5.099E-02	1.052
IG-110	-1.863	1.106	-6.886E-02	1.069

Since two types of pores were observed, gas-evolved porosity and shrinkage cracks, with very different shapes, it was initially hypothesized that the pore shape distribution would be bimodal. As seen in Figure 4.7, this hypothesis is invalid. The shape distribution of porosity in nuclear grade graphite shows no obvious transition between shrinkage cracks and gas evolved porosity. To estimate the shrinkage crack contribution to total porosity the following assumption was made: The second inflection point in the continuous distributions is located at the eccentricity value where shrinkage cracks become the dominant observation. Using this criterion it was found that shrinkage cracks account for a fraction greater than or equal to ~0.9% of IG-110 pores, ~0.6% of PGX pores, ~0.6% of NBG-18 pores, and ~0.8% of PCEA pores. This appears to visually coincide with the optical micrographs of each grade. The average aspect ratio of the inflection point was approximately 5.5.

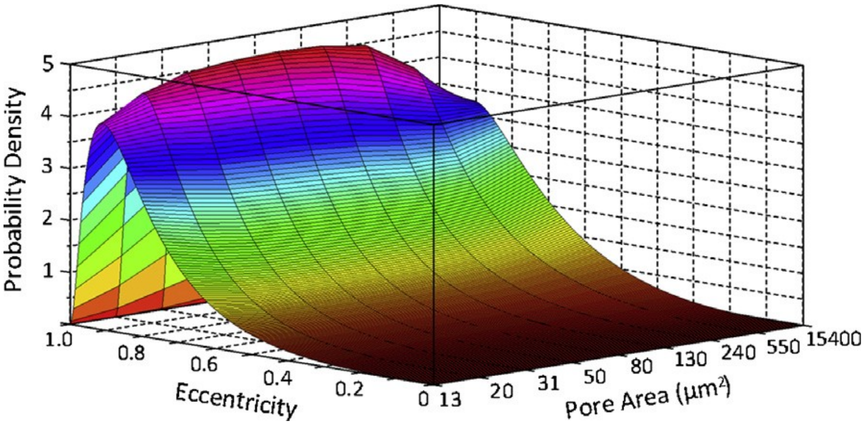

Figure 4.8 3D surface plot of the probability density of various pore shapes (eccentricity) for ranges of pore area; the pore area given is the log-mean average of the range of pore areas used.

From the examination of pore shape as a function of pore area, it was observed that the shape distribution function is slightly dependent on pore area. As the pore size increases, the probability density near the peak position increases and becomes a maximum near ~100 μm^2 for NBG-18 and PCEA (Figure 4.8). For IG-110 this peak occurs at approximately 300 μm^2. There is also a slight shift in the peak position to higher eccentricities that occurs in each grade. As the pore area is increased, this shift becomes much smaller. While there is a slight dependence of the shape distribution on pore area, the overall fit is exceptional over the entire range of pore area.

4.4 Conclusions

This paper characterizes the virgin microstructure of filler material and porosity in nuclear grade IG-110, PGX, NBG-18, and PCEA. As expected, the IG-110 and PGX grades had anisotropic filler particles of super fine and medium size, respectively. The newer, nearly isotropic grades NBG-18 and PCEA had filler particles more spherical in nature. The filler particles of these grades vary from super fine anisotropic particles in IG-110 to medium isotropic filler particles in NBG-18. The degree of crystalline alignment, which ultimately determines the particle shape, can be compared for each grade by inspection of the aspect ratio of the particles.

Image analysis of porosity in nuclear graphite appears to be an accurate method for quantitatively determining distributions and trends within the porosity. Apparent densities were measured accurately by image analysis. Preferential alignment was observed in each grade as a result of the examination of three orthogonal samples of each grade. The area of macro-scale porosity is roughly logarithmic in nature and can be fitted well with a third-order polynomial. The distribution of eccentricity in macro-scale porosity is fitted with the Johnson SB distribution.

While the size and shape of these 3D features may not be directly derived from measurements in 2D cross-sections, the measurements do provide a good qualitative basis for comparison with irradiated and oxidized graphite specimens.

4.5 Author Justification

The research presented in this publication was carried out and authored by Joshua Kane as a partial fulfillment of the requirements for a Doctoral degree in Materials Science and Engineering at Boise State University, under the advisement and supervision of Dr. Darryl P. Butt. Dr. Karthik Chinnathambi assisted with the optical microscopy of many samples examined as well as provided critical feedback and editing of the article in all stages of its preparation. Dr. Rick Ubic, Dr. William E. Windes, and Dr. Darryl P.

Butt contributed greatly in terms of financial support, detailed discussion distributions with respect to processing routes, and provided in-depth critical reviews of the article throughout the writing process.

4.6 References

[1] B. J. Marsden, L. H. Fok, Irradiation behavior and structural analysis of HTR/ VHTR graphite core components, in: 18th International Conference on Structural Mechanics in Reactor Technology (SMiRT 18), China, Beijing, August 7–12, 2005. SMiRT18-A01-7.

[2] R. Bratton and W. Windes, "NGNP graphite selection and acquisition strategy"; ORNL/TM-2007/153-10-07 (INL/MIS-10-19427), Oak Ridge National Laboratory, July 28, 2010.

[3] W. Windes, T. Burchell, and R. Bratton, Graphite technology development plan, INL/ EXT-07-13165, Idaho National Laboratory, September 2007.

[4] B. T. Kelly, "Physics of Graphite"; Academic Press, New York and London, (1962).

[5] B. T. Kelly, B. J. Marsden, and K. Hall, Irradiation Damage in Graphite due to Fast Neutrons in Fission and Fusion Systems, TECDOC-1154, International Atomic Energy Agency,Vienna, Austria, 2000.

[6] ASTM Standard D7219, 2008, Standard specification for isotropic and near- isotropic nuclear graphites, ASTM International, West Conshohocken, PA, 2003, doi:10.1520/D7219-08.

[7] W. P. Eatherly and E. L. Piper, "Manufacturing"; pp. 21-51 in *Nuclear Graphite*. Edited by R.E. Nightingale, Academic Press, 1962.

[8] R. E. Nightingale, "Structure"; pp. 87-115 in Nuclear Graphite. Edited by R.E. Nightingale. Academic Press, New York, 1962.

[9] R. Blackstone, "Radiation creep of graphite. An introduction," *J. Nucl. Mater.*, **65**, 72-78 (1977).

[10] B. T. Kelly and A. J. E. Foreman, "The theory of irradiation creep in reactor graphite- The dislocation pinning-unpinning model," *Carbon*, **12**[2] 151-159 (1974).

[11] B. T. Kelly, "Irradiation creep in graphite-some new considerations and observations," *Carbon*, **30**[3] 379-383 (1992).

[12] B. T. Kelly, "The analysis of irradiation creep experiments on nuclear reactor graphite," *Carbon*, **32**[1] 119-125 (1994).

[13] R. H. Telling and M. I. Heggie, "Radiation defects in graphite," *Phil. Mag.*, **87**[31] 4797-4846 (2007).

[14] R. C. Gonzalez and R. E. Woods, "Digital Image Processing"; third ed., Pearson Education Inc., New Jersey, 2008.

[15] T. D. Burchell, "A microstructurally based fraction model for polyranular graphites," *Carbon*, **34**[3] 297-316 (1996).

[16] C. I. Contescu and T. D. Burchell, Characterization of porosity development in oxidized graphite using automated image analysis techniques, ORNL/TM- 2009/192, 2009.

[17] L. Babout, P. M. Mummery, T. J. Marrow, A. Tzelepi, and P. J. Withers, "The effect of thermal oxidation on polycrystalline graphite studied by X-ray tomography," *Carbon*, **43**[4] 765-774 (2005).

[18] L. Babout, T. J. Marrow, P. M. Mummery, and P.J. Withers, “Mapping the evolution of density in 3D of thermally oxidized graphite for nuclear applications,” *Scr. Mater.*, **54**[5] 829-834 (2006).

[19] A. Hodgkins, T. J. Marrow, P. Mummery, B. Marsden, and A. Fok, “X-ray tomography observation of crack propagation in nuclear graphite,” *Mater. Sci. Technol.*, **22**, 1045-1051 (2006).

[20] K. Y. Wen, J. Marrow, and B. Marsden, “Microcracks in nuclear graphite and highly oriented pyrolytic graphite (HOPG),” *J. Nucl. Mater.*, **381**[1-2] 199-203 (2008).

[21] N. Otsu, “A threshold selection method from gray-level histograms,” *IEEE Syst. Man Cybern.*, **9**[1] 62-66 (1979).

CHAPTER FIVE: AN OXYGEN TRANSFER MODEL FOR HIGH PURITY GRAPHITE OXIDATION*

This chapter is published by Elsevier in *Carbon* and should be referenced appropriately.

Reference:

J.J. Kane, C. Karthik, R. Ubic, W.E. Windes, D.P. Butt, “An oxygen transfer model for high purity graphite oxidation,” *Carbon*, **59**, 49-64 (2013).

*This chapter includes modifications from the originally published version.

AN OXYGEN TRANSFER MODEL FOR HIGH PURITY GRAPHITE OXIDATION

Joshua J. Kane[a]

Chinnathambi Karthik[a]

Rick Ubic[a,b]

William E. Windes[b,c]

Darryl P. Butt[a,b]

Accepted for publication in:

Carbon

June, 2013

[a]*Department of Materials Science and Engineering, Boise State University,*
1910 University Drive, Boise, ID 83725.

[b]*Center for Advanced Energy Studies,*
995 University Boulevard, Idaho Falls, ID 83415.

[c]*Idaho National Laboratory,*
2351 N. Boulevard, Idaho Falls, ID 83415.

Abstract

An intrinsic mathematical model is developed for the investigation of the gas–solid reaction kinetics of high-purity graphite and oxygen. This model is based upon the oxygen transfer mechanism and uses physically meaningful parameters that are directly comparable to the experimental and theoretical literature of the carbon–oxygen reaction system. The model was used to extract reaction parameters for NBG-18 polycrystalline graphite for oxygen/nitrogen mixtures with a total pressure of 100 kPa. Experimental temperatures ranged from 500 to 850 °C for oxygen partial pressures of 1, 5, 10, 20, and 40 kPa. The optimized model parameters are in good agreement with previously reported literature values.

Nomenclature

C_{ac}	An armchair carbon edge atom on the {110}.
C_b	A basal plane carbon atom site.
$C_b(O)$	A "Stable" (temporarily stable) surface complex. The complex is an epoxide type structure that resides on the basal plane, (001).
C_e	A carbon edge atom site. C_{ac} and C_{zz} are subsets of C_e.
$C_e(O)$	A reactive surface complex assumed to be a semiquinone complex on an {100} or {110} type plane.
$C_e(O_2)$	A reactive surface complex assumed to be a dioxiranyl complex on an {100} or {110} type plane.

C_{zz}	A zigzag carbon edge atom on the $\{100\}$.

Coefficients, Constants, and Variables

a	The stoichiometric coefficient for carbon in the overall reaction $aC + O_2(g) \rightarrow Products(g)$
k_{A1}	The reaction rate constant for reaction (11a), $\left[\frac{m^3}{mol\ s}\right]$.
k_{A2}	The reaction rate constant for reaction (11b), $\left[\frac{m^3}{mol\ s}\right]$.
k_{D1}	The reaction rate constant for reaction (13a), $\left[\frac{m^2}{mol\ s}\right]$.
k_{D1}^*	The modified reaction rate constant for reaction (13a), $\left[\frac{1}{s}\right]$. $k_{D1}^* = k_{D1}[C_b(O)]$.
k_{D2}	The reaction rate constant for reaction (13b), $\left[\frac{m^2}{mol\ s}\right]$.
k_{D2}^*	The modified reaction rate constant for reaction (13b), $\left[\frac{1}{s}\right]$. $k_{D2}^* = k_{D2}[C_b(O)]$.
k_{D3}	The reaction rate constant for reaction (13c), $\left[\frac{1}{s}\right]$.
$k_{eff}^{''}$	The effective reaction rate constant for the shrinking cylindrical platelet model. The double prime denotes that the reaction is normalized with respect to platelet edge geometric surface area, $\left[\frac{m}{s}\right]$.
k_g	The gaseous mass transfer coefficient, $\left[\frac{m}{s}\right]$.

k_S	The reaction rate constant for reaction (12), $\left[\frac{m^2}{mol\ s}\right]$.
k_S^*	The modified reaction rate constant for reaction (12), $\left[\frac{1}{s}\right]$. $k_S^* = k_S[C_b]$.
l	The thickness of a graphite platelet particle, $[m]$.
n	The effective reaction order with respect to oxygen.
N_C	The molar flux of carbon, $\left[\frac{mol}{m^2\ s}\right]$.
n_C	The moles of carbon within a platelet, $[mol]$.
r	The radius of a platelet at time, t, $[m]$.
r_0	The radius of a platelet at time zero, t_0, $[m]$.
S_{ext}	The exterior geometric edge surface of a platelet, $[m^2]$.
t	Time, $[s]$.
α	Conversion. The quantity of reactant that has been converted to product, $\alpha = 1 - \frac{n_c(t)}{n_c(t_0)}$.
ρ	The carbon molar density. ρ was estimated using the lattice parameters for NBG-18, $\left[\frac{mol}{m^3}\right]$.
Γ_b	The surface concentration of carbon basal plane sites, $\left[\frac{mol}{m^2}\right]$.
Γ_e	The surface concentration of carbon edge sites, $\left[\frac{mol}{m^2}\right]$.

$[C_e(O)]$	The surface concentration of $C_e(O)$ surface complex, $\left[\frac{mol}{m^2}\right]$.
$[C_e(O_2)]$	The surface concentration of $C_e(O_2)$ surface complex, $\left[\frac{mol}{m^2}\right]$.
$[O_2]$	The gaseous oxygen concentration at the reacting surface, $\left[\frac{mol}{m^3}\right]$.

5.1 Introduction

Modern society would not be possible without the chemical combustion of carbon. According to the World Coal Institution, in 2009, 41% of the world's electricity production came from coal-fired power plants [1]. Thus the combustion of carbon is one of the most important and extensively investigated high-temperature reactions. As global energy demand continues to increase, there is an increased interest in low-carbon energy technologies to mitigate the effects of carbon emissions on climate change.

5.1.1 Nuclear Application

Nuclear power is one such low-carbon technology. Ironically, the combustion of carbon is still a very important chemical reaction; however, it is the mitigation of this reaction which concerns its use in nuclear applications.

NBG-18 graphite (SGL, Germany), the polycrystalline graphite of interest in this study, is a candidate graphite grade selected by the Next Generation Nuclear Plant program for use in the high neutron dosage region of the very high-temperature nuclear reactor (VHTR) pebble-bed design [2]. NBG-18 is nearly isotropic on the macroscale, has medium sized grains, and is produced from a coal-tar pitch coke source [3, 4]. The production is similar to that of many electrographites [5]. In addition, NBG-18 undergoes additional purification to meet ‘‘nuclear’’ graphite ASTM standards [4, 6]. A shortcoming to the use of carbon materials within a VHTR is their vulnerability to oxidation at operating temperatures (850–1000 °C) by either minor impurities in the helium coolant or accidental air ingress. Although these factors are not a critical concern for normal operation, they are of interest to maintaining and understanding the structural integrity of the graphite and throughout the reactor lifespan [7].

5.1.2 Oxidation Complications

The task of characterizing the kinetics and transport of a polycrystalline graphite may seem deceptively simple given the overall reaction; however, the characterization is complicated by the heterogeneous nature of the bulk material and the complex kinetics of the surface chemical reaction.

$$C(s) + \left(1 - \tfrac{1}{2}x\right)O_2(g) \rightarrow xCO(g) + (1 - x)CO_2(g) \qquad (5.1)$$

NBG-18 is essentially a carbon–carbon composite composed of filler particles (grains with well aligned graphite crystallites) held together by a graphitized binder material (Figure 5.1).

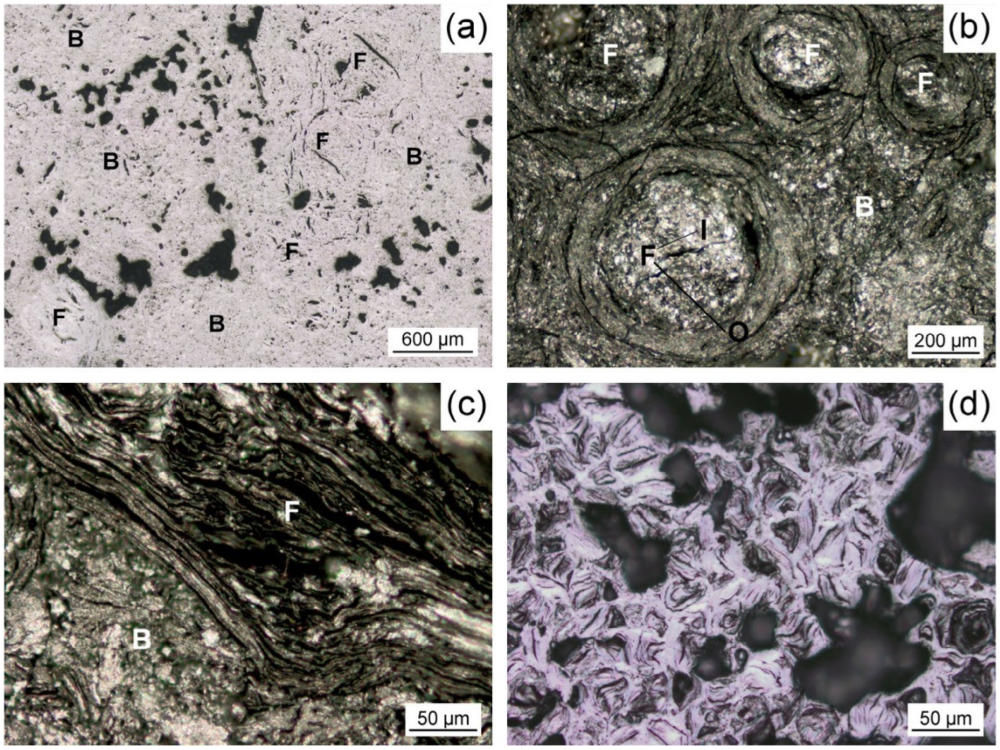

Figure 5.1 Various features of NBG-18 polycrystalline graphite are shown, including the filler, F, both inner, I, and outer, O, layers as well as the binder, B. (a) Shows the virgin NBG-18 microstructure. (b–d) Show oxidized NBG-18 filler. (b) Shows the inner and outer layers of the typically spherical filler particles. (c) Shows the high degree of alignment of crystallites in the outer layers of the filler particles relative to the binder. (d) Shows the random orientation of crystallites in the filler particle interiors. For (b and c), samples were oxidized for 30 min at 700 °C. For (d), graphite was oxidized using $K_2Cr_2O_7$ in concentrated sulfuric acid [8].

The production process creates a great deal of porosity and many shrinkage cracks from hydrolysis of the binder and initial calcination of the filler, respectively [9]. In addition, during rapid cooling from graphitization temperatures (> 2000 °C) the anisotropic thermal expansion leads to so-called microcracks [10 ,11] in the filler crystallites. These flaws span a large size range with the largest pores on the order of 1 mm in diameter and the smallest microcracks on the order of 1 nm in width. Such a large and heterogeneous porosity distribution complicates kinetics modeling of the porous graphite material. Many authors have attempted, with limited success, to model the effects of porosity on the chemical reaction of carbon materials with oxygen [12–15]. The complications are briefly discussed with the aid of Figure 5.2.

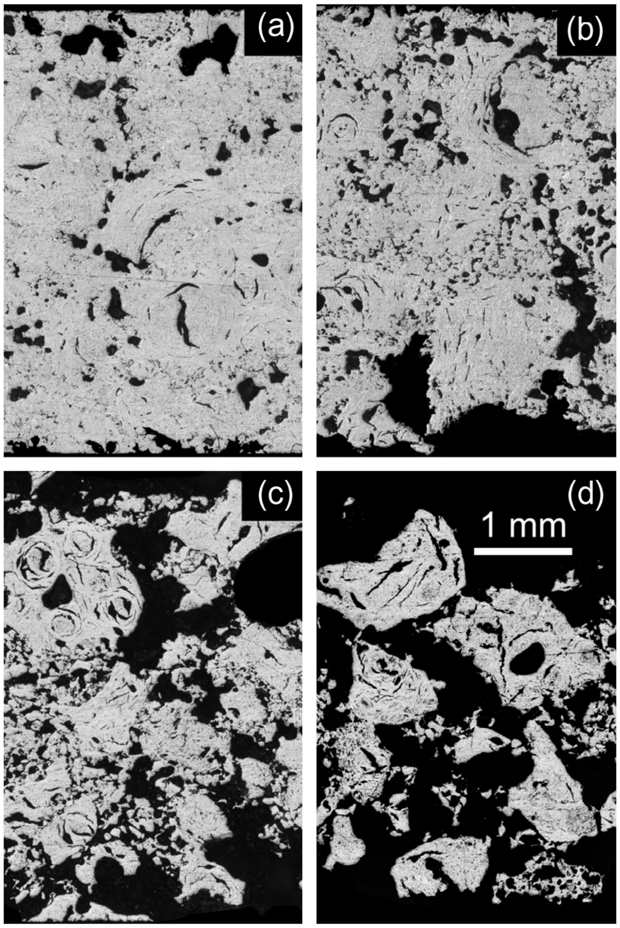

Figure 5.2 NBG-18 plate cross-sections showing progression of oxidation at 700 °C. Hours of oxidation: (a) 2 h (b) 4 h (c) 8 h (d) 12 h. Samples were run in a high-purity mixture of 21% O_2 balance N_2 (atomic basis) with flow rate of 500 sccm. All plate dimensions were approximately 4.5 x 13 x 51 mm. The scale bar in (d) applies to (a–c) as well.

When the rate of diffusion through the pore structure is of similar magnitude to the rate of oxidation, an oxygen gradient develops within the graphite porosity. Over time, the density of the bulk graphite will become non-uniform. Near the exterior surface transport of oxygen and/or reaction products will be convective but becomes increasingly diffusive in nature towards the interior as the void fraction decreases. The surface area significantly changes during the course of the reaction as well. Initially, the surface area increases as small pores are opened (Figure 5.2a and b). As the pores grow, their interconnectivity increases, causing the overall surface area to decrease.

The polycrystalline nature of NBG-18 can also obscure the analysis of the carbon–oxygen reaction kinetics. In Figure 5.1c and d, it is evident that the binder is preferentially oxidized relative to the filler material. The binder is composed of small randomly oriented crystallites whereas the crystallites in the filler particles are much larger and well aligned with their [0 0 1] typically parallel to the particle's radial direction. This preferential oxidation is due to the much larger quantity of exposed reacting surface area on the smaller randomly oriented crystallites. Preferential oxidation of the binder phase has also been observed by Contescu *et al.* [16]. Additionally, at the surface of the bulk material, high degrees of burn-off may cause filler particles to fall out of the binder.

A great deal of literature exists on oxidation of graphite materials for nuclear applications [17–25]. The literature shows a wide variation between grades, but more concerning is the large variation in measured parameters between experiments for the same grade. Much of this scatter can be attributed to the physical complications of phenomena discussed above, and thus leads to difficulty in the comparison of rate data for specimen of different sizes, geometries, and gas flows. This variation severely limits the degree of confidence that can be given to extrapolations of experimental reaction-rate data to the monolithic graphite material to be used within a future VHTR. The end goal of this research is the development of a general oxidation model applicable to all high-purity polycrystalline graphites. Such a model must be normalized to the reacting surface of a graphite rather than the mass, volume, or geometric surface area since these parameters are inherently linked to the microstructure and thus the carbon source and manufacturing process of the graphite.

5.1.3 Carbon-Oxygen Reaction Kinetics

The oxidation kinetics of carbon materials has received a great deal of consideration for over a century. Indeed, the carbon–oxygen reaction is arguably one of the most important known reaction systems. Despite a plethora of data and research efforts, the literature still contains a wide range of activation energies (~120 to ~400 kJ/mol for product desorption [26–28]) and no unifying rate equation that describes the rate of oxidation for all carbon materials. In a 1969 lecture, J.M. Thomas [29], likened the carbon oxidation kinetics literature to Ecclesiastes 1:18 ''For in much wisdom is much grief: and he that increaseth knowledge increaseth sorrow.'' Despite the lack of a unified rate equation many pioneers such as Thomas, Hennig, Walker, and Radovic have made significant contributions to the understanding of the carbon– oxygen reaction and the elementary processes within the reaction mechanism. Several excellent contributions to the literature exist that summarize key findings over the past half century and highlight current problems and developments within the field [26, 29–36].

There are three reaction products in the carbon–oxygen reaction system, gaseous CO, CO_2, and a temporarily stable carbon–oxygen surface complex, $C_b(O)$. CO and CO_2 were both confirmed to be primary reaction products by oxygen tracer experiments performed by Vastola *et al.* [37] and Hart [38]. The stable surface complex, $C_b(O)$, is an epoxide type structure on the surface of the basal plane. Although the complex is not directly desorbed as CO or CO_2, it can participate indirectly in the formation of CO_2, and it dynamically weakens adjacent C–C bonds within the basal planes, thus affecting local carbon reactivity [39–44]. A reaction mechanism for carbon oxidation containing all known influential factors is quite complicated [32, 45]. The essential reaction features are reflected in the following generalized oxygen transfer mechanism for carbon oxidation proposed by Radovic *et al.* [34–36]:

$C_{zz} + O_2(g) \rightarrow C_e(O_2)$	Molecular Oxygen Chemisorption	(5.2a)
$2C_{ac} + O_2(g) \rightarrow 2C_e(O)$	Oxygen Dissociative Chemisorption	(5.2b)
$C_e(O_2) + C_b \rightarrow C_e(O) + C_b(O)$	Oxygen Spillover	(5.3a)
$C_{b1}(O) \leftrightarrow C_{b2}(O)$	Surface Diffusion (hopping)	(5.3b)
$C_e(O) \rightarrow CO(g)\ (+2C_e)$	Direct CO Desorption	(5.4a)
$C_e(O) + C_b(O) \rightarrow CO_2(g)\ (+C_e)$	Indirect CO_2 Desorption	(5.4b)
$C_e(O_2) \rightarrow CO_2(g)\ (+2C_e)$	Direct CO_2 Desorption	(5.4c)
$2C_e \rightarrow 2C_b$	Nascent Site Deactivation	(5.5)

Reactions (2a) and (2b) represent the chemisorption of oxygen, either molecularly or dissociatively, onto the carbon surface. The strong covalent sp2 hybridized bonds within the carbon basal planes, (0 0 1), and weak delocalized p bonds between planes, result in the high affinity of oxygen to the unsaturated bonds of edge carbon atoms, (hk0). Thus oxygen chemisorption occurs only on the edge planes [46], specifically on activated sites such as the carbene-like C_{zz} and carbyne-like C_{ac} sites [47]. Due to differences in the local chemical environment, these sites have different reactivities. This has been shown experimentally through meticulous work by both Thomas and Hennig [48, 49], and confirmed by many density functional theory (DFT) simulations [36, 41]. Chemisorption of oxygen onto the basal plane molecularly or dissociatively does not occur as it is highly unfavorable thermodynamically [46, 50].

Given the anisotropy and preferential (re)active sites in graphite, different classifications of surface area must be defined. Total surface area (TSA) is the total surface area of the carbon material and is obtained via a method such as a Brunauer-Emmett-Teller (BET) method combined with a physisorption isotherm [51, 52]. The subsets active surface area (ASA) and reactive surface area (RSA) must also be considered. ASA and RSA can be defined succinctly as the portion of the TSA capable of chemisorbing oxygen and the portion of TSA covered by reactive surface intermediates, respectively [46, 53].

It has been known for quite some time that, at high surface coverage, the large concentration of chemisorbed O_2 (as much as 10–20 weight percent [31, 47, 54, 55]) cannot be explained by edge atoms alone. For these concentrations of oxygen to exist on a carbon surface, oxygen must be able to migrate to the basal plane. This fact is reflected in reaction (5.3a) in which molecularly chemisorbed oxygen spills over onto basal plane carbon sites [31, 44, 56]. Radovic *et al.* [50, 57] recently reported a viable pathway for the formation of an epoxide structure on the basal plane upon exposure to O_2. Orrego *et al.* [42] has proposed an alternative pathway that may become prominent at higher temperatures (>725 °C) as the equilibrium concentration of atomic oxygen becomes appreciable.

The stable surface complex, $C_b(O)$, migrates along the basal plane by hopping between bridge sites. The surface complex, initially straddled between carbon sites, breaks a carbon–oxygen bond and passes through a transition state above a single carbon atom before reforming a carbon–oxygen bond. Radovic *et al.* [57] estimated the diffusivity at 650 °C to be on the order of 10-11 m^2/s with an activation energy of approximately 70 kJ/mol for grapheme. Yang and Wong [56] experimentally measured the diffusion rate of $C_b(O)$ at 650 °C and found a diffusion coefficient orders of magnitude smaller and an activation energy of nearly 150 kJ/mol. This large variation can be attributed to the extreme sensitivity of the $C_b(O)$ to the geometric and electronic properties of the local basal plane [57]. The addition of edge functional groups such as semiquinones will drastically reduce the energy barrier for diffusion of $C_b(O)$ toward the center of the basal plane. While the oxygen mobility is not as high as in related oxygen/metal systems, it is quite significant and thus an important factor in the carbon–oxygen reaction system [58].

Since it is well known that dissociative chemisorption is an important process in the surface chemical reaction, desorption pathways such as reactions (5.4a) and (5.4b) are quite reasonably expected [31, 32]. CO(g) is formed by the direct decomposition of $C_e(O)$ complex. It is also known that the stable surface complex lowers carbon–carbon binding energies by approximately 30%, thus $C_b(O)$ should play a role in the rate of reaction (5.4a) indirectly [40]. In reaction (5.4b), CO_2 (g) is formed by the insertion of oxygen (unzipping) from the basal plane epoxide adjacent to $C_e(O)$ followed by subsequent desorption [34, 42]. Carbon dioxide can also be formed via a direct pathway. A modulated molecular beam study performed by Olander *et al.* [59] suggested that a majority (80– 90%) of CO_2 evolved was produced by ‘‘direct encounters’’ of molecular oxygen with the edge surfaces at 1177 °C. This stemmed from the observation of incomplete statistical mixing of the oxygen isotopes used. Thus reaction (5.4c) must be taken into consideration as a significant contributing source for CO_2 production [34, 43].

A broad range of activation energies for desorption have been observed in the literature due in part to the local chemical environments of different (re)active sites, but also a variety of functional group [28, 60–63] seen especially in chars. Arguably, the most important functional groups for graphite are the semiquinone and dioxiranyl surface complexes, for the $C_e(O)$ and $C_e(O_2)$ reactive surface complexes, respectively. The range of activation energies is known to be much greater for chars than highly graphitic materials, which may be a result of the surface heterogeneity of chars, especially the lack of resonance in some of the char structures. Resonance energy may account for approximately 40–60 kJ/mol difference in the stability of an active site [41].

Finally, the stabilization of (re)active sites and hence the reduction of site (re)activity is represented by reaction (5.5). This phenomenon has been dubbed nascent site deactivation (NSD) and was used by Ranish and Walker [64] to describe the pressure effects observed at high oxygen partial pressures and low temperatures on the rate of carbon gasification. The NSD of the carbyne-like armchair and carbene-like zigzag active sites are quite different and are discussed in detail by Radovic *et al*. [35]. NSD also suggests that the number of (re)active sites available under steady-state conditions is dependent upon the rate of site deactivation relative to the rate of oxidation as well as the equilibrium reactive surface complex concentration [35, 65, 66].

5.2 Experimental

As discussed in Section 5.1.2, porosity in a carbon material greatly complicates the oxidation kinetics of the bulk material. Near 700 °C (Figure 5.2), the oxidation of the bulk graphite in this study is well within the regime of pore diffusion [30]. While the temperature range of the kinetic regime can theoretically be expanded by a substantial increase in the gas velocity over the graphite surface, filler particle fall out, and changing surface area throughout the reaction are difficult to account for directly.

5.2.1 Graphite Powder

To avoid the convoluting effects of porosity on the reaction kinetics and develop an intrinsic reaction model, graphite powder was used. NBG-18 graphite powder was prepared from bulk NBG-18 using a percussion mortar and pestle. A particle density of 2.23 g/cm^3 (99% theoretical density) was measured using a helium pycnometer (Quantachrome, USA) upon passage through a 500 mesh (25 µm) sieve. The particle size distribution was measured using a laser diffraction particle size analyzer (Partica LA-950, Horiba, Japan) via a wet method in distilled water. The particle size was normally distributed with a mean of 12.9 µm and a standard deviation of 4.6 µm. This was confirmed by inspection using an analytical scanning electron microscope (Hitachi S-3400N-II, Hitachi, Japan).

The reactivity of carbon is known to vary with the level of impurities [30, 32, 67, 68]. The NBG-18 graphite used in this study did not undergo the additional purifications required for nuclear applications [4]. The results of elemental analysis via inductively coupled plasma mass spectrometry (ICP-MS) are shown in Table 5.1. Impurity levels were assumed negligible in terms of their participation in the overall observed rate of oxidation.

Table 5.1 Twelve Largest Impurities in NBG-18. Elemental analysis performed via ICP-MS. The quantities are given in terms of mass fraction.

Element	ppm	Element	ppm	Element	ppm
Si	38	**Fe**	4.8	**Hg**	< 0.5
Ca	5.9	**F**	< 1	**Mg**	< 0.5
Ta	< 5	**B**	0.57	**Pb**	< 0.5
S	4.8	**Cr**	< 0.5	**Sb**	< 0.5

5.2.1 Powder Oxidation Experimental Setup

The overall rate of carbon consumption

$$aC(s) + O_2(g) \rightarrow Products(g) \tag{5.6}$$

For NBG-18 was measured via thermogravimetric analysis (STA 449 F3 Jupiter, Netzsch, Germany). Experiments were performed isothermally between 500 and 850 °C. The absolute pressure within the reaction chamber was constant at approximately 100 kPa. The gas flow rate was maintained at 270 standard cubic centimeters per minute (sccm) to decrease the likelihood of mass transfer playing a significant role in the observed kinetics. The inlet gas was composed of 7.4 mol% argon, a protective gas for the balance chamber of the analyzer, and varying amounts of oxygen and nitrogen. Five oxygen partial pressures were investigated 1, 5, 10, 20, and 40 kPa.

All experiments were conducted with 15 ± 0.5 mg of well- mixed NBG-18 powder placed in an alumina crucible (6 mm diameter, 4 mm high). Alumina was shown by Ranish [69] to be an inert material in the carbon–oxygen reaction system. Prior to running an experiment, the graphite samples underwent a vacuum and purge cycle to remove adsorbed moisture. Immediately thereafter, samples were ramped to the reaction temperature at a rate of 20 °C/min in nitrogen at 50 sccm. Upon reaching the reaction temperature, the system was allowed to stabilize thermally for 30 min in nitrogen. The nitrogen flow was increased in two 100 sccm steps to 250 sccm over the first 5 min of the thermal stabilization dwell. After the allotted 30 min, the gas mixture was switched to the desired oxygen/nitrogen mixture with a total flow rate of 250 sccm. Each set of experiments was duplicated at least once for greater statistical certainty. A correction file was run at each temperature and partial pressure to account for errors in gravimetric measurements due to changing gas flows and thermal drift over longer experiments (>36 h). Residual powder was collected for post-examination. The excess oxygen ratio, EOR, was used as a figure of merit to help ensure that transport effects did not interfere with kinetics measurements. The EOR was calculated as the difference between oxygen molar flow rate and rate of carbon consumption, relative to the rate of carbon consumption, assuming the reaction product was entirely CO_2. Once the EOR fell below 10 for any significant portion of the experiment, higher temperature experiments were assumed null.

All gases were obtained from Praxair Inc. (CT, USA). The argon and nitrogen gases used were ultra-high purity grade. Oxygen was introduced via one of two primary standards containing 5% and 40% oxygen (by volume), respectively and the balance nitrogen. Analytical uncertainty for the standard was guaranteed to be within ±2% of the reported oxygen concentration.

5.2.2 Electron Microscopy

NBG-18 powder was examined pre- and post-oxidation using a scanning electron microscope (SEM) (S-3400N-II Analytical SEM, Hitachi, USA).

Transmission electron microscope (TEM) samples were analyzed to confirm assumptions made in the derivation of the shrinking-core model. The analysis confirmed preferential oxidation orthogonal to the basal plane and the absence of significant amounts of product film/ash on the graphite surface. TEM samples of NBG-18 (bulk material purchased from SGL group, Germany), were prepared by cutting thin bars, approximately 3 mm in length, from the as-received graphite. These bars were further thinned mechanically to a thickness of approximately 100 µm. An ion-slicer (EM09100-IS, JEOL, Japan) was used to achieve the final electron transparency. Compared to conventional ion milling techniques, the ion-slicer produces minimal beam damage to the TEM samples. After initial examination in the TEM, samples were oxidized for 5 min with an oxygen partial pressure of 20 kPa at 600, 700, or 800 °C and re-examined. Examination took place at room temperature using a high resolution transmission electron microscope (2100-HR, JEOL, Japan) operated at 200 kV.

5.2.3 Arrhenius Parameter Estimation

The Arrhenius parameters for the oxygen transfer model (see Section 5.3.3.1) were determined using an unconstrained non- linear optimization implemented in MATLAB® (Matlab R2011a, Mathworks, USA). The optimization used a Nelder-Mead simplex direct search algorithm [70]. The minimization function was chosen specifically to mitigate substantial numerical error due to the large magnitudes and variation in parameter values with temperature and oxygen concentration. An initial guess vector for the optimization was chosen using a combination of available literature values, estimates from linear sections of the experimental Arrhenius plot, and visual inspection.

5.3 Results/Discussion

5.3.1 Shrinking Cylindrical Platelet Model

Derivation of the phenomenological shrinking cylindrical platelet model (SCPM) follows the approach of Levenspiel for a shrinking core [71, 72]. In order to make inferences regarding the surface chemical reaction, the oxygen concentration at the surface must be known. If the reaction resistance is much greater than the gaseous mass transfer $\frac{1}{k''_{eff}} \gg \frac{1}{k_g}$ and there is no/negligible ash or reaction product on the solid surface (a reasonable assumption for high purity graphite) the concentration at the carbon surface is essentially that of the bulk gas stream.

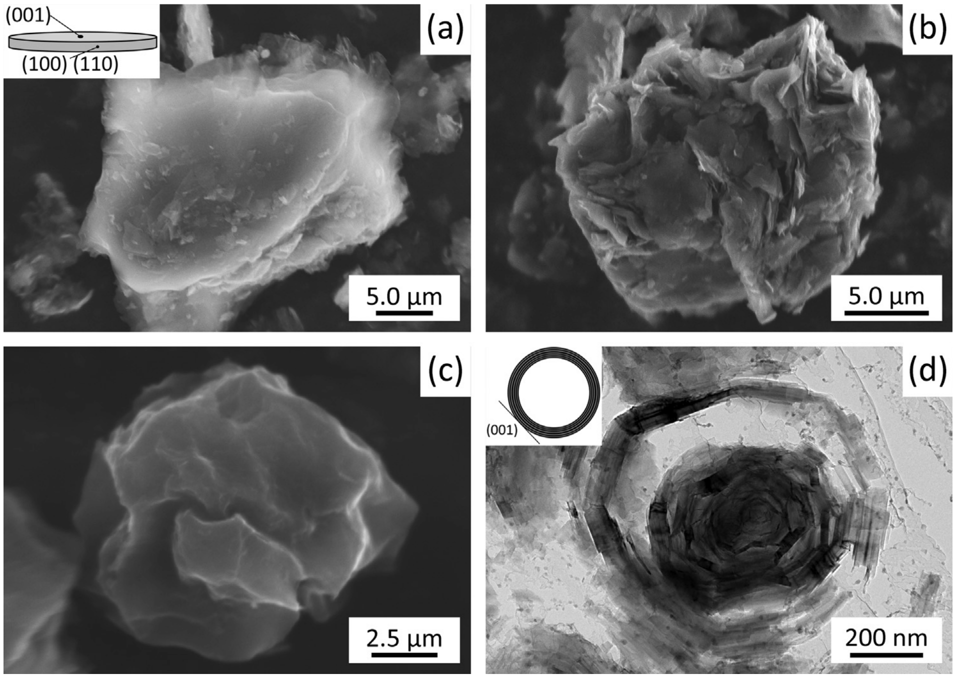

Figure 5.3 Scanning electron micrographs of powder showing (a) a graphite platelet oriented as depicted in the inset, (b) a graphite platelet oriented on edge, (c) a platelet oxidized at 575 °C to $\alpha \approx 0.5$ at $P_{O2} = 20$ kPa, and a transmission electron micrograph of oxidized NBG-18 binder showing (d) quinoline insoluble particle oxidized at 700 °C for 5 min at $P_{O2} = 20$ kPa.

In addition, for a traditional shrinking cylindrical core it is assumed that it was assumed that the chemical reaction did not occur on the top or bottom of the graphite platelets (graphitic basal planes), but only along the plate edges ((1 0 0) and (1 1 0) planes, Figure 5.3a–c). In other words, it is assumed that the RSA is proportional to the plate edge area, 2πrl. A transmission electron micrograph of an oxidized, quinoline-insoluble particle is shown in Figure 5.3d. These particles, as depicted in the inset, are structured with the basal plane orthogonal to the particle's radial direction. The preservation of much of the particle along [uv0] visually suggests oxidation parallel to the (001) planes, as previously observed [46].

The molar flux of carbon from the RSA of the graphite may be expressed as

$$-N_C = ak_{eff}^{''}\left[O_2\right]^n \tag{5.7}$$

however,

$$N_C = \frac{1}{S_{ext}}\frac{dn_c}{dt} \tag{5.8}$$

The double prime above the reaction rate constant is used to denote that it is normalized with respect to the platelet edge geometric surface area which is assumed proportional to the RSA. Relating the moles of graphite to the cylindrical radius of the platelet through the molar volume, upon integration Eqs. (5.7) and (5.8) become

$$1-\frac{r}{r_0} = \frac{ak_{eff}^{''}\left[O_2\right]^n}{r_0\rho}t \tag{5.9}$$

Typically, the term $\frac{r}{r_0}$ is replaced by an expression for the conversion of material to product defined here as α. For cylindrical platelet geometry the conversion is related to $\frac{r}{r_0}$ by

$$\frac{r}{r_0} = (1-\alpha)^{1/2} \qquad (5.10)$$

A plot of $1 - (1 - \alpha)^{1/2}$ vs. time will yield a straight line if the SCPM describes the physical progression of the reaction. The slope of such a plot contains information regarding the effective reaction order and the effective reaction rate constant. Both the reaction order and rate constant are generally expressed as effective parameters since gas–solid reactions typically involve many elementary steps within the overall reaction.

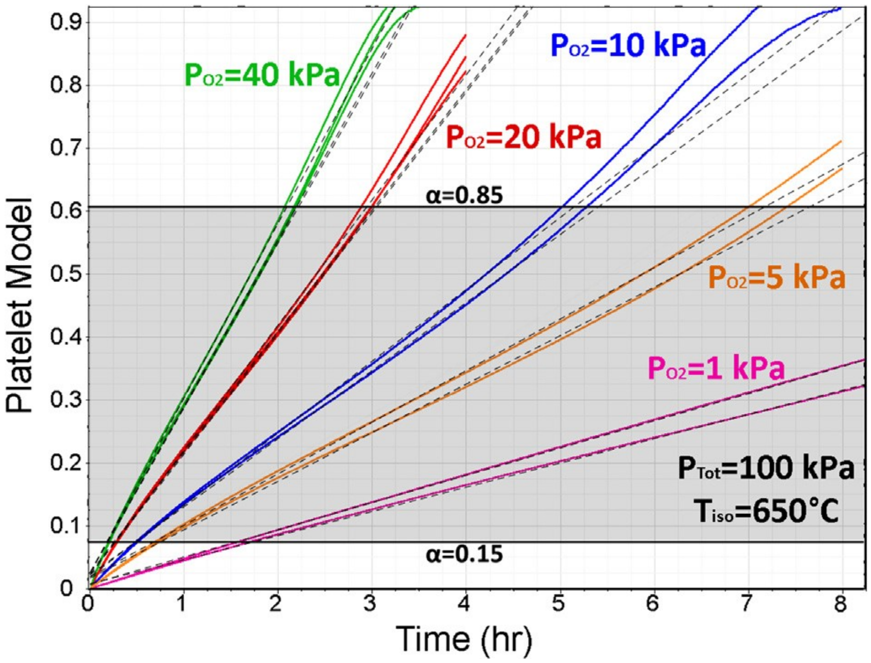

Figure 5.4 The experimental measurements at 650 °C for 1, 5, 10, 20, and 40 kPa O_2 in N_2 of $1 - (1 - \alpha)^{1/2}$ vs. time. The error from individual data points and linear fits are insignificant relative to the error between measurements.

Throughout the entire experimental range, the SCPM was found to provide a reasonable fit of the experimental mass-loss data for all oxygen partial pressures. As observed in Figure 5.4, the trend is highly linear, having a correlation coefficient greater than 99% for all experimental oxygen partial pressures. The slope of each curve was determined for $0.15 \leq \alpha \leq 0.85$. The deviation for $\alpha \leq 0.15$ may be explained by examination of electron micrographs in Figure 5.3a and b. While the particle is approximated as a cylinder, it initially has a greater amount of ASA than the SCPM assumes. The surface area does smooth considerably upon further oxidation as shown in Figure 5.3c. Deviation from the SCPM for $\alpha \geq 0.85$ can be explained by the observation that the platelets are made up of multiple crystallites. As α increases and platelet edge surface area decreases, the oxidation of the crystallite grain boundaries begins to contribute appreciably to the rate of oxidation. This causes the experimental data to deviate slightly from the SCPM. Additionally, the particle size distribution may have contributed to the deviation from the linear trend. The reaction rate observed was found to be insensitive to the level of conversion in the fitted range suggesting a pseudo-steady-state on the surface.

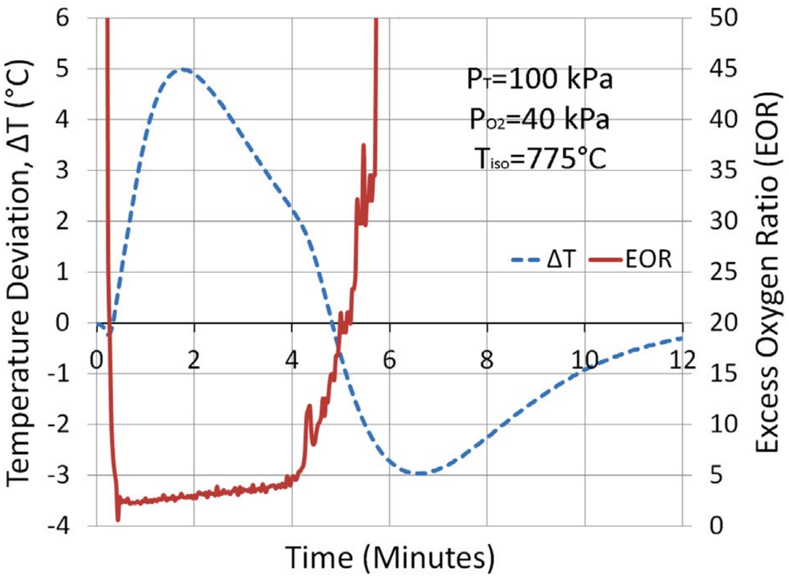

Figure 5.5 The temperature deviation from the isothermal set point and EOR vs. time. A sample temperature controller was used to minimize sample temperature deviation.

The SCPM did not provide an accurate description of the reaction above 725 °C for the higher oxygen partial pressures examined (10, 20 and 40 kPa). It was determined that gaseous transport effects became rate-limiting within the reaction system. As demonstrated in Figure 5.5, the sample temperature rose 5 °C within a minute of oxygen introduction to the system. The irregular shape of the temperature peak and the negative temperature deviation of the curve are the results of the sample temperature controller set to maintain the isothermal set point. The sample thermocouple, as in many thermogravimetric setups, was located below the sample crucible, thus it is plausible that the sample temperature deviation was substantially greater than 5 °C; however, even a 5 °C change may be considered substantial given the overall reaction rate was observed to approximately double with a temperature increase of 25 °C. The excess oxygen ratio also decreased significantly from initial values greater than 100 to approximately 3 and remained between 3 and 4 for a majority of the reaction. The low excess oxygen ratio brings into question the validity of the assumption that the surface oxygen concentration was equal to that of the bulk gas at high temperatures. Several methods are available for examining a system for which mass transfer and the chemical reaction must be considered [15, 72–76]. These models rely on the use of mass transfer correlations and introduce a much larger degree of uncertainty than desired in the current study; therefore, great care was taken to ensure that the mass transfer resistance was negligible.

5.3.2 Effective Kinetics Parameters

Since the graphite–oxygen reaction system is quite complex, the reaction order was initially assumed to be 1 with respect to oxygen. The resulting reaction rate constants are plotted in an Arrhenius plot for the oxygen isobars in Figure 5.6a. The most notable feature is the lack of linearity throughout the entire experimental temperature range. For 500–550 °C, the apparent activation energy is approximately 160 kJ/mol. Between 600 and 725 °C this value increases to nearly 225 kJ/mol. These values align quite well with typical overall activation energies of approximately 170–210 kJ/mol for carbon materials, including high purity graphites [17–25, 77]. Finally, above 750 °C, the apparent activation energy decreases to roughly 30 kJ/mol.

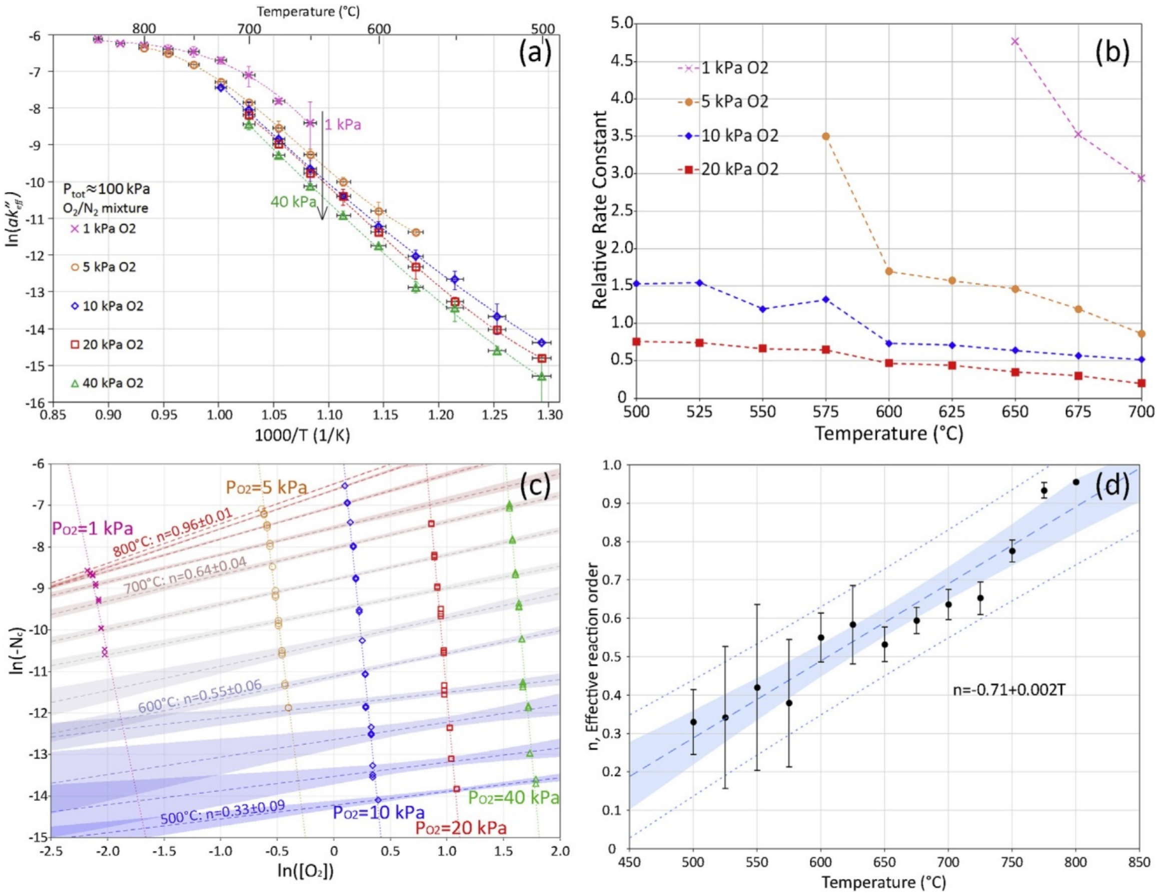

Figure 5.6 (a) An Arrhenius plot of SCPM data for the five experimental oxygen isobars. (b) A plot of the effects of oxygen partial pressure and temperature on ak''_{eff}. The reaction rate constants are plotted relative to $ak''_{eff}(T, 40\ kPa)$. (c) A ln-ln plot of carbon flux vs. oxygen concentration. The shaded regions represent the two sided 95% confidence interval for the linear fits of each temperature. The slopes from each isothermal set are plotted I (d) to show the change in effective reaction order with temperature. The shaded region and dotted line represent the two sided 95% confidence intervals for the linear fit and the individual data points, respectively. The error bars in all subplots represent two sided 95% confidence intervals about the sampled mean.

Two additional features observed are an increase in ak''_{eff} with decreasing oxygen partial pressure and the decrease in distance between the values of ak''_{eff} for a given set of oxygen partial pressures as temperature increases (Figure 5.6a and b).

5.3.3 Oxygen Transfer Model

As discussed in Section 5.1.3, the oxygen transfer mechanism (OTM) proposed by Radovic *et al.* [34–36] is thought to be a concise mechanism that is both sufficient and necessary to observations regarding the carbon–oxygen reaction system. Making a number of simplifying assumptions, an intrinsic rate equation can be written explicitly in terms of the reaction temperature and the concentration of molecular oxygen.

The OTM is comprised of the following reactions of the oxygen transfer mechanism:

$$C_e + O_2(g) \xrightarrow{k_{A1}} C_e(O_2) \tag{5.11a}$$

$$2C_e + O_2(g) \xrightarrow{k_{A2}} 2C_e(O) \tag{5.11b}$$

$$C_e(O_2) + C_b \xrightarrow{k_S} C_b(O) + C_e(O) \tag{5.12}$$

$$C_e(O_2) + C_b(O) \xrightarrow{k_{D1}} CO_2(g) + C_e(O) \tag{5.13a}$$

$$C_e(O) + C_b(O) \xrightarrow{k_{D2}} CO_2(g) \tag{5.13b}$$

$$C_e(O) \xrightarrow{k_{D3}} CO(g) \tag{5.13c}$$

The most obvious simplifications to the oxygen transfer mechanism are the removal of reactions (5.3b) and (5.5). The mobility of Cb(O) on the basal plane is quite high. It was assumed that the resistance to oxygen diffusion was much smaller than that of the adsorption or desorption processes and consequently not a rate limiting factor. NSD was neglected to simplify the mathematical complexity and eliminate the need to track each individual reaction site. Additionally, complete conversion can be achieved; therefore, site deactivation must eventually reverse.

The relationship between the rate of oxygen adsorption, reactions (5.2a) and (5.2b), and NSD is indeed complex. Jones and Jones [65], estimated ring closure to occur one order of magnitude faster than the maximum rate of oxygen adsorption; yet it was also stated that ‘‘a point may be reached when ring contraction would no longer be favored because of steric hindrance’’. This could be the result of graphite becoming increasingly strained to accommodate further ring closure, or due to the presence of oxygen complex on the surface [65, 66]. Radovic *et al.* [35], used DFT simulations to compare the deactivation of adjacent zigzag sites. When four adjacent active sites were modeled, ring closure occurred. When only two adjacent sites were modeled, ring closure did not occur due to the need for a substantial driving force; thus, further oxidation of the nascent sites would be expected.

Site anisotropy was also eliminated from the OTM; consequently, all reactive sites are considered equivalent. Silva-Tapia *et al.* [36] showed that reactions (5.2a) and (5.2b) are the major pathways for molecular and dissociative chemisorption, respectively; however, equal treatment of the carbene and carbyne type active sites greatly reduces the mathematical complexity, allowing an average intrinsic rate to be derived explicitly in terms of temperature and gaseous oxygen concentration. This simplification allows the general effects of reactions (5.2a) and (5.2b) to be observed without the need for an implicit solution to the intrinsic rate equation.

5.3.3.1 Derivation

The gaseous carbon flux outward from the graphite surface may be written out concisely in terms of reactions (5.13a–c) as

$$-N_C = k_{D1}^{*}[C_e(O_2)] + (k_{D2}^{*} + k_{D3})[C_e(O)] \tag{5.14}$$

Eq. (5.14) is of limited practical use in many cases because the surface concentrations, [C_e(O)] and [C_e(O_2)], are not easily determined. The surface concentrations can be determined for the OTM using the law of mass action to apply a differential mass balance about C_e, C_e(O), and C_e(O_2). It was assumed that the total number of edge sites per unit area of the {100} and {110} surfaces was constant. This allowed an edge site conservation equation

$$\Gamma_e = [C_e] + [C_e(O_2)] + [C_e(O)] \tag{5.15}$$

to be invoked. Eq. (5.15) was used directly to account for [C_e]. For the concentration of available sets of C_e sites (needed for reaction (11b)), [2C_e], it was assumed that

$$[2C_e] \approx \frac{1}{2}(\Gamma_e - [C_e(O_2)] - [C_e(O)]) \tag{5.16}$$

It should be noted that many of the reactions, such as reaction (5.13b), are not truly elementary reactions. It is assumed, in all cases, that these reactions have one transition state with a significantly larger energy barrier than other transition states within the reaction pathway. Consequently, the single largest transition state barrier dictates the rate of reaction. This was demonstrated via DFT by Orrego *et al.* [42] for reaction (5.13b). Furthermore, a pseudo-steady-state is assumed. Upon extensive algebraic manipulation and rearrangement [C_e(O)] and [C_e(O_2)] may be explicitly written in terms of the experimentally determined Arrhenius parameters, temperature, and the gaseous oxygen concentration at the gas–solid interface.

After substitution of the expressions for [C_e(O)] and [C_e(O_2)] and considerable rearrangement, Eq. (14) may be written as

$$-N_C(T,[O_2])=\frac{\left(k_{A1}k_{D1}^{*}+\left(k_{A1}+k_{A2}\right)\left(k_S^{*}+k_{D1}^{*}\right)\right)\left(k_{D2}^{*}+k_{D3}\right)\Gamma_e[O_2]}{\left(k_{A1}+k_{A2}\right)\left(k_S^{*}+k_{D1}^{*}\right)[O_2]+\left(k_{A1}[O_2]+k_S^{*}+k_{D1}^{*}\right)\left(k_{D2}^{*}+k_{D3}\right)} \tag{5.17}$$

Comparing Eq. (5.7) with (5.12) reveals that $ak_{\text{eff}}^{''}$ is a function of gaseous oxygen concentration as well as temperature where

$$ak_{eff}^{''}(T,[O_2])=\frac{\left(k_{A1}k_{D1}^{*}+\left(k_{A1}+k_{A2}\right)\left(k_S^{*}+k_{D1}^{*}\right)\right)\left(k_{D2}^{*}+k_{D3}\right)\Gamma_e}{\left(k_{A1}+k_{A2}\right)\left(k_S^{*}+k_{D1}^{*}\right)[O_2]+\left(k_{A1}[O_2]+k_S^{*}+k_{D1}^{*}\right)\left(k_{D2}^{*}+k_{D3}\right)} \tag{5.18}$$

5.3.3.2 Fit to Experimental Data

Equation 5.18 was used as a basis for the estimation of the rate constants of reactions 5.10a through 5.12c. All reaction rate constants were assumed to have an Arrhenius temperature dependence of the form $k_i(T) = k_{0i}e^{\frac{-E_i}{RT}}$. Data comparing the fit of the OTM for the estimated parameters is given in Table 5.2. The parameters k_{0i} and E_i are listed in Tables 5.3 through 5.5 for the optimization of all isobars, 1-10 kPa O_2, and 10-40 kPa O_2, respectively.

Table 5.2 **Absolute Relative Error Between Model and Experimental Data. The average, standard deviation, and maximum residual error are tabulated to show the effect of the three optimizations (All, 1-10 kPa, and 10-40 kPa isobars) on the residual error for each individual isobar as well as the entire set of experimental data.**

Fit	*All Isobars*			*1,5, and 10 Isobars*			*10, 20, and 40 Isobars*		
Statistics	**Avg.**	**StDev**	**Max**	**Avg.**	**StDev**	**Max**	**Avg.**	**StDev**	**Max**
All	35%	38%	156%	26%	21%	86%	39%	33%	132%
1 kPa	31%	45%	156%	19%	25%	86%	49%	18%	61%
5 kPa	65%	50%	140%	14%	9%	32%	66%	37%	132%
10 kPa	49%	27%	93%	9%	6%	23%	54%	29%	96%
20 kPa	9%	7%	24%	38%	11%	57%	16%	10%	34%
40 kPa	18%	9%	32%	52%	10%	62%	10%	8%	26%

Table 5.3 **Arrhenius Parameter Optimization of all Isobars. Activation energies expressed in kJ/mol. Dimensions for pre-exponential factors vary (see nomenclature section). Activation energies are given in kJ/mol.**

k_i	k_{A1}	k_{A2}	k^*_S	k^*_{D1}	k^*_{D2}	k_{D3}
k_{0i}	2.82E+03	3.45E+03	4.51E+06	9.92E+08	3.26E+08	1.75E+16
E_i	86	34	137	210	147	273

Table 5.4 **Arrhenius Parameter Optimization of 1, 5, and 10 kPa Isobars. Activation energies expressed in kJ/mol. Dimensions for pre-exponential factors vary (see nomenclature section). Activation energies are given in kJ/mol.**

k_i	k_{A1}	k_{A2}	k^*_S	k^*_{D1}	k^*_{D2}	k_{D3}
k_{0i}	2.09E+03	1.80E+03	9.02E+07	8.21E+08	3.31E+08	4.46E+16
E_i	71	28	113	200	148	289

Table 5.5 Arrhenius Parameter Optimization of 10, 20, and 40 kPa Isobars. Activation energies expressed in kJ/mol. Dimensions for pre-exponential factors vary (see nomenclature section). Activation energies are given in kJ/mol.

k_i	k_{A1}	k_{A2}	k^*_S	k^*_{D1}	k^*_{D2}	k_{D3}
k_{0i}	2.58E+03	1.66E+03	7.27E+07	1.05E+09	3.86E+08	4.05E+16
E_i	100	34	90	175	148	278

Table 5.2 indicates a “good” fit between the experimental results and the OTM. In the experimental temperature and O_2 partial pressure range used, the model’s predicted effective reaction rate constant is off by no more than a factor of 2.6. The fit of the 1, 5, and 10 kPa isobars, Table 5.4, produces the smallest overall residual error between model and experimental data. A plot of the optimized model for 1, 5, and 10 kPa data is given in Figure 5.7a. The OTM predicts the majority of the fitted data well with the exceptions of oxygen partial pressure data for 1 kPa below 700 °C and 20 and 40 kPa data above 600 °C. As seen in the residual error plot in Figure 5.7b, the magnitude of the residual error correlates roughly with the variation in partial pressure and the error is largest between 600 °C and 700 °C.

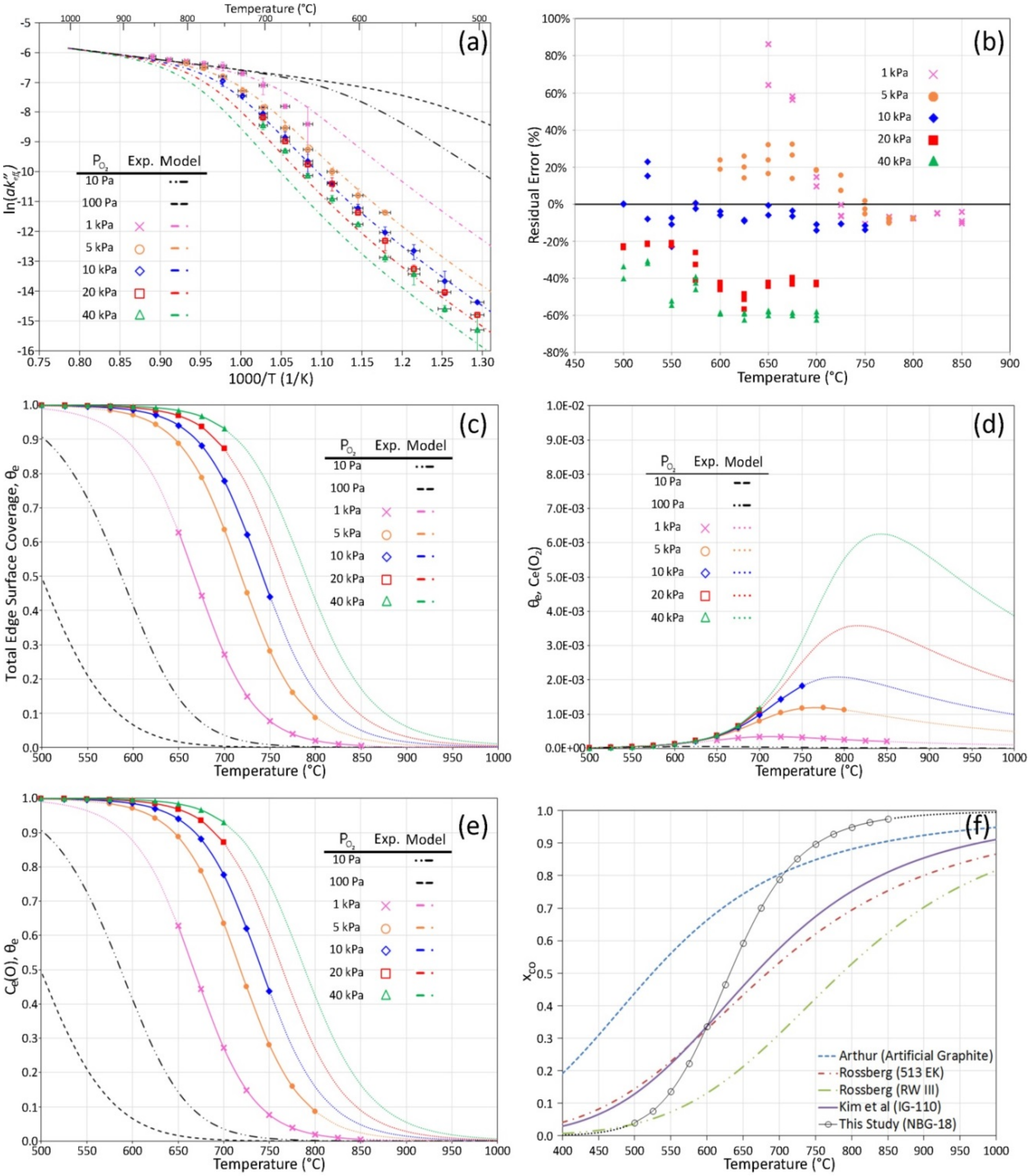

Figure 5.7 **Results from the OTM (a) compares ak''_{eff} of the experimental and fitted OTM using paramters from Table 5.4. The residual error between the experimental values and the OTM is shown in (b). The total surface complex coverage of the edge places (denoted θ_e) is shown in (c). (d and e) Show the surface coverage of the individual reactive surface complexes $C_e(O_2)$ and $C_e(O)$, respectively. (f) Shows the fractional carbon conversion to gaseous CO predicted by the OTM compared to empirical fits of experimental data for various carbon materials [17, 78, 79].**

5.3.3.3 Validation

As shown in Figure 5.7a, the OTM describes the observations made in Section 5.3.2 regarding the effective reaction rate constant. The low, intermediate, and high temperature regions correspond approximately with activation energies for the indirect desorption of CO_2, direct desorption of CO, and the dissociative chemisorption of oxygen, respectively. The OTM also accounts for the increase in ak''_{eff} with decreasing oxygen partial pressure, the decreasing difference between the values of ak''_{eff} with increasing temperature, and the experimentally observed temperature dependence of the effective reaction order. While a good fit to experimental observations is important, it does little to validate the accuracy of the individual reactions implied within the model. To validate the model, the fitted parameters for each reaction pathway are compared to available literature as well as key literature observations.

As is the case with much of the carbon oxidation literature, the range of values for the kinetics of oxygen adsorption on carbon is quite broad. Activation energies for adsorption of oxygen range from 0 to approximately 130 kJ/mol [34, 36, 61, 80–83]. Bansal *et al.* [82] observed five distinct chemisorption processes with increasing surface coverage for activated Graphon between -78° and 160 °C. The activation energies ranged from approximately 13 kJ/mol to 52 kJ/mol for low and high surface coverage, respectively. In a much later study, TGA/DSC was used to study the chemisorption of oxygen on Saran chars at 100 kPa between 77° and 222 °C to yield an activation energy of 47.7 ± 2.9 kJ/mol for surface coverage between 0.76 and 0.96 [81]. The activation energy for dissociative chemisorption of oxygen in the OTM falls right in the middle of this range. As seen in Figure 5.7c–e θ_e, varies both with temperature and pressure.

Higher equilibrium θ_e is maintained for greater oxygen partial pressures. The OTM implicitly assumes that reaction rate constants are independent of surface coverage and surface species interactions.

Comparison of the optimized parameters for 1, 5, and 10 kPa O_2 and 10, 20, and 40 kPa do show an increase in activation energies for the adsorption processes which may result from differences in the average θ_e for the optimizations. Silva-Tapia *et al.* [36] used DFT simulations to show that the dissociative chemisorption of oxygen should occur on the carbyne type armchair sites with an activation energy of approximately 3 kJ/mol for carbon nanotubes and 28 kJ/mol for graphene. For molecular chemisorption, Radovic *et al.* [34,36] predicted activation energies between 71 and 80 kJ/mol on carbene type zigzag site for carbon nanotubes and graphene, respectively. These calculations did not consider the effects of surface complexes on the edge or basal planes. The remaining literature found on the chemisorption of oxygen ranges from 54 to 134 kJ/mol. Kelemen and Freund [61] using Auger electron spectroscopy found activation energies ranging from 54 to 134 kJ/mol, respectively for θ_e ranging from 0.2 to 0.9, respectively. Finally, Walker *et al.* [80], using thermoelectric power measurement on pressed bars of high purity graphite flakes, measured an activation energy of 125 ± 8 kJ/mol for temperatures between 327° and 452 °C and an oxygen partial pressure of 100 kPa. No significant variation of the activation energy was found with the reported quantities of adsorbed oxygen. From Figure 5.7c it is expected that the surface coverage would be quite high throughout the experimental range. Walker *et al.* [80] also reported a pre-exponential factor equivalent to $2.2\text{x}10^3 \frac{\mathrm{m}^3}{\mathrm{mol\,s}}$. This is the same order of magnitude as the pre-exponential factors predicted for reactions (11a) and (11b).

To the best of the authors' knowledge an activation energy for the spill-over of oxygen to the basal plane has not been measured experimentally; however, Radovic *et al.* [57], estimated the activation energy to overcome the transition state between the reactant and products side of reaction (12) to be approximately 130 kJ/mol using DFT. The parameter optimizations in Tables 5.4 and 5.5 result in slightly lower activation energies of approximately 110 and 90 kJ/mol, respectively. A decrease in the activation energy is observed between Tables 5.4 and 5.5; However this does not necessarily imply a decrease in the activation energy with increasing surface complex concentrations as the difference is likely within the range of experimental uncertainty. Further experimental work and DFT simulations should be used to make such an inference.

Literature for the desorption of CO_2 and CO from the active surface area is quite abundant. Experimentally it has been shown that the activation energy for surface complex removal decreases with increasing surface coverage [37, 39, 77]. Tables 5.4 and 5.5 show a decrease in the optimized activation energy for direct CO_2 and CO adsorption at higher average surface coverage. DFT has also suggested that desorption energies are substantially lowered (~30% decrease) by the presence of the epoxide on the basal plane. These facts, at least in part, can account for the broad range of observed activation energies. For CO_2 desorption, activation energies range from approximately 120 to 250 kJ/mol for high and low surface coverage, respectively [61, 76, 77]. Orrego *et al.* [42] determined for indirect CO_2 desorption an activation energy of approximately 145 kJ/mol. The proposed energy barrier is due to the rearrangement of the seven-member ring after oxygen insertion (unzipping) into a four-membered ring lactone group subsequent to desorption. The optimized activation energy from Tables 5.4 and 5.5 is

148 kJ/mol. A proposed reaction pathway for direct CO_2 desorption was estimated via DFT to have an activation energy of 203 kJ/mol [43]. The presence of $C_b(O)$ on the basal plane is critical for the decomposition, as the activation energy would otherwise be significantly higher. The molecular beam study by Olander *et al.* [59] suggested that at 1177 °C the direct production route for CO_2 should account for 80–90% of the total evolved CO_2. The OTM at this same temperature predicts approximately 80% of CO_2 will be formed via the direct path.

Activation energies for CO desorption in the literature generally range from 240 kJ/mol at high surface coverage to 350 kJ/mol at low surface coverage [28, 61]. The kinetics of desorption for CO via a semiquinone carbon–oxygen complex determined via DFT in the absence of other functional groups yielded an activation energy of 396 kJ/mol and a pre-exponential factor of $1.81 \cdot 10^{17}$ s^{-1}. This pre-exponential factor is in good agreement with the optimized values in Tables 5.2–5.4. If a stable surface complex is assumed to be near the $C_e(O)$ complex, assuming a 30% reduction in the carbon–carbon bond energy and equivalent reduction in the activation energy for desorption, the activation energy would be closer to 280 kJ/ mol. This value is comparable to that of the optimized OTM. The OTM is also capable of predicting the CO/CO_2 ratio.

$$\frac{CO}{CO_2} = \frac{k_{D3}(k_{A1}+k_{A2})(k_S^*+k_{D1}^*)}{k_{A1}k_{D1}^*(k_S^*+k_{D1}^*)+k_{D2}^*(k_{A1}+k_{A2})(k_S^*+k_{D1}^*)} \tag{5.19}$$

Although no experimental data was collected for the product ratio, the model fits reasonably with other published literature shown in Figure 5.7f. The experimental values for the CO/ CO_2 ratio are often fitted empirically to an Arrhenius model. Values of the empirical activation energy vary significantly depending on the experimental conditions.

Phillips *et al*. [84, 85] reported an empirical value of approximately 27 kJ/mol for oxygen partial pressures between approximately 1 and 27 Pa and temperatures ranging from 525 to 625 °C. Arthur [78] found that for both a natural graphite and a coal char (460–900 °C and oxygen partial pressures of 5–25 kPa) the empirical activation energy was 51 kJ/mol. Rossberg [79], for two electrode carbons (520–1420 °C), found somewhat higher values of 60 and 78 kJ/mol. Kim *et al*. [17] reported an activation energy of approximately 70 kJ/mol for temperatures between 950 and 1800 °C and oxygen partial pressures varying between 5 and 20 kPa. The flows used in these experiments, with the exception of Phillips *et al.* [84], were well below the velocity of approximately 51 $\frac{\mathrm{m}}{\mathrm{s}}$ needed to prevent secondary oxidation of CO [84]. Additionally, reactions between the CO and the reactive surface complexes may have occurred, artificially decreasing the CO/CO_2 ratio. The empirical activation energy resulting from the OTM using the optimized parameters from Table 5.4 results is 141 kJ/mol. Examination of Table 5.4 shows that the activation energy is the difference between the activation energies for reactions (5.13b) and (5.13c), suggesting, as in much of the literature, that the empirical activation energy is related to the energy difference for desorption of CO and CO_2. Upon analysis of the terms in the numerator and denominator of Eq. (5.19), the following simplification is realized over the temperatures and oxygen concentrations of the experimental data.

$$\frac{CO}{CO_2} \approx \frac{k_{D3}}{k_{D2}^*} \tag{5.20}$$

Neither Eq. (5.19) nor (5.20) have any direct dependence on the oxygen concentration within the system. Phillips *et al.* [85] showed that the amount of stable complex formed, $C_b(O)$, was strongly dependent on the initial oxygen concentration within the system and the product ratio decreased with increasing oxygen concentration. This observation suggests that the product ratio is a function of the concentration of $C_b(O)$ on the basal plane. Noting that $k_{D2}^* = k_{D2}[C_b(O)]$,

$$\frac{CO}{CO_2} \approx \frac{k_{D3}}{k_{D2}[C_b(O)]} \tag{5.21}$$

which is of the same form derived by Skokova and Radovic [86] for an early form of the oxygen transfer mechanism. Intuitively from reactions (5.11a) and (5.11b) an increase in the system's oxygen concentration should increase the concentration of the stable oxygen complex on the basal plane. This is in good agreement with the findings of Phillips *et al.* [85]. The degree to which the concentration of the stable surface complex increases is also dependent upon the equilibrium rate of consumption of the complex.

5.3.3.4 Deficiencies

The OTM fits the experimental kinetics data, and the optimized parameters agree well with literature for the corresponding reaction pathways used; however, there are some deficiencies within the model. The first is the failure to predict changes in the product ratio with changing oxygen concentration. The change in product ratio may be accounted for in the model by dropping the simplification of k_S, k_{D1}, and k_{D2} to k_S*, k_{D1}*, and k_{D2}* and using an implicit method for solve the conservation equations for the five surface species. In addition, careful consideration must be given to the concentration of the epoxide on the basal plane bearing in mind that it is only consumed at the edge. Skokova and Radovic [86] observed an inversely proportional relationship between the product ratio and the crystallite size. This could suggest that, at least for small crystallites the migration of stable complex on the basal plane must be taken into consideration (reaction 5.3b), as its (in)ability to diffuse away from the crystallite edge will affect the concentration near the RSA.

Another deficiency is the failure to account for the known dependency of reaction parameters on surface coverage. Although Tables 5.4 and 5.5 do show the correct general trends of the reaction parameters for the lower and higher ''average'' surface coverage, the optimized parameters only reflect an average value rather than the actual value throughout the fitted range of experimental data. Accounting for this dependency may eliminate a majority of the experimental residual error. The dependency may be added to the activation energies as a correction factor that varies with θ_e. This method should decrease the residual error of the model, but has no physical meaning.

Next, in the model derivation, Eq. (5.16) is used to describe the concentration of available sites for dissociative chemisorption of oxygen. This assumption is expected to be a good approximation at low to moderate surface coverage. At high surface coverage, this assumption may become increasingly inaccurate. Although dissociative chemisorption is expected to occur nearly exclusively on the carbyne type armchair sites, the model assumes no site specificity. The lack of site specificity makes each individual carbon edge site a potential adsorption site and near the maximum surface coverage, Eq. (5.16) will not describe the availability of edge site pairs. This may in part explain the lack of conformity of the OTM with the high pressure studies of Ranish and Walker [64]. At the temperatures and pressures of Ranish and Walker's experiments, the OTM predicts that the reaction is nearly independent of oxygen concentration, whereas their experimental data shows an increase in the reaction order with decreasing oxygen partial pressure.

Finally, the OTM assumes that the maximum achievable concentration of edge surface complex is C_e. C_e was set to $2.01\text{x}10^{-5}\,\frac{\text{mol}}{\text{m}^2}$, the average of the ideal (100) and (110) planar densities. On the nano-scale this appears to be a valid assumption given the atomic level smoothness observed in the micrographs of Figure 5.8; however, the assumption that all carbon sites are equally available as potential reaction sites may be questionable.

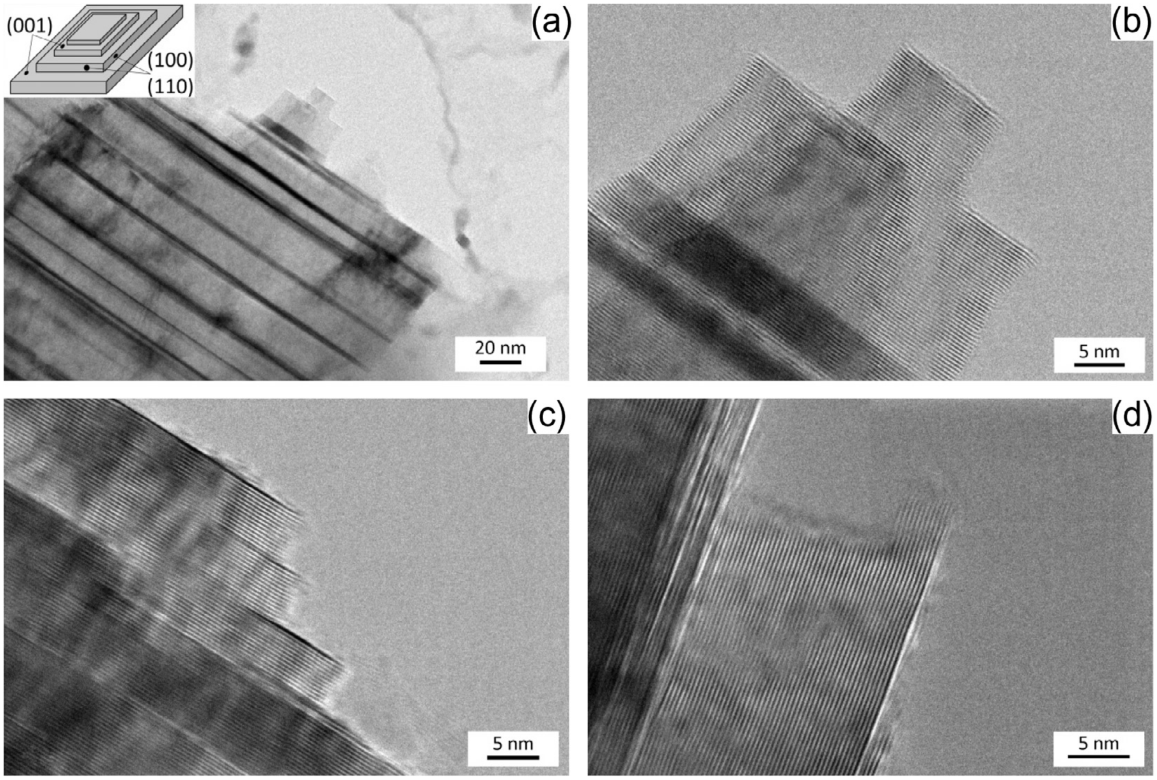

Figure 5.8 The figure shows high resolution transmission electron micrographs of NBG-18 graphite. The reaction progression along the edge plane steps appears uniform. (a) Shows terracing commonly observed in large crystallites within the filler particles. The inset depicts the terracing. (b) Is the tip of the crystallite from (a). (c and d) Show the terracing at the edges of crystallites.

5.4 Conclusions

An intrinsic isothermal reaction model of the carbon–oxygen reaction system has been developed for application to high-purity graphites. Based on the oxygen transfer mechanism proposed by Radovic *et al.* [34, 35], the parameters of the oxygen transfer model are physically meaningful and directly comparable to experimental and theoretical calculations. Model parameters were determined from kinetics experiments for NBG-18 graphite in an oxygen/nitrogen reaction system between 500 and 850 °C using oxygen partial pressures of 1, 5, 10, 20, and 40 kPa. All experimentally optimized parameters agreed well with experimental and theoretical literature. The dissociative chemisorption of oxygen, indirect desorption of CO_2, and direct desorption of CO were found to have activation energies of 28, 150, and 290 kJ/mol, respectively. Additionally, an experimental activation energy for the spill-over of oxygen onto the basal plane was determined (113 kJ/mol).

The oxygen transfer model also follows several important experimental trends and observations from the literature. It shows an increasing effective reaction rate constant with decreasing oxygen concentration, an increase in the effective reaction order (with respect to oxygen concentration) at moderate oxygen concentrations, and follows the empirical Arrhenius dependence of the CO/CO_2 ratio on reaction temperature. It also predicts the dominant reaction product to be CO_2 at low temperatures and high surface coverage and CO at high temperatures and low surface coverage. Finally, it predicts the dominance of the direct CO_2 formation route over the indirect route at high temperatures.

The oxygen transfer mechanism was purposefully derived to be a compromise between simple explicit use/implementation and intrinsic accuracy. The deficiencies observed in the model are likely the direct result of the mathematical simplifications used. Further expansion of the model is quite feasible and would theoretically increase the accuracy; however, such expansion would also decrease the practicality of using the model for inversely extracting kinetics parameters as well as decrease the certainty of the parameters.

5.5 Author Justification

The research presented in this publication was carried out and authored by Joshua Kane as a partial fulfillment of the requirements for a Doctoral degree in Materials Science and Engineering at Boise State University, under the advisement and supervision of Dr. Darryl P. Butt. Dr. Karthik Chinnathambi contributed to the microscopy of many oxidized samples examined as well as provided critical feedback and editing of the article in all stages of its preparation. Dr. Rick Ubic, Dr. William E. Windes, and Dr. Darryl P. Butt contributed greatly in terms of financial support, detailed discussion of mechanisms, and provided in-depth critical reviews of the article throughout the writing process.

5.6 References

[1] World Coal Institute. The coal resource: a comprehensive overview of coal, 48. Available from: http://www.worldcoal.org/resources/wca-publications/; 2005 [cited 07.11.12].

[2] T. R. Allen, K. Sridharan, L. Tan, W. E. Windes, J. I. Cole, D. C. Crawford, and G. S. Was, "Materials challenges for Generation IV nuclear energy systems," *Nucl. Technol.*, **162**[3] (2008).

[3] W. Windes, T. Burchell, and R. Bratton, Graphite technology development plan, INL/

EXT-07-13165, Idaho National Laboratory, September 2007.

[4] ASTM Standard D7219, 2008. Standard specification for isotropic and near isotropic nuclear graphites. West Conshohocken (PA): ASTM International; 2003. http://dx.doi.org/10.1520/D7219-08.

[5] W. P. Eatherly and E. L. Piper, "Manufacturing"; pp. 21-51 in *Nuclear Graphite*. Edited by R.E. Nightingale, Academic Press, 1962.

[6] ASTM Standard C781, 2008. Standard practice for testing graphite and boronated graphite materials for high-temperature gas-cooled nuclear reactor components. West Conshohocken (PA): ASTM International; 2003. http:// dx.doi.org/10.1520/C0781-08.

[7] T. D. Burchell, R. Bratton, and B. Marsden, "Next Generation Nuclear Plant Phenomena Identification and Ranking Tables (PIRTS)"; Vol. 5 Graphite PIRT, USNRC, NUREG/CR-6944, ORNL/TM-2007/147, 2008.

[8] A. Tarpinian, and G.E. Gazza, "A technique for the microstructural examination of polycyrstalline graphites" Report WAL-TR- 132.5/1. Watertown Arsenal Laboratory; February 1959.

[9] J. Kane, C. Karthik, D. P. Butt, W. E. Windes, R. Ubic, "Microstructural characterization and pore structure analysis of nuclear graphite," *J. Nucl. Mater.*, **415** [2] 189-197 (2011).

[10] C. Karthik, J. Kane, D. P. Butt, W. E. Windes, R. Ubic, "Microstructural Characterization of Next Generation Nuclear Graphites." *Micros. Microanal.*, **18**, 272-278 (2012).

[11] K. Y. Wen, J. Marrow, and B. Marsden, "Microcracks in nuclear graphite and highly oriented pyrolytic graphite (HOPG)," *J. Nucl. Mater.*, **381**[1-2] 199-203 (2008).

[12] G. F. Hewitt, "Gaseous mass transport within graphite"; pp. 121 in Chemistry and Physics of Carbon, Vol 1. Edited by P. L. Walker Jr. Dekker, New York, 1965.

[13] M. Sahimi, G. R. Galvalas, and T. T. Tsotsis, "Statistical and continuum models of fluid-solid reactions in porous media," *Chemi. Eng. Sci.,* **45**, 1443-1502 (1990)

[14] S. Miura, P. L. Silveston, and K Hashimoto "Analysis of pore development processes during gasification of a carbon char," *Carbon*, **13**, 391-400 (1975).

[15] J Szekely, J. W. Evans, and H. Y. Sohn, "Gas–solid reactions"; New York: Academic Press; 1976.

[16] C. I. Contescu, S. Azad, D. Miller, M. J. Lance, F. S. Baker, and T. D. Burchell, "Practical aspects for characterizing air oxidation of graphite," *J. Nucl. Mater.*, **381**, 15-24 (2008).

[17] E. S. Kim and H. C. No, "Experimental study on the oxidation of nuclear graphite and development of an oxidation model," *J. Nucl. Mater.*, **349**, 182-194 (2006).

[18] H. Yang, H. Eun, D. Lee, C. Jung, and K. Lee, "Analysis of combustion kinetics of powdered nuclear graphite by using a non-isothermal thermogravimetric method," *J. Nucl. Sci. Technol.*, **43**, 1436-1439 (2006).

[19] H. Kawakami, "Air oxidation behavior of carbon and graphite materials or HTGR," *Tanso*, **124**, 26-33 (1994).

[20] S. Chi and G. Kim, "Comparison of oxidation rate and degree of graphitization of selected IG and NBG nuclear grades," *J. Nucl. Mater.*, **381**, 9-14 (2008).

[21] E. S. Kim, H. C. No, B. J. Kim, and C. H. Oh, “Estimation of graphite density and mechanical strength variation of VHTR during air-ingress accident,” *Nucl. Eng. Des.*, **238**[4], 837-847 (2008).

[22] L. Xiaowei, R. Jean-Charles, and Y. Suyuan, “Effect of temperature on graphite oxidation behavior,” *Nucl. Eng. Des.,* **227**[3], 273-280 (2004).

[23] H. K. Hinssen, K. Kühn, R. Moorman, B. Schlögl, M. Fechter, and M. Mitchell, “Oxidation experiments and theoretical examinations of graphite materials relevant for PBMR,” *Nucl. Eng. Des.*, **238**[11], 2018-2025 (2008).

[24] R. Moormann, H.K. Hinssen, and K. Kühn, “Oxidation behavior of an HTR fuel element matrix graphite in oxygen compared to a standard nuclear graphite,” *Nucl. Eng. Des.*, **227**, 281-284 (2004).

[25] E. L. Fuller and J. M. Okoh, “Kinetics and mechanisms of the reaction of air with nuclear grade graphites: IG-110,” *J. Nucl. Mater.*, **240**, 241-250 (1997).

[26] P. L. Walker Jr “Carbon: an old but new material revisited,” *Carbon*, **28**, 261–279 (1990).

[27] A. Montoya, F. Mondragón, and T. N. Truong “First-principles kinetics of CO desorption from oxygen species on carbonaceous surface,” *J. Phys. Chem. A*, **106**, 4236–4239 (2002).

[28] B. Marchon, J. Carrazza, H. Heinemann, and G. A. Somorjai, “TPD and XPS studies of O_2, CO_2, and H_2O adsorption on clean polycrystalline graphite,” *Carbon*, **26**[4] 507-514 (1988).

[29] J. M. Thomas, “Reactivity of carbon: some current problems and trends,” *Carbon*, **8**, 413-421 (1970).

[30] P. L. Walker Jr, F. Rusinko, and L. G. Austin, “Gas reactions of carbon” pp. 133-221 in *Advances in catalysis, vol. 11.* Edited by D. D. Eley, P. W. Selwood, and P. B. Weisz. Academic Press, New York, 1959.

[31] P. L. Walker Jr, T. L. Taylor, J. M. Ranish, “An update on the carbon– oxygen reaction,” *Carbon*, **29**, 411-421 (1991).

[32] L. R. Radovic, “Carbon and graphite reactivity”; in *Encyclopedia of materials: science and technology*. Edited by K. H. J. Buschow, R. W. Cahn, M. C. Flemings, B. Ilschner, E, J. Kramer, and S. Mahajan. Elsevier, New York 2001.

[33] N. R. Laine, “A mass spectrometric study of the carbon–oxygen reaction– 27 years Later,” *Carbon*, **29**[6] 729-733 (1991).

[34] L. R. Radovic, “Active sites in graphene and the mechansim of CO_2 formation in carbon oxidation,” *J. Am. Chem. Soc.*, **131**, 17166-17175 (2009).

[35] L. R. Radovic, A. F. Silva-Villalobos, A. B. Silva-Tapia, and F. Vallejos- Burgos, “On the mechanism of nascent site deactivation in graphene,” *Carbon*, **49**, 3471-3487 (2011).

[36] A. B. Silva-Tapia, X. García-Carmona, and L. R. Radovic, “Similarities and differences in O_2 chemisorption on graphenenanoribbon vs. carbon nanotube,” *Carbon*, **50**, 1152-1162 (2012).

[37] F. J. Vastola, P. J. Hart, and P. L. Walker Jr, “A study of carbon–oxygen surface complexes using O18 as a tracer,” *Carbon*, **2**[1] 65-71 (1964).

[38] P. J. Hart, “Oxygen-18 tracer and low temperature chemisorption studies of the carbon–oxygen reaction”; Penn State Univ, Ph.D. Thesis. University Park, PA, 1966.

[39] K. Skokova and L. R. Radovic, “On the role of carbon–oxygen surface complexes in the carbon/oxygen reaction mechanism”; pp. 143-147, American Chemical Society (Div. Fuel Chem. Pre-prints) ACS. Washington D.C., 1996.

[40] S. G. Chen, R. T. Yang, F. Kapeteijn, and J. A. Moulihn, “A new surface oxygen complex on carbon: toward a unified mechanism for carbon gasification reactions,” *Ind. Eng. Chem. Res.*, **32**, 2835-2840 (1993).

[41] A. Montoya, T. T. Truong, F. Mondragón, and T. N. Truong, “CO desorption from oxygen species on carbonaceous surface: 1. Effects of the local structure of the active site and the surface coverage,” *J. Phys. Chem. A*, **105**, 6757-6764 (2001).

[42] J. F. Orrego, F Zapata, T. N. Truong, and F. Mondragón, “Heterogeneous CO_2 evolution from oxidation of aromatic carbon-based materials,” *J. Phys. Chem. A*, **113**, 8415-8420 (2009).

[43] A. Sánchez and F. Mondragón, “Role of the epoxy group in the heterogeneous CO_2 evolution in carbon oxidation reactions,” *J. Phys. Chem. C*, **111**, 612-617 (2007).

[44] L. R. Radovic and K. Skokova, “Electron density in graphene layers: implications for carbon reactivity”; pp. 223-229, American Chemical Society (Div. Fuel Chem. Pre-prints) ACS. Washington D.C., 2000.

[45] M. H. Back, “Comment on an update on the carbon–oxygen reaction,” *Carbon*, **29**, 1290-1291 (1991).

[46] N. R. Laine, F. J. Vastola, and P. L. Walker Jr, "The importance of active surface area in the carbon oxygen reaction," *J. Phys. Chem.*, **67**, 2030-2034 (1963).

[47]L. R. Radovic and B. Bockrath, "On the chemical nature of graphene edges: origin of stability and potential for magnetism in carbon materials," *J. Am. Chem. Soc.*, **127**, 5917-5927 (2005).

[48] J. M. Thomas, "Microscopic studies of graphite oxidation"; pp. 73 in Chemistry and Physics of Carbon, Vol. 1. Edited by P. L Walker Jr. Dekker, New York, 1965.

[49] G. R. Hennig, "Electron microscopy of reactivity changes near lattice defects in Graphite"; pp. 1 in Chemistry and Physics of Carbon, Vol. 2. Edited by P. L Walker Jr. Dekker, New york, 1966.

[50] L. R. Radovic, A. Suarez, F. Vallejos-Burgos, and J. O. Sofo, "Oxygen migration on the graphene surface. 2. Thermochemistry of basal-plane diffusion (hopping)," *Carbon*, **49**[13] 4226-4238 (2011).

[51] F. Rouquerol, J. Rouquerol, and K. Sing, "Adsorption by powders and porous solids"; Academic Press, London, UK, 1999.

[52] S. Lowell, J. E. Shields, M. A. Thomas, and M. Thommes, "Characterization of porous solids and powders: surface area, pore size and density"; Springer, Dordrecht, The Netherlands, 2006.

[53] T. Kyotani, C. A. Leon y Leon, and L. R. Radovic, "Simulation of carbon gasification kinetics using an edge recession model," *AIChE J.*, **39**[7] 1178-1185 (1993).

[54]A. A. Lizzio , H. Jiang, and L. R. Radovic, "On the kinetics of carbon (Char) gasification: reconciling models with experiments," *Carbon*, **28**[1] 7-19 (1990).

[55] R. L. Taylor, “Low-temperature gasification and chemisorption studies of the carbon–oxygen reaction”; Penn State Univ, Ph.D. Thesis. University Park, PA, 1982.

[56] R. T. Yang and C. Wong, “Kinetics and mechanism of oxidation of basal plane on graphite,” *J. Chem. Phys.*, **75**, 4471-4476 (1981).

[57]L. R. Radovic, A. B. Silvia-Tapia, and F.Vallejos-Burgos, “Oxygen migration on the graphene surface. 1. Origin of epoxide groups,” *Carbon*, **49**[11] 4218-4225 (2011).

[58] E. G. Seebauer and C. E. Allen, “Estimating surface diffusion coefficients,” *Prog. Surf. Sci.*, **49**, 265-330 (1995).

[59] D. R. Olander, R. H. Jones, J. A. Schwarz, and W. J. Siekhaus, “Reactions of modulated molecular beams with pyrolytic graphite. II. Oxidation of the prism plane,” *J. Chem. Phys.*, **57**, 421-433 (1972).

[60] J. Lahaye and P. Ehrburger, “Fundamental issues in control of carbon gasification Reactivity”; In proceedings of the NATO advanced study workshop. Academic Publishers, 1991.

[61] S. R. Kelemen and H. Freund, “O_2 oxidation studies of the edge surface of graphite,” *Carbon*, **23**, 619-625 (1985).

[62] R. N.Smith, D. A. Young, and R. A. Smith, “Infra-red study of carbon– oxygen surface complexes,” *Trans. Faraday. Soc.*, **62**, 2280-2286 (1966).

[63] G. Tremblay, F. J. Vastola, and P. L. Walker Jr, “Thermal desorption analysis of oxygen surface complexes on carbon,” *Carbon*, **16**, 35-39 (1978).

[64] J. M. Ranish and P. L. Walker Jr, “High pressure studies of the carbon– oxygen reaction,” *Carbon*, **31**[1] 135-141 (1993).

[65] J. M. Jones, and D. H. Jones, “Modeling the competition between annealing and oxidation in the carbon–oxygen reaction,” *Carbon*, **45**[3] 677-680 (2007).

[66] O. Senneca, P. Salatino, and M. Sabato, “The influence of char surface oxidation on thermal annealing and loss of carbon reactivity,” *Proc. Combust. Inst.*, **30**, 2223-2230 (2005).

[67] J.D.Lambert, “The effect of certain metals on the oxidation process of carbon,” *Trans. Faraday. Soc.*, **32**, 1080-1083 (1936).

[68] D. J. Allardice and P. L. Walker Jr, “The effect of substitutional boron on the kinetics of the carbon–oxygen reaction,” *Carbon*, **8**, 375-385 (1970).

[69] J. M. Ranish, “. Kinetics of the carbon–oxygen reaction”; Penn State Univ, Ph.D. Thesis. University Park, PA, 1984.

[70] J. A. Nelder and R. Mead, “A simplex method for function minimization,” *Comput. J.*, **7**, 308-313 (1965).

[71] O. Levenspiel, “Chemical reactor omnibook”; pp 51.1-55.25 OSU Book Stores Inc., Corvallis, OR, 1996.

[72] O. Levenspiel, “Chemical reaction engineering. 3rd ed.”; pp. 567-586. John Wiley & Sons Inc., Hoboken NJ, 1999.

[73] D. E. White and J. J. Carberry, “Kinetics of gas–solid non-catalytic reactions,” *Can. J. Chem. Eng.*, **43**, 334-337 (1965).

[74] J. Shen and J. M. Smith, “Diffusional effects in gas solid reactions,” *Ind. Eng. Chem. Fund.*, **4**, 293-310 (1955).

[75] R. A. Svehla, “Estimated viscosities and thermal conductivities of gases at high Temperatures”; Technical Report R-132, NASA 1962.

[76] A. S. Parkerand H. C. Hottel, “Combustion rate of carbon study of gas-film structure by microsampling,” *Ind. Eng. Chem.*, **28**, 1334-1341 (1936).

[77] S. Ahmed and M. H. Back, “The role of the surface complex in the kinetics of the reaction of oxygen with carbon,” *Carbon*, **23**, 513-524 (1985).

[78] J. R. Arthur, “Reactions between carbon and oxygen,” *Trans. Faraday. Soc.*, **47**, 164-178 (1951).

[79] V. M. Rossberg, “Experimentelle Ergebnisse uber die Primarreaktionen bei der Kohlenstoffverbrennung,” *Z. Elektrochem.*, **60**, 952-956 (1956).

[80] P. L. Walker Jr, L. G. Austin, and J. J. Tietjen, “Oxygen chemisorption effects on graphite thermoelectric power”; pp. 327-365 in Chemistry and Physics of Carbon Vol. 1. Edited by P. L. Walker Jr., Dekker, New York, 1965.

[81] I. M. K. Ismail and P. L. Walker Jr, “Detection of low temperature gasification using DSC and TGA,” *Carbon*, **27**[4] 549-559 (1989).

[82] R. C. Bansal, F. J. Vastola, and P. L Walker Jr, “Studies on ultraclean carbon surfaces: II. Kinetics of chemisorption of graphon,” *J. Colloid. Interface. Sci.*, **32**[2] 187-194 (1970).

[83] K. Sendt and B. S. Haynes, “Density functional study of the chemisorption of O_2 on the zig-zag surface of graphite,” *Combust. Flame*, **143**, 629-643 (2005).

[84] R. Phillips, F. J. Vastola, and P. L. Walker Jr, “Factors affecting the product ratio of the carbon–oxygen reaction – II. Reaction temperature,” *Carbon*, **8**, 205-210 (1970).

[85] R. Phillips, F. J. Vastola, P. L. Walker Jr., “The effect of oxygen pressure and carbon burn-off on the product ratio of the carbon–oxygen reaction,” *Carbon*, **7**, 479-485 (1969).

[86] K. Skokova, L. R. Radovic, “CO/CO_2 ratio in the products of the carbon–oxygen Reaction”; pp. 608-609 In Proceedings of the 22nd biennial conference on carbon, American Carbon Society, San Diego, CA, 1995.

CHAPTER SIX: CONCLUSIONS

Graphite material properties are highly dependent on the initial carbon source material, coke type, ratios of filler, binder and impregnation material, and processing specifications. This allows for a great deal of versatility in the material properties, but also implies that each new grade is a unique uncharacterized carbon material.

Since historical graphite grades used in past HTGRs are no longer available new candidate grades must be qualified and characterized prior to application in the future VHTR. The work included in this dissertation has focused on the thorough characterization of the microstructure of several candidate grades, defects that affect swelling and shrinkage of nuclear graphites under irradiation, and the reaction mechanism of the graphite-oxygen reaction system.

In Chapter Two the microstructures of IG-110, NBG-18, and PCEA were characterized using bright-field transmission electron microscopy. In all grades examined, both the binder and filler were well graphitized, however the range of the order is much smaller in binder compared to individual cyrstallites in the filler. Turbostratic graphite identified by an elliptical diffraction pattern was also observed in all grades. The turbostractic graphite has close-packed carbon planes that are curled and rotated with respect to each other. The simultaneous presence of translational and rotational disorder results in the distribution of scattering power in the reciprocal lattice to form concentric cylinders. The turbostratic regions were found to be inherent to the microstructure rather than artifacts of sample preparation. The quantity of QI particles and chaotic structures was higher in NBG-18 graphite which was attributed the coal-tar pitch source. Finally, the microcracks (Mwrozowski cracks) observed in the filler material of each grade varied in size and shape. Microcracks in NBG-18 were small and appeared in large clusters within cyrstallites whereas PCEA microcracks were much larger (in width and length), but were less frequent. The differences in microcrack size and density would be expected to effect the overall shrinkage and swelling characteristics of each grade under irradiation.

Chapter Three examined the atomic level processes involved in the swelling and crack-closure using noise-filtered lattice images. In situ high resolution transmission electron microcopy provided direct experimental evidence for the formation of vacancy loops and interstitial loops in graphite irradiated with an electron beam at room temperature. Observation of interstitial loops to be highly unstable and few in number make it unlikely to contribute appreciably to the observed swelling in nuclear graphite under irradiation. Observation of vacancy loops in much larger quantities lead to the conclusion that the swelling of graphite along the c-axis and closure of microcracks is mainly caused by the new basal planes introduced by the positive climb of dislocation dipoles created by vacancy loops. This conclusion contradicts much of the initial theory as to the mechanism for the macroscopic swelling of graphite along the c-axis, but is supported by the lack of clear microstructural evidence for the formation and growth of such new interstitial planes [1].

Chapter Four analyzed microstructural features of the filler and macro-porosity in IG-110, PGX, NBG-18, and PCEA graphites. Average size and aspect ratios were determined for the filler particles from large sample populations. It was found that qualitatively the aspect ratio of the filler particle cross-sections observed increased with the degree of crystallite alignment within the filler particles. For the macro-porosity analyzed via image analysis it was found that a majority of the total porosity is composed of a just a few large pores. The pore frequency per unit volume as a function of pore size is roughly logarithmic in nature with IG-110 having the largest deviation from linearity. The average aspect ratio of the porosity (assuming a simple elliptical model) is approximately 2. A probability density function of the shape (described by eccentricity) was best fit by a Johnson S_B distribution function. This distribution function was used to infer that 0.6%-0.9% of the total observed porosity can be attributed to shrinkage cracks in the filler particles. Finally, a preferred orientation of the porosity was observed in all grades.

While the size and shape of these three-dimensional features cannot be directly derived from two-dimensional measurements, they do provide a qualitative basis for comparison with irradiated and oxidized graphite specimen. Further development of the image analysis code for use with μX-ray computer tomography is currently underway and initial measurements of the three-dimensional porosity are qualitatively in good agreement with the two-dimensional observations.

Chapter Five focused on the development of an intrinsic rate equation for the reaction of high-purity graphite with oxygen. This work in many ways built upon work in the previous chapters. The biggest contribution was the observation in Chapter Two that the binder and filler regardless of the graphite grade had long range graphitic order. The implication of this observation to oxidation was that all grades intrinsically react at the same rate. The differences between grades in the rate of reaction are purely an apparent effect of the size, shape, and orientation of the crystallites in the binder and filler and the nature of the porosity which allows oxygen to penetrate into the structure.

The experimental data demonstrates that a simple reaction model with effective Arrhenius parameters, which is quite common in the nuclear graphite literature [2-13], poorly describes the graphite-oxygen reaction system over a wide range of temperatures and pressures. On the other hand, the oxygen transfer model developed provides an excellent fit to the experimental data, over the entire experimental temperature and pressure range, (500 °C-850 °C and 1 kPa-40 kPa) the most significant experimental deviation from the model is only off by a factor of 1.8.

The oxygen transfer model is also based on the graphite-oxygen reaction mechanism proposed by Radovic *et al.* [14, 15], which takes into account the vast majority of know influences and experimental observations involving the reaction. This implies that the activation energies are directly related to the individual elementary reaction steps within the reaction mechanism, and thus have a physical meaning. A direct comparison of the fitted elementary reaction parameters are in excellent agreement with both experimental and density functional theory calculations of the same parameters [16-20]. The implications of the excellent agreement are two-fold: First, the parameters come from multiple carbon sources (and configurations of "graphene" molecules for density functional theory simulations). This suggests that the reaction model is applicable to all grades of nuclear graphite. Second, since the parameters are directly related to the reaction mechanism, a much high degree of confidence can be given to the extrapolation of the model beyond the experimental range.

When used in combination with material dependent parameters such as effective diffusivity and effective reactive surface area, the apparent rate of reaction, as well as the local carbon loss within a monolithic graphite structure can be accurately predicted.

6.1 References

[1] R. H. Telling and M. I. Heggie, "Radiation defects in graphite," *Phil. Mag.*, **87**[31] 4797-4846 (2007).

[2] E. S. Kim and H. C. No, "Experimental study on the oxidation of nuclear graphite and development of an oxidation model," *J. Nucl. Mater.*, **349**, 182-194 (2006).

[3] H. Yang, H. Eun, D. Lee, C. Jung, and K. Lee, "Analysis of combustion kinetics of powdered nuclear graphite by using a non-isothermal thermogravimetric method," *J. Nucl. Sci. Technol.*, **43**, 1436-1439 (2006).

[4] H. Kawakami, "Air oxidation behavior of carbon and graphite materials or HTGR," *Tanso*, **124**, 26-33 (1994).

[5] S. Chi and G. Kim, "Comparison of oxidation rate and degree of graphitization of selected IG and NBG nuclear grades," *J. Nucl. Mater.*, **381**, 9-14 (2008).

[6] E. S. Kim, H. C. No, B. J. Kim, and C. H. Oh, "Estimation of graphite density and mechanical strength variation of VHTR during air-ingress accident," *Nucl. Eng. Des.*, **238**[4] 837-847 (2008).

[7] L. Xiaowei, R. Jean-Charles, and Y. Suyuan, "Effect of temperature on graphite oxidation behavior," *Nucl. Eng. Des.,* **227**[3] 273-280 (2004).

[8] H. K. Hinssen, K. Kühn, R. Moorman, B. Schlögl, M. Fechter, and M. Mitchell, “Oxidation experiments and theoretical examinations of graphite materials relevant for PBMR,” *Nucl. Eng. Des.*, **238**[11], 2018-2025 (2008).

[9] E. L. Fuller and J. M. Okoh, “Kinetics and mechanisms of the reaction of air with nuclear grade graphites: IG-110,” *J. Nucl. Mater.*, **240**, 241-250 (1997).

[10] M. S. El-Genk and J. P. Tournier, “Development and validation of a model for the chemical kinetics of graphite oxidation,” *J. Nucl. Mater.*, **411**, 193-207 (2011).

[11] M. S. El-Genk and J. P. Tournier, “Comparison of oxidation model predictions with gasification data of IG-110, IG-430 and NBG-25 nuclear graphite,” *J. Nucl. Mater.*, **420**, 141-158 (2012).

[12] M. S. El-Genk and J. P. Tournier, “Validation of gasification model for NBG-18 nuclear graphite,” *Nuc. Eng. Des.*, **250**, 142-155 (2012).

[13] R. Moormann, H.K. Hinssen, and K. Kühn, “Oxidation behavior of an HTR fuel element matrix graphite in oxygen compared to a standard nuclear graphite,” *Nucl. Eng. Des.*, **227**, 281-284 (2004).

[14] L. R. Radovic, “Active sites in graphene and the mechansim of CO_2 formation in carbon oxidation,” *J. Am. Chem. Soc.*, **131**, 17166-17175 (2009).

[15] L. R. Radovic, A. F. Silva-Villalobos, A. B. Silva-Tapia, and F. Vallejos- Burgos, “On the mechanism of nascent site deactivation in graphene,” *Carbon*, **49**, 3471-3487 (2011).

[16] A. B. Silva-Tapia, X. García-Carmona, and L. R. Radovic, “Similarities and differences in O_2 chemisorption on graphenenanoribbon vs. carbon nanotube,” *Carbon*, **50**, 1152-1162 (2012).

[17] A. Sánchez and F. Mondragón, “Role of the epoxy group in the heterogeneous CO_2 evolution in carbon oxidation reactions,” *J. Phys. Chem. C*, **111**, 612-617 (2007).

[18] J. F. Orrego, F Zapata, T. N. Truong, and F. Mondragón, “Heterogeneous CO_2 evolution from oxidation of aromatic carbon-based materials,” *J. Phys. Chem. A*, **113**, 8415-8420 (2009).

[19] A. Montoya, T. T. Truong, F. Mondragón, and T. N. Truong, “CO desorption from oxygen species on carbonaceous surface: 1. Effects of the local structure of the active site and the surface coverage,” *J. Phys. Chem. A*, **105**, 6757-6764 (2001).

[20] P. L. Walker Jr, L. G. Austin, and J. J. Tietjen, “Oxygen chemisorption effects on graphite thermoelectric power”; pp. 327-365 in Chemistry and Physics of Carbon Vol. 1. Edited by P. L. Walker Jr., Dekker, New York, 1965.